Toward Understanding Bacterial Ice Nucleation

Interface-specific nonlinear spectroscopy used to unravel the working mechanisms of bacterial ice nucleation proteins

Max Lukas

Max Planck Institute for Polymer Research

Johannes Gutenberg University

1. Gutachter*in:

2. Gutachter*in:

Tag der mündlichen Prüfung: 9. März 2022

Declaration

I hereby declare that I wrote the dissertation submitted without any unauthorized external assistance and used only sources acknowledged in the work. All textual passages which are appropriated verbatim or paraphrased from published and unpublished texts as well as all information obtained from oral sources are duly indicated and listed in accordance with bibliographical rules. In carrying out this research, I complied with the rules of standard scientific practice as formulated in the statutes of Johannes Gutenberg-University Mainz to insure standard scientific practice.

Mainz, December 2021
Max Lukas

Abstract

Small droplets of pure water, as they are found in our atmosphere, can be supercooled to temperatures close to $-40\,°C$. Above this temperature, the formation of a stable initial ice nucleus can be triggered by interaction with aerosol particles. The properties that make a good ice nucleator (IN) have been under discussion for decades, based on the idea that the underlying mechanism must involve ordering of adjacent water molecules into an ice-like structure. A variety of efficient INs have been identified, of which the bacterium *Pseudomonas syringae* exhibits exceptional ice nucleation efficiency, facilitating freezing at $\sim -2\,°C$. Although it is known that specialized ice nucleation proteins (INPs), anchored to its cell membrane, are responsible for the nucleation mechanism, this same membrane integration impedes the analysis of the protein's three-dimensional structure and hence clarity about its working mechanism.

In the first chapter of this thesis, the previous fundamental findings concerning bacterial ice nucleation proteins, in specific of *P. syringae*, are compiled and discussed. These indicate that a distinctive feature of the bacterial INs, the precise assembly of the INPs into functional aggregates, is crucial for their efficiency. It has been shown that this aggregation largely depends on environmental conditions; the reasons, however, have remained unclear. Therefore, we conduct studies on the influences of pH as well as ion-specific interactions.

In this thesis, we use interface-specific sum-frequency generation (SFG) vibrational spectroscopy to investigate the molecular-level interaction of the proteins with water. As a tool for evaluating the effects on the functional level, we utilize the Twin-plate Ice Nucleation Assay (TINA). This droplet freezing experiment yields so-called *freezing spectra*, which give information on the INs present in the sample, active at distinct freezing temperatures.

Applying this combined approach, we discover that the absence of the natural net charge at the isoelectric point of the INPs is accompanied by the complete loss of the most efficient *Class* of functionally aggregated INs, which is an important detail of this puzzling class-selective pH dependence (Chapter 4).
Furthermore, we link the effects of ions on the ice nucleation efficiency to their specific interactions with the protein surface, by studying INP solutions in the presence different salts (Chapter 5). We find that these specific ion effects on the threshold freezing

temperatures follow the Hofmeister series and propose two competing explanatory approaches based on molecular dynamics simulations.

Next, we make use of ice-affinity purification methods and focus on investigations of temperature effects on the protein structure (Chapter 6). Using circular dichroism and Amide I SFG spectroscopy, we demonstrate that its three-dimensional structure is not altered at low temperatures but drastically changed upon heat treatment, which in turn results in the loss of its ice nucleation activity. Moreover, we show that a previously reported increased order of water in contact with INPs at low temperatures is also found for such heat-inactivated INP solutions, and therefore does not constitute a sufficient condition for ice nucleation activity.

Finally, we conclude our studies and formulate a *perspective* on the research of bacterial INPs (Chapter 7). We emphasize the importance of functional aggregation and environmental conditions and hence consideration of the crucial role of the bacterial membrane. An understanding of the outstanding ice nucleation efficiency of bacterial INPs demands an interdisciplinary approach to link functional-level effects observed with high-throughput freezing assays with changes of the proteins' conformation and their interactions with water.

In addition to the introduction into the fundamentals of nonlinear optics and conventional SFG spectroscopy, as used in the presented studies, this thesis also contains a detailed discussion of phase-resolved SFG (PR-SFG). Capturing the phase of SFG signals has several advantages; most prominently, it provides direct information on the molecular orientations at the probed interface. In Chapter 3, a novel setup is presented, which overcomes the inherent technical challenges in a way that future studies, not only of ice-nucleating bacteria as proposed in as Chapter 8, can benefit from these advantages without significant additional experimental effort.

Zusammenfassung

Kleine Tröpfchen puren Wassers, wie man sie in unserer Atmosphäre findet, können bis zu Temperaturen von fast $-40\,°C$ unterkühlt werden. Oberhalb dieser Temperatur kann die Bildung eines stabilen, initialen Eisnukleus durch die Interaktion mit Aerosolpartikeln angestoßen werden. Die Eigenschaften die einen guten Eisnukleator (IN) ausmachen werden seit Jahrzehnten diskutiert, ausgehend von der Idee, dass der zugrundeliegende Mechanismus die Ordnung der angrenzenden Wassermoleküle in eine eisartige Struktur beinhalten muss. Eine Vielzahl an effizienten IN wurde identifiziert, von denen das Bakterium *Pseudomonas syringae* eine herausragende Eisnukleationseffizienz aufweist und Gefrieren bei $\sim -2\,°C$ ermöglicht. Obwohl bekannt ist, dass spezialisierte Eisnukleationsproteine (INP), verankert in der Zellmembran, für den Nukleationsmechanismus verantwortlich sind, behindert ebenjene Membranintegration die Analyse der dreidimensionalen Struktur des Proteins und damit Klarheit über dessen Arbeitsmechanismus.

Im ersten Kapitel dieser Dissertation werden zunächst die grundlegenden Erkenntnisse zu bakteriellen Eisnukleationsproteinen, im Speziellen von *P. syringae*, zusammengefasst und diskutiert. Diese deuten darauf hin, dass ein charakteristisches Merkmal der bakteriellen IN, die präzise Aneinanderfügung der INP zu funktionalen Aggregaten, für ihre Effizienz entscheidend ist. Es wurde gezeigt, dass diese Aggregation stark von Umwelteinflüssen abhängt; die Ursachen blieben bisher allerdings unklar. Wir führen daher Studien zu den Einflüssen von pH und zu ionenspezifischen Interaktionen durch.

In dieser Dissertation setzen wir grenzflächenspezifische Summenfrequenzspektroskopie (SFG) ein, um die Interaktionen der Proteine mit Wasser auf der molekularen Ebene, anhand der Molekülschwingungen, zu untersuchen. Zur Erfassung der Effekte auf der funktionalen Ebene nutzen wir das *Twin-plate Ice Nucleation Assay* (TINA). Dieses Tropfengefrierexperiment ergibt sogenannte *Gefrierspektren*, die Information zu den IN in einer Probe, aktiv bei verschiedenen Gefriertemperaturen, geben.

Dabei entdecken wir, dass die Abwesenheit der natürlichen Nettoladung am isoelektrischen Punkt der INP vom kompletten Verlust der effizientesten *Klasse* der funktional aggregierten INP begleitet wird, was ein wichtiges Detail dieser rätselhaften klassenselektiven pH-Abhängigkeit ist (Kapitel 4).

Des Weiteren können wir die Effekte von Ionen auf die Eisnukleationseffizienz mit ihren

spezifischen Interaktionen mit der Proteinoberfläche in Verbindung bringen, indem wir INP-Lösungen unter Zugabe verschiedener Salze untersuchen (Kapitel 5). Wir stellen fest, dass die spezifischen Ioneneffekte auf die Gefriertemperaturen der Hofmeisterserie folgen und schlagen zwei mögliche Erklärungsansätze unter Zuhilfenahme von Molekulardynamik-Simulationen vor.

Anschließend nutzen wir Eisaffinitäts-Aufreinigungsmethoden und fokussieren uns auf Untersuchungen von Temperatureffekten auf die Proteinstruktur. Mithilfe von Circulardichroismus- und Amid I-SFG-Spektroskopie zeigen wir, dass ihre dreidimensionale Struktur sich bei niedrigen Temperaturen nicht, dagegen bei Hitzebehandlung drastisch verändert, was wiederum zum Verlust der Eisnukleationsaktivität führt. Wir zeigen außerdem, dass eine zuvor berichtete erhöhte Ordnung des Wassers in Kontakt mit INP bei niedrigen Temperaturen auch bei solchen hitzeinaktivierten INP-Lösungen auftritt und somit keine ausreichende Bedingung für Eisnukleationsaktivität sein kann.

Schließlich fassen wir unsere Studien zusammen und formulieren eine *Perspective* auf die Erforschung bakterieller INP (Kapitel 7). Wir betonen die Wichtigkeit der funktionalen Aggregation und von Umwelteinflüssen, und somit der Berücksichtigung der entscheidenden Rolle der Bakterienmembran. Ein Verständnis der außergewöhnlichen Eisnukleationseffizienz bakterieller INP verlangt nach interdisziplinären Methoden, um Effekte auf der funktionalen Ebene, beobachtet mit Hochdurchsatz-Gefrierexperimenten, mit Veränderungen der Struktur der Proteine und ihrer Interaktion mit Wasser zu verbinden.

Zusätzlich zu der Einführung in die Grundlagen der nichtlinearen Optik und konventioneller SFG-Spektroskopie, wie sie in den aufgeführten Studien zum Einsatz kommt, enthält diese Arbeit auch eine detaillierte Diskussion phasenaufgelöster SFG-Spektroskopie (PR-SFG). Die Erfassung der Phase von SFG Signalen hat mehrere Vorteile, am markantesten davon direkte Information über die Orientierung der Moleküle in der untersuchten Grenzfläche. In Kapitel 3 wird ein neuer Versuchsaufbau präsentiert, der die inhärenten technischen Herausforderungen in einer Weise überwindet, dass zukünftige Studien, nicht nur von eisbindenden Proteinen (Kapitel 8), von diesen Vorteilen profitieren können, ohne signifikanten zusätzlichen experimentellen Aufwand.

Outline and Own Contribution

This thesis covers collaborative studies of the ice-nucleating bacterium *Pseudomonas syringae* and the development of a novel phase-resolved sum-frequency generation (PR-SFG) vibrational spectroscopy setup.

Chapter 1 starts with an introduction into the basic theory of heterogeneous ice nucleation and the state of research, pointing out why studies of the ice nucleation mechanism of proteins from *P. syringae* are significant, and deriving some open questions as a framework for the studies described in the Chapters 4 to 6.

In these collaborative studies, I contributed to research design, the analysis, discussion and interpretation of the obtained results, and as (co-)lead author in writing the manuscripts. My experimental contribution consisted predominantly in the sum-frequency generation (SFG) vibrational spectroscopy experiments. An introduction into nonlinear optics, in particular SFG, is given in Section 1.3, followed by a description of the SFG experiment in Section 2.1. All freezing assay (TINA) experiments were performed by Ralph Schwidetzky; I contributed to the interpretation and discussion of the data. The principles of the TINA experiments are discussed in Section 2.2.

Based on our results, we formulated a *perspective* (Chapter 7) on bacterial ice nucleation, where I contributed as the lead author, and which serves as a conclusion chapter of this thesis. In Chapter 8, these conclusions are supplemented in regard of future implications for SFG studies of biological ice nucleators.

The phase-resolved SFG setup described in Chapter 3 has been developed independently from the work on *P. syringae*, but is an excellent tool for any future SFG studies, including such investigations on ice-nucleating biomolecules. Here, I constructed and tested the setup, conducted the experiments, contributed to setup and experimental design and evaluation, and was lead author of the manuscript. An introduction into PR-SFG is given in Section 2.1.3.

Publications Covered in this Thesis

Chapter 3 M. Lukas, E. H. G. Backus, M. Bonn, and M. Grechko. **Passively Stabilized Phase-Resolved Collinear SFG Spectroscopy Using a Displaced Sagnac Interferometer**. *Submitted to the Journal of Physical Chemistry A*, 2021

Chapter 4 M. Lukas, R. Schwidetzky, A. T. Kunert, et al. **Electrostatic Interactions Control the Functionality of Bacterial Ice Nucleators**. *Journal of the American Chemical Society*, **142**(15):6842–6846, 2020

Chapter 5 R. Schwidetzky, M. Lukas, A. YazdanYar, et al. **Specific Ion–Protein Interactions Influence Bacterial Ice Nucleation**. *Chemistry – A European Journal*, **27**(26):7402–7407, 2021

Chapter 6 M. Lukas, R. Schwidetzky, A. T. Kunert, et al. **Interfacial Water Ordering Is Insufficient to Explain Ice-Nucleating Protein Activity**. *The Journal of Physical Chemistry Letters*, **12**(1):218–223, 2020

Chapter 7 M. Lukas, R. Schwidetzky, R. J. Eufemio, et al. **Towards Understanding Bacterial Ice Nucleation**. *Submitted to the Journal of Physical Chemistry B*, 2021

Contents

Glossary

AFP Antifreeze protein; protein able to hinder the growth of ice crystals and thereby to reduce the freezing temperature.

C-terminus domain Non-repetitive amino acid sequence domain, found in the consensus sequence of ice nucleation proteins and located between the central repeat domain and the C-terminus.

CD spectroscopy Circular dichroism spectroscopy

Class A, (B), C (Hypothetical) Classes of ice nucleators found in the freezing spectra of ice nucleation active bacteria

Consensus sequence The consensus (or canonical) sequence of a protein is the most conserved sequence of amino acids, when comparing different protein sequences by sequence alignment.

CRD Central repeat domain; repeating amino acid sub-domains found in the consensus sequence of ice nucleation proteins. Responsible for the protein's ability to order water into an ice-like structure.

DFG Difference-frequency generation; second-order nonlinear process where light with the difference-frequency of two incident frequencies of light is generated.

Freezing spectrum Spectrum of the ice nucleators present in an investigated sample, active at distinct freezing temperatures.

FWHM Full width at half maximum

IBP Ice-binding protein; proteins that have an affinity to bind to ice, for instance, ice nucleation and antifreeze proteins.

IBS Ice-binding site; structural motif responsible for the ability to bind to the surface of ice.

IEP/IIEP (Interfacial) Isoelectric point; pH value, at which the net charge of a sample in solution (at the interface between sample film and water) is zero.

IN Ice nucleator; particle or surface which induces heterogeneous ice nucleation.

INP Ice nucleation protein; protein able to induce heterogeneous ice nucleation, sometimes also referred to as ice-nucleating protein

IR Infrared; usually referring to the mid-infrared beam utilized in an SFG experiment.

LO Local oscillator; an auxiliary electromagnetic wave, utilized in phase-resolved sum-frequency generation spectroscopy and usually generated by sum-frequency generation in an optically nonlinear crystal.

MD simulations Molecular dynamics simulations

N-terminus domain Non-repetitive amino acid sequence domain found in the consensus sequence of ice nucleation proteins and located between the central repeat domain and the N-terminus.

PR-SFG   Phase-resolved sum-frequency generation spectroscopy, also referred to as phase-sensitive or heterodyne SFG.

SFG   Sum-frequency generation; second-order nonlinear process where light with the sum-frequency of two incident frequencies of light is generated.

SHG   Second-harmonic generation; second-order nonlinear process where light with the double-frequency of the incident light is generated.

Snomax®   Commercial product which contains sterile extracts from the bacterium *P. syringae*.

TINA   Twin-plate ice nucleation assay; a high-statistic droplet freezing assay for the acquisition of freezing spectra of efficient ice nucleators.

VIS   Visible; usually referring to the near-infrared ($\sim 800\,\mathrm{nm}$) beam utilized in an SFG experiment.

1

Introduction & Theory

1.1   Heterogeneous Ice Nucleation

Life on Earth as we know it is primarily based on its atmosphere and a fragile, indispensable energy balance. Next to their role in the hydrological cycle, clouds contribute to that balance by reflecting shortwave, respectively absorbing and re-emitting longwave radiation.[6] These radiative interactions depend largely on the ratio of liquid water to ice in a cloud, which in turn also determines its extent, lifetime, and precipitation.[7] Freezing processes in clouds hence play a key role in understanding the complex systems which steer global precipitation patterns, and ultimately the global climate. The droplet volumes found in clouds are in the micro- or nanoliter range. Freezing of such tiny volumes of pure water behaves fundamentally different from that of volumes in our everyday experience, as it can be shifted to around $-40\,°C$. Freezing at higher temperatures is decisively controlled by the interaction with aerosol particles, which serve as crystallization nuclei.[8,9] These two fundamental processes, **homogeneous** and **heterogeneous ice nucleation** are briefly elucidated in the following.

Below its melting point, the thermodynamically favored state of water is ice. However, the initial formation of a stable ice crystal nucleus is determined by kinetics and requires a temperature-dependent critical cluster size of properly ice-like aligned molecules. For this reason, homogeneous ice nucleation, is shifted down to much lower temperatures (T_{hom} in Figure 1.1). In the following, the situations is discussed in terms of classical nucleation theory (CNT). This approach is concluded in more detail, for instance, in Murray *et al.* and predicts, despite some inherent weaknesses, experimentally well-reproducible trends.[10,11,12,13,14]

The total Gibbs free energy is the sum of the surface free energy ΔG_S needed for creating an interface between the embryonic crystal and the surrounding water, and the excess volume free energy ΔG_V from the formation of hydrogen bonds in the bulk of the cluster:

$$\Delta G_{l \to s} = \Delta G_S + \Delta G_V = 4\pi r^2 \gamma + \frac{4}{3}\pi r^3 \Delta G_v \qquad (1.1)$$

Here, r is the cluster radius, γ the interfacial tension between the developing crystal surface and the liquid phase, and ΔG_v is the free energy change per unit volume upon transformation from liquid to solid.[12]

The diagram in Figure 1.2 shows the total free energy vs. the number of molecules in an ice nucleus. At small numbers of clustered molecules i, ΔG_S dominates; therefore,
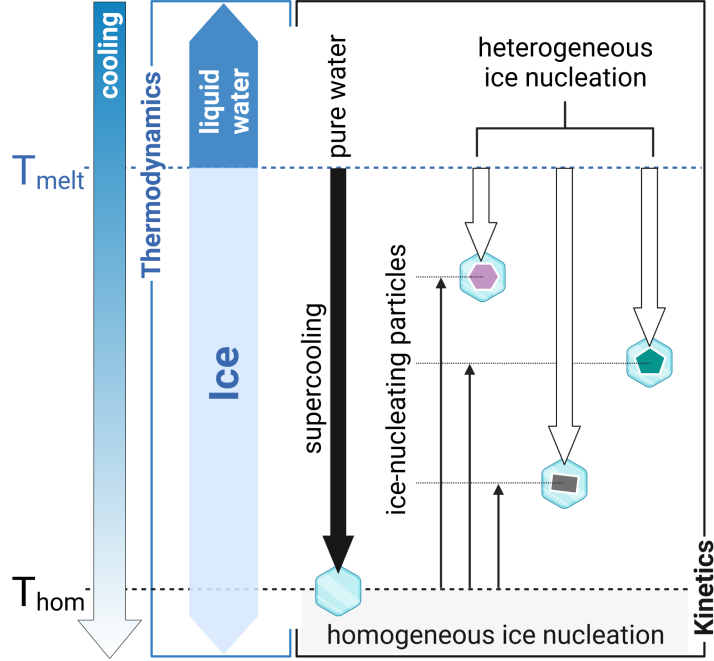
Figure 1.1: Illustration of homogeneous and heterogeneous ice nucleation - Thermodynamically, the stable state of water below its melting point, T_{melt}, is ice. Due to kinetic hindrance, ice nucleation in pure water occurs only at the much lower homogeneous freezing temperature T_{hom}. Immersed particles can trigger heterogeneous ice nucleation of the supercooled water at intermediate temperatures ($T_{melt} > T_{het} > T_{hom}$), which depend on the individual particle's ice nucleation efficiency.

small nuclei forming through fluctuations in the metastable water redissolve (or "melt back") into the more stable liquid phase. Above a critical number i^*, the total free energy decreases when further molecules are added to the seed and it grows spontaneously. This energy barrier ΔG^*, and thus the critical number of molecules in a stable nucleus i^*, depends on the supercooling temperature, and determines the probability for the emergence of stable nuclei from fluctuations in the liquid water.

The rate of critical-size embryo formation can hence be expressed in an Arrhenius form as

$$J(T) = A \exp\left(-\frac{\Delta G^*}{kT}\right),\tag{1.2}$$

with the Boltzmann constant k and the absolute temperature T. The constant A, which can be determined experimentally or in models,[10,11,12,14] and therefore J have the dimension $cm^{-3}s^{-1}$, underlining that the homogeneous freezing temperature is volume-dependent. It has been shown, that once a stable embryonic crystal has evolved,
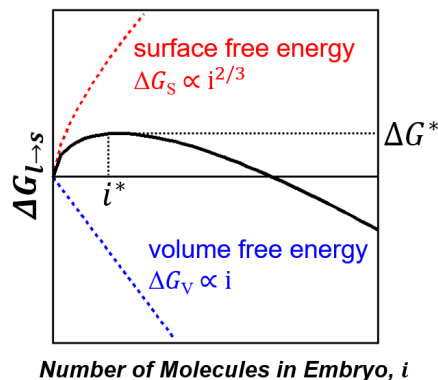
Figure 1.2: Free energy diagram for the formation of an embryonic ice nucleus - The surface free energy dominates the total free energy $\Delta G_{l \to s}$, up to a critical number of molecules i^* in the embryo ($r \propto i^{1/3}$). Above this number, the addition of further molecules decreases the total free energy. i^*, and thereby the critical free energy ΔG^* depend on the supercooling temperature. The diagram is qualitatively reproduced from Wolber (1993).[11]

it serves as a seed for secondary ice nucleation and leads to rapid crystallization at the respective threshold temperature.[10,11] This cascade explains why larger volumes of water, as in our everyday experience, freeze close to the melting point, while in small droplet volumes, as they are found, for instance, in mixed-phase clouds, homogeneous ice nucleation occurs at about $-38\,°C$.[15,16] These clouds appear in the troposphere and lower stratosphere and are therefore directly involved in the hydrological cycle. They have a strong impact on local and global climate and, not least, are largely affected by **heterogeneous ice nucleation**:[17]

Phase transitions in our atmosphere, like ice nucleation or condensation, are triggered by the ubiquity of a diversity of aerosol particles and thereby depend largely on latitude, soil properties, and season.[14] It has also been shown that anthropogenic sources have increased the load of continental aerosol by orders of magnitudes and drastically shifted the pre-industrial homogeneity between continental and maritime aerosol concentrations.[14,18,19,20,21] Compared to condensation particles, effective ice nucleation particles are relatively rare and, interestingly, a direct connection between both properties can not be drawn.[14,20,22,23]

Figure 1.1 illustrates the effect of heterogeneous ice nucleation, for ice-nucleation particles immersed in water droplets. The nucleation temperature is shifted from the homogeneous nucleation temperature, up to a temperature that now depends on the properties of the individual **ice nucleator (IN)**. This shift from T_{hom} to T_{het} is the

formal measure for the ice nucleation efficiency of an IN. In experiments, the theoretical T_{hom} is oftentimes not detectable, inter alia, due to remaining impurities in the utilized water. Therefore, it is common to use the threshold temperatures, i.e., the supercooling temperatures at which the INs are active, to compare IN efficiencies.

In decades of research, the efficiencies of many different INs have been empirically quantified in various generations of freezing assays.[9,14,24,25,26,27,28] However, the responsible molecular-level interactions between their surfaces and the adjacent water molecules are still not fully understood. It is assumed that water in contact with ice-nucleating particles is ordered into an ice-like structure and subsequently forms embryonic crystals which are large enough to grow. Such a templating effect indicates crystal lattice matching as one important precondition. Pruppacher and Klett proposed some additional, general properties for an effective IN, such as:[15] 1) Size of the particle, as it should scale with the templated nucleus size and therefore the threshold temperature, 2) insolubility, as the ice-nucleating structure should not disintegrate in solution, and 3) the ability to bind chemically to water.

In terms of the above-introduced description, the ice nucleation rate J at a given temperature is increased by lowering the free energy barrier, which can be written as

$$\Delta G^*_{het} = \Delta G^*_{hom} \, \phi(m, R). \tag{1.3}$$

The function ϕ has been defined in different ways,[10,11,14,29] however, its value ranges between 0 and 1. It depends on the parameter m, which quantifies the ability of the IN to interact with water and to order it into an ice-like structure, and R, a measure for a characteristic length of the nucleus. While m is usually defined in terms of contact angles or interfacial free energies of the participant phases, the size parameter R as introduced by Wolber *et al.* remains more elusive. It has been described as a kind of "coherence length" of the ice-nucleating site with the ice crystal lattice. It considers that there is a maximum distance over which a given IN can order water into an ice-like structure, before accumulated strains due to lattice mismatch prevail.[11]

Experimentally, it could be shown for various ice-nucleating mineral surfaces that the application of general explanations for the activities of individual INs remains complicated. For instance, rigorous, charge-induced ordering into slightly different structures can even suppress ice nucleation, while some minerals seem to facilitate ice

nucleation mainly due to the presence of defects in their crystal structure.[14,30,31,32] Interestingly, the introduced basic requirements on an effective IN can also be found to match the apparent properties of another, very important category of INs: **Bacterial ice nucleation proteins**.

Among the most relevant types of ice-nucleating particles are mineral dusts as well as organic macromolecules.[14,33,34] While mineral dusts and soot are expected to be responsible for up to $\sim 80\%$ of atmospheric ice nucleation,[14,35] their efficiencies, i.e., the threshold temperatures, are rather low. Further generalized, ice nucleation below around $-15\,°\mathrm{C}$ is mostly driven by mineral dusts and soot.[14] But freezing temperatures of water droplets as high as $-5\,°\mathrm{C}$ or $-2\,°\mathrm{C}$ are, with few exceptions (e.g., silver iodide), only reached by a number of ice-nucleating microorganisms, apparently naturally designed to serve as dedicated INs (Figure 1.3).[11,14]
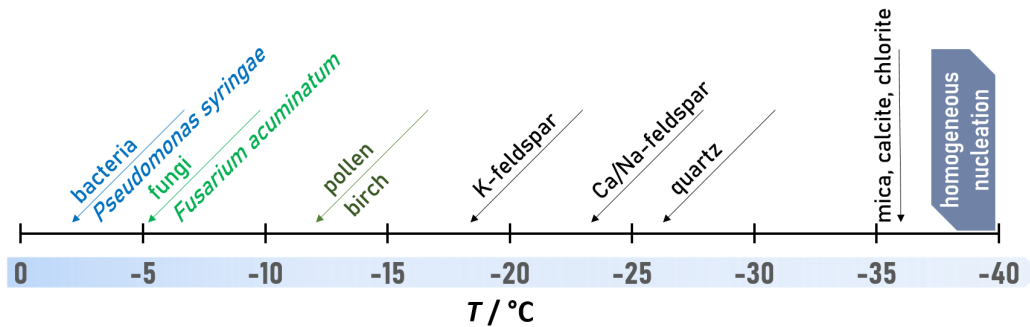

Figure 1.3: Overview of typical threshold temperatures of selected ice nucleators - The indicated temperatures represent typical datasets found in literature, where more differentiated overviews are available.[14,27]

1.2   Bacterial Ice Nucleation Proteins

One of the most effective and best characterized atmospheric relevant ice-nucleating microorganisms is the gram-negative bacterium *Pseudomonas syringae*. Its ice nucleation activity was discovered in the 1970's and in the following years, several other gram-negative species from the families *Pseudomonadaceae*, *Enterobacteriaceae* and *Xanthomonadaceae*, as well as the gram-positive *Lysinibacillus*, have been added to the list of ice-nucleating bacteria.[36,37,38,39,40]

Water droplets in contact with *P. syringae* freeze close to the melting point, at temperatures up to $-2\,°C$.[36,41] This outstanding ice nucleation efficiency allows the plant pathogenic bacterium to invade frost-damaged host tissue at mild subzero temperatures.[42] Meanwhile, under the product name Snomax®,[43] sterile, freeze-dried *P. syringae* extracts are commercially used as a supplement for snowmaking in ski areas. Snomax® also serves as a commonly used and comparable model system in various studies,[26,44,45,46] including the studies covered by this thesis.

It is known that the bacterium's ice nucleation activity originates from specialized ice nucleation proteins (INPs),* which are attached to the bacteria's outer cell membranes (Figure 1.4).[47,48] The consensus ("common") sequences of several INPs from ice-nucleating bacteria were inferred in the 1980's. It had been found that the ice nucleation activity phenotype can be transferred to *Escherichia coli* by cloning DNA stretches from ice-nucleating bacteria.[11,49] The five genes identified in this way encode five INPs with largely similar sequences of amino acid residues ($\sim 85\%$), which in turn contain domains of highly repetitive residue series. These domains are usually referred to as **central repeating domains (CRDs)**, and they are surrounded by two further, unique domains; one at the N-terminal ($-NH_2$) and one at the C-terminal ($-COOH$) of the protein. The CRD is composed of 4 subdomains with repeats of 8, 16 or 48 amino acid residues. The largest fidelity of the repetition is found in the center, where the 48 residue repeat is nearly perfect and is built up of 3 units of the 16 residue repeat GYGSTxTAxxxSxLxA (x's denote non-conserved amino acids).[50] A detailed overview of the consensus primary structure is, for instance, given in *Wolber* (1993).[11]

---

*While the proteinaceous origin of bacterial ice nucleation is well accepted, there is less clarity about the INs from other species like fungi, lichen or pollen. Since the focus of this thesis is on bacterial INs, whenever the term INP is used without further specification it refers to bacterial INPs from *P. syringae*.

It has been tried to derive the ice-active residue motifs from the CRD sequence, however, their large size ($> 120\,\mathrm{kDa}$), their tendency to aggregate, and their association to the bacterial membrane hamper attempts to solve the three-dimensional structure of the protein and therefore a clear understanding of the underlying mechanisms of their interaction with water.[47]
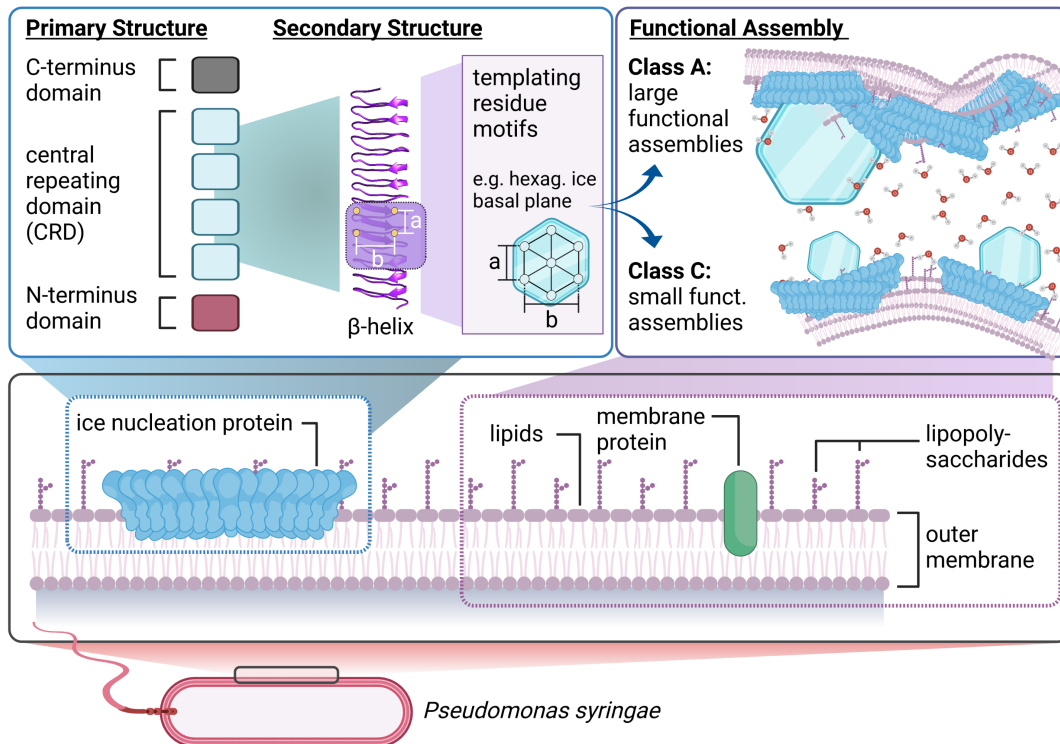
Figure 1.4: Overview of the proposed structures and working mechanism of bacterial ice nucleation proteins - The INPs are anchored to the outer cell membrane of the gram-negative *P. syringae*. Their principal working mechanism is believed to be based on an ice crystal-templating repeating domain of amino acid residues (CRD). The secondary structure has been proposed to be β-helical. The distinct threshold temperatures found for the bacterium are ascribed to different states of functional protein aggregation, in which the membrane and attached components might play a decisive role. This figure has been published in Lukas *et al.*[5]

A promising approach for the solution of this issue arises from the idea that INPs share a fundamental mechanism with proteins, which utilize it for the opposite effect on water: **Antifreeze proteins (AFPs)**. In contrast to the bacterial INPs, they are not bound to a membrane, which simplifies purification, and they are substantially smaller ($< 40\,\mathrm{kDa}$). Therefore, the 3D structures of AFPs from various natural sources like

insects and fish have been solved.[51,52,53,54,55,56] AFPs possess ice-binding sites (IBS), which are responsible for the adsorption of the AFP to an ice crystal. Thereby, the growing crystal surface is forced to curve, which consumes additional energy and decreases the freezing temperature.[57,58,59] In case of hyperactive insect AFPs, those IBS consist of flat arrays of TxT* repeats exposed by a β-helix. The result is a two-dimensional lattice with distances comparable to those found in the ice-crystal (prismatic and basal plane, Figure 1.4).[53,60,61,62,63]

Helices had been suggested before and models also predicted planar anti-parallel β-strand arrays.[50,63,64] Those predictions have been combined to a model assuming a β-helical fold with β-stranded hydrophobic TxT motifs within each 16 amino acid repeat.[61,65] Recent studies propose that both, the TxT residues of hyperactive insect AFPs and bacterial INPs, utilize anchored clathrate motifs to bind to the ice crystal planes, respectively to nucleate ice by aligning water into an ice-like structure.[66,67] In case of INPs, those clathrate motifs have been proposed to be supplemented by hydrophilic ice-like hydrogen bonding motifs (ExSxT)† on the opposite side of the helix.[67] The idea, however, is striking as it implicates that INPs and AFPs do primarily not differ in the structure of their active sites, but by the effective surface areas of the ice-binding planes/sites (IBS) and other, related properties of the protein, for instance, rigidity.[67] This hypothesis has been experimentally supported by the observation of slight AFP activity of INP fragments.[68]

One central aspect of bacterial ice nucleation is the role of **functional aggregation**. Freezing spectra obtained from droplet freezing assays give information on the number of INs active at a given temperature. The spectra of *P. syringae* in aqueous solution reveal distinct, steep rises at $-2\,^\circ\text{C}$ and $-7\,^\circ\text{C}$, indicating the presence of two different populations of INs (explained in Section 2.2, Figure 2.9). This heterogeneity of the nucleation temperature was first described in 1981 and initially led to the establishment of 3 distinct *Groups*, I, II and III:[69] It had been found that the structures with the highest freezing temperatures, Group I ($\geq -4\,^\circ\text{C}$ to $-2\,^\circ\text{C}$) are the rarest, with 1 in 10^4 compared to 1 in 300 for Group III ($-8\,^\circ\text{C}$ to $-10\,^\circ\text{C}$). Turner *et al.* renamed and slightly redefined these groups to the *Classes* A, B and C used today, not least because of progress in the precision and accuracy of temperature steps in droplet freezing assays.[26]

---

*T: Threonine
†E: Glutamic acid; S: Serine

1. INTRODUCTION & THEORY

In this context, it is worth mentioning, and will be briefly discussed later in this thesis, that the modern freezing assay TINA (Section 2.2) does not provide clear indication for the existence of a Class B anymore (Chapter 7).[70]

An important finding concerning an explanation for the heterogeneity of freezing temperatures was that the highest threshold temperatures are reached by the largest structures of INs (up to 19.000 kDa).[47] Furthermore, Southworth *et al.* reported a non-linear relationship between ice nucleation temperatures and the concentration of INPs in bacterial samples.[71] Together those findings indicated that the different activation temperatures could be explained by aggregation of one type of INPs, which increases the effective sizes of the ice nucleation sites. Aggregation of the INPs in the cell membrane had been confirmed in several studies and it had also been suggested that the intact membrane, or associated components, might play a major role in the ice nucleation activity of the aggregates.[41,69,71,72] However, it has also been found that the different populations of bacterial INs must have different properties, inferable from different behavior upon chemical treatment.[11,26,50]

Another open question arises from the above-introduced idea of the "coherence length" of an ice nucleation site: How can this aggregation provide the needed control for such highly precise assembly of the single INPs' active sites? Recent molecular dynamics (MD) simulations indicate that such functional aggregation is able to produce INs that are active at all observed temperatures, provided that a (sub-)Ångström control over the INP arrangement is given.[73] Moreover, the results revealed that even the least efficient Class C INs' threshold temperatures are only explainable taking aggregation into account. In short, elongation of the beta-helical CRD of one INP (i.e., adding more loops) was shown not to lead to ice nucleation temperatures above $\sim -25\,°\mathrm{C}$ ($\widehat{=}$ 16 loops). This was, inter alia, attributed to the increase in anisotropy of the ice-binding plane, but also to the accumulation of slight crystal lattice distance mismatching.

Summed up, despite crystal structures of INPs remaining inaccessible, decades of research have brought extensive knowledge about their structure and working mechanism, also by utilizing similarities with the related protein class of AFPs. However, experimental insight is needed to unravel and connect the loose strings of the functional aggregation, the role of the membrane, the heterogeneity of the bacterial INs, and the three-dimensional protein structures. Our collaborative work tackling this task is covered in Chapters 4, 5 and 6 and concluded in Chapters 7 and 8.

1.3 Nonlinear Optical Spectroscopy

Spectroscopy commonly denotes studies of the specific wavelength-dependent interaction of matter with light. The term *spectrum* was first used by Isaac Newton, who described that white light can be decomposed into seven distinct colors using a prism.[74] Since, its meaning has been largely extended to include characterizations of other waves (e.g., matter, acoustic, gravitational) and further, rather borrowing, applications are common as well; for instance, when we designate the concentrations of different populations of ice nucleators, active at distinct threshold temperatures, as *freezing spectra*. Besides Newton's experiment, probably the most classic example for spectroscopy is the observation of absorption lines in the spectrum of light, transmitted by a medium, or conversely, recording the characteristic emission lines in the spectrum of a light source.

The origin of these discrete absorption and emission lines has only been understood after the development of quantum theory. It describes the quantization of the energy levels of an atom or a molecule, for instance, the orbitals of electrons in an atom, and assigns them to a set of quantum numbers. Electromagnetic radiation with a frequency ν on the other hand, has an energy which is quantized into photons with the energy $E = h\nu$, where h is the Planck constant. The energies of ultraviolet and visible light photons typically match transitions between the discrete electronic states of atoms, which therefore possess characteristic absorption and emission lines in this frequency range.

In molecules, atoms are furthermore connected by chemical bonds. In a simplified picture, a bond can be compared to a spring, with a spring constant k which relates the stretching (or bending) of this bond with a restoring force ($\vec{F} = -k\vec{x}$). Within this picture, the lines in the observed absorption spectra are comparable to the resonance curve of such a mechanical oscillator: Driven at the resonance frequency, the amplitude of the vibration is drastically increased. Obviously, incident electromagnetic radiation is absorbed when the frequency matches a resonance frequency of a molecular vibration. These resonance frequencies are predominantly found in the mid-IR range.

Under the condition that the restoring force increases linearly with the displacement x, an oscillator has a *harmonic*, parabolic potential $V = \frac{1}{2}kx^2$ and hence an (angular) resonance frequency $\omega_0 = \sqrt{\frac{k}{\mu}}$, where k is the spring constant and μ is the system's reduced mass. The quantum mechanical description, obtained by solving Schrödinger's

equation assuming a harmonic potential, yields that the energy of a vibration is quantized into states with energies $E_v = \hbar \left(v + \frac{1}{2} \right) \omega$, where v is the vibrational quantum number ($v = 0, 1, 2, ...$).

The requirement, or selection rule, that we can measure the absorption of incident IR light with a frequency that matches the energy difference between two vibrational states, is that the *transition dipole moment* $\boldsymbol{\mu}_{if} = \langle \psi_f | \hat{\boldsymbol{\mu}} | \psi_i \rangle$ between the initial and final state, which are described by their respective wave functions ψ_i and ψ_f, is non-zero.[75] In this case, the light induces a superposition of the states, which gives rise to an oscillating polarization. This polarization of the material is a source of an electromagnetic wave, which interferes destructively with the incident light, thus causing a dip in the spectrum. In practice, the *IR activity* of vibrational motions can oftentimes be deduced considering the symmetry of a molecule. The *gross selection rule* for IR activity is that the molecules dipole moment must change upon the relative displacement of the atoms during the vibration.

Molecules with more than two atoms consequently have more than one vibrational mode, which are represented by superpositions of independent vibrational motions. The so-called *normal modes* of the water molecule's vibrations are illustrated in Figure 1.5.
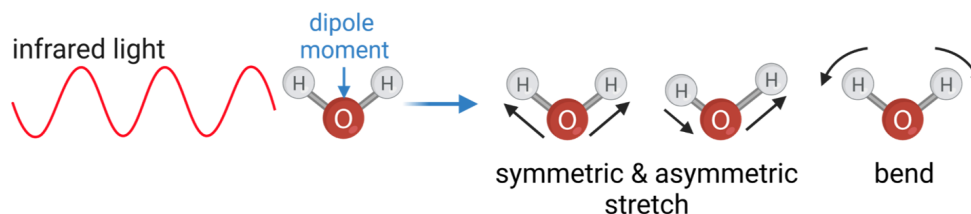

Figure 1.5: The three normal modes of the water molecule's vibrations - All of them are IR active and the dipole moment of the molecule changes with the vibrational motions.

Figure 1.6 A schematically illustrates vibrational energy levels and a transition from the ground state into the first excited state upon absorption of a photon with the respective frequency (*IR absorption*). Here, the states' envelop, the potential energy surface, doesn't correspond to a harmonic (parabolic) potential, but a potential that has anharmonicity (e.g., Morse potential). One limitation of the harmonic oscillator approximation is that the parabolic potential wouldn't allow for the dissociation of a bond, as the needed energy would be infinite. Moreover, all vibrational energy levels

would be equally separated, making the transitions between adjacent states of one vibrational mode indistinguishable in a spectrum. Another issue relates to the selection rules for a vibrational transition. The selection rule derived for the harmonic oscillator approximation allows only the *fundamental* transitions $\Delta\nu = \pm 1$, however, transitions $|\Delta\nu| > 1$ and therefore so-called *higher harmonics* or *overtones* can be observed as weak additional lines in experiments.[75]
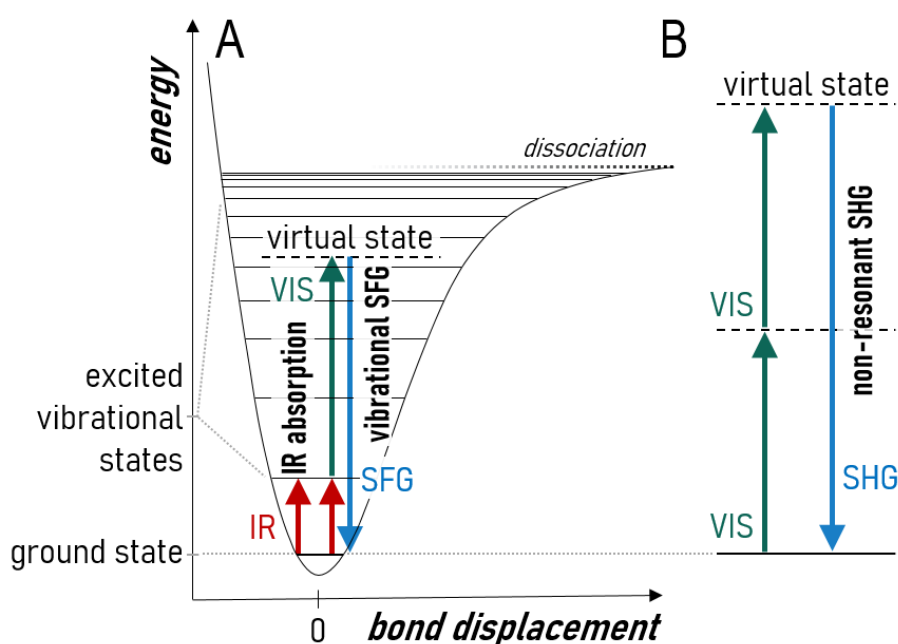

Figure 1.6: Schematic energy diagrams of IR absorption, vibrational SFG and non-resonant SHG - (A) IR absorption and SFG vibrational spectroscopy probe the vibrational resonances, shown here as the energy levels in an anharmonic potential. In the case of SFG, the excited state is upconverted to a virtual state by interaction with visible light and light of the sum-frequency is emitted. (B) SHG is oftentimes used off-resonantly and hence doesn't probe the electronic or vibrational resonances of a system.

In many conventional spectroscopy methods, such as the briefly described IR absorption spectroscopy, the collected information stems mainly from bulk molecules, as the surface area makes up a marginal percentage of the probed matter. The specific compositions, structures and dynamics of interfaces, however, are oftentimes of particular interest, which creates a strong demand for techniques that can provide an access to surface-specific investigations.

Spectroscopy techniques that make use of the second-order nonlinear optical effects

second-harmonic generation (SHG) and sum-frequency generation (SFG) provide such access to the investigation of interfaces in a unique manner: The specificity results directly from the intrinsic symmetry conditions and selection rules of these processes. In short, SHG causes the appearance of light of the double frequency ($2\omega_i$) of the incident light (ω_i). In case of using two beams with different frequencies (ω_i and ω_j), SFG describes a response that is of the sum of both frequencies ($\omega_i + \omega_j$). Therefore, SHG can also be described as a specific case of SFG, where the two incident beams' frequencies are equal. The interface-specificity means that detectable signals are, for most materials and experimental conditions, generated only from the outermost monolayer(s) of molecules.

With a few exceptions, nonlinear optical processes were only discovered and studied after the first working laser had been built due to the need for high intensities to generate measurable signals. However, from the discovery of SHG after the development of the ruby laser in 1961 to its understanding and the establishment as developed and recognized surface-specific method, it took more than twenty years.[76,77,78,79,80] SHG has been extensively applied to investigate adsorbates at liquid interfaces and to determine the orientation of the adsorbed molecules using polarization-dependent SHG as well as the interface charging.[81,82,83] Moreover, time-resolved SHG has been used to follow surface structural changes,[84] and SHG microscopy has been utilized to investigate spatial variations of surface structures.[85,86]

With the development of optical parametric amplifiers (OPAs) and hence the availability of tunable laser light in the IR region,[87] SFG spectroscopy gained in importance due to a shortcoming of SHG: While electronic transitions could be probed and detected using tunable visible frequencies, characteristic molecular vibrational modes, which require input frequencies in the mid-IR range, were not accessible with SHG due to the sensitivity limitations of IR detection (the frequency-doubled signals would still be predominantly in the IR range).[86] Therefore, oftentimes SHG gives only some information on the order and symmetry of a system, without the possibility to resolve this information for its distinct molecular species (non-resonant SHG; Figure 1.6 B). In contrast, SFG, which combines mid-IR with visible/near-IR frequencies (Figure 1.6 A), probes vibrational spectra, due to the frequency-summation shifted into the well-detectable visible region (enabling the use of charge-coupled device (CCD) sensors) and features the same interface specificity. Today, commercial OPA systems pumped by kHz femtosecond Ti:sapphire lasers provide tunable (~ 0.21 to $16\,\mu$m) and broadband IR

pulses.[86,88] In combination with narrowband visible pulses, this widespread configuration enables multiplex probing of the vibrational resonances and therefore drastically reduced accumulation times at a comparatively high signal-to-noise ratio.[89] Overviews of the manifold developments and applications of SFG spectroscopy, among these also phase-sensitive and time-resolved SFG setups as well as combinations of both,[90,91,92,93,94] can be found in literature.[86,95] Inter alia, SFG is frequently used to study water, as subphase, at its interface with a film, for instance, of lipids,[96,97,98,99] peptides, or proteins.[100,101,102,103]

The fundamentals of SFG vibrational spectroscopy are explained in the following section, as well as in Sections 2.1.2 and 2.1.1, where the practical aspects of an SFG experiment and the utilized SFG spectrometer setup are presented. The feature of phase sensitivity and challenges associated with its realization are in particular discussed in Section 2.1.3 and in Chapter 3, which presents a new type of phase-resolved SFG spectrometer.

1.3.1 Nonlinear Optical Wave Equation

To understand the origin of the phenomena SHG and SFG, and in particular the fundamentals of SFG spectroscopy, we have to comprehend the consequences of a material's response which is not linear to an applied field. The equations and derivations in this section were selected from literature and describe the origin of SFG phenomenologically, using an electromagnetic approach.[86,104,105]

The evolution of light, an electromagnetic wave, is described by Maxwell's equations (SI units): *

$$\nabla \cdot \widetilde{\boldsymbol{D}} = \widetilde{\rho} \tag{1.4}$$

$$\nabla \cdot \widetilde{\mathbf{B}} = 0 \tag{1.5}$$

$$\nabla \times \widetilde{\boldsymbol{E}} = -\frac{\partial \widetilde{\mathbf{B}}}{\partial t} \tag{1.6}$$

$$\nabla \times \widetilde{\mathbf{H}} = \frac{\partial \widetilde{\boldsymbol{D}}}{\partial t} + \widetilde{\mathbf{J}}, \tag{1.7}$$

where $\widetilde{\boldsymbol{D}}$ is the dielectric displacement field, $\widetilde{\mathbf{B}}$ the magnetic flux density and $\widetilde{\boldsymbol{E}}$ and $\widetilde{\mathbf{H}}$ the electric and magnetic field strengths, respectively. In the absence of free charges, the charge and current densities, $\widetilde{\rho}(\mathbf{r}, t)$ and $\widetilde{\mathbf{J}}(\mathbf{r}, t)$, are

$$\widetilde{\rho} = 0 \tag{1.8}$$

$$\widetilde{\mathbf{J}} = 0. \tag{1.9}$$

The dielectric and magnetic properties of the material are considered in the quantities $\widetilde{\boldsymbol{D}}$ and $\widetilde{\mathbf{B}}$, which are linked to $\widetilde{\boldsymbol{E}}$ and $\widetilde{\mathbf{H}}$ by

$$\widetilde{\boldsymbol{D}} = \epsilon_0 \widetilde{\boldsymbol{E}} + \widetilde{\boldsymbol{P}} \tag{1.10}$$

$$\widetilde{\mathbf{B}} = \mu_0 \widetilde{\mathbf{H}} + \widetilde{\mathbf{M}}, \tag{1.11}$$

where ϵ_0 and μ_0 are the permittivity and the permeability of free space, respectively. Here, it is further assumed that the magnetization of the material is negligible ($\widetilde{\mathbf{M}} \approx 0$).

---

*The following conventions were applied in agreement with the denotation in *Boyd* (2008):[104] Bold letters denote vectors; $\widetilde{}$ accents denote quantities that vary rapidly in time.

The Maxwell equations (1.6) and (1.7) are coupled via (1.10) and (1.11). Therefore, the **wave equation** can be derived utilizing the approach $\nabla \times$ (1.6):

$$\nabla \times \nabla \times \widetilde{\boldsymbol{E}} = -\mu_0 \frac{\partial}{\partial t}(\nabla \times \widetilde{\mathbf{H}}) \tag{1.12}$$

Substituting $\nabla \times \widetilde{\mathbf{H}}$ according to (1.7) and (1.9), replacing $\widetilde{\boldsymbol{D}}$ by the relation (1.10), and rearranging yields

$$\nabla \times \nabla \times \widetilde{\boldsymbol{E}} + \frac{1}{c^2}\frac{\partial^2}{\partial t^2}\widetilde{\boldsymbol{E}} = -\frac{1}{\epsilon_0 c^2}\frac{\partial^2}{\partial t^2}\widetilde{\boldsymbol{P}}. \tag{1.13}$$

The **electromagnetic** or **optical wave equation** describes the propagation of light in a medium and thereby connects the electric field with the polarization in the material. Here, the relation

$$c^2 = \frac{1}{\mu_0 \epsilon_0} \tag{1.14}$$

has been applied, as it can be shown that c is the speed of light in vacuum.

$\widetilde{\boldsymbol{P}}$ can already be a nonlinear response with respect to an applied field, however, in order to demonstrate the implications of this nonlinearity, a few more considerations are useful:

Initially, a mathematical identity allows rewriting the first term of the left-hand side as

$$\nabla \times \nabla \times \widetilde{\boldsymbol{E}} = \nabla(\nabla \cdot \widetilde{\boldsymbol{E}}) - \nabla^2 \widetilde{\boldsymbol{E}}. \tag{1.15}$$

The Helmholtz theorem allows to write the vector field $\widetilde{\boldsymbol{E}}$ as the sum of its *transverse* and its *longitudinal* part:[106]

$$\widetilde{\boldsymbol{E}} = \widetilde{\boldsymbol{E}}^{\perp} + \widetilde{\boldsymbol{E}}^{\parallel}, \tag{1.16}$$

where the transverse part denotes the component with zero divergence and the longitudinal part the component with zero curl:

$$\nabla \cdot \widetilde{\boldsymbol{E}}^{\perp} = 0 \tag{1.17}$$

$$\nabla \times \widetilde{\boldsymbol{E}}^{\parallel} = 0 \tag{1.18}$$

It can be shown, that the longitudinal field $\widetilde{\boldsymbol{E}}^{\parallel}$ does not propagate; therefore, assuming a transverse field $\widetilde{\boldsymbol{E}} = \widetilde{\boldsymbol{E}}^{\perp}$ allows to apply (1.17) to the term $\nabla(\nabla \cdot \widetilde{\boldsymbol{E}})$ in (1.15).[106]

A shorter, more common expression of the wave equation (1.13) can then, after further

substitution according to (1.10), be written as

$$\nabla^2 \widetilde{\boldsymbol{E}} - \frac{1}{\epsilon_0 c^2} \frac{\partial^2}{\partial t^2} \widetilde{\boldsymbol{D}} = 0. \tag{1.19}$$

In nonlinear optics, the relation (1.10) between $\widetilde{\boldsymbol{E}}$ and $\widetilde{\boldsymbol{D}}$ can be written as:

$$\widetilde{\boldsymbol{P}} = \widetilde{\boldsymbol{P}}^{(1)} + \widetilde{\boldsymbol{P}}^{(NL)} \tag{1.20}$$

$$\widetilde{\boldsymbol{D}} = \epsilon_0 \widetilde{\boldsymbol{E}} + \widetilde{\boldsymbol{P}}^{(1)} + \widetilde{\boldsymbol{P}}^{(NL)} = \widetilde{\boldsymbol{D}}^{(1)} + \widetilde{\boldsymbol{P}}^{(NL)}, \tag{1.21}$$

where $\widetilde{\boldsymbol{P}}$ and $\widetilde{\boldsymbol{D}}$ are split into linear and nonlinear parts, respectively.

Finally, the linear component of $\widetilde{\boldsymbol{D}}$ can be substituted by

$$\widetilde{\boldsymbol{D}}^{(1)} = \epsilon_0 \boldsymbol{\epsilon}^{(1)} \cdot \widetilde{\boldsymbol{E}}, \tag{1.22}$$

introducing the linear dielectric tensor $\boldsymbol{\epsilon}^{(1)}$. In isotropic media this simplifies to

$$\widetilde{\boldsymbol{D}}^{(1)} = \epsilon_0 \epsilon^{(1)} \cdot \widetilde{\boldsymbol{E}}. \tag{1.23}$$

The wave equation can now be rewritten as

$$-\nabla^2 \widetilde{\boldsymbol{E}} + \frac{\epsilon^{(1)}}{c^2} \frac{\partial^2 \widetilde{\boldsymbol{E}}}{\partial t^2} = -\frac{1}{\epsilon_0 c^2} \frac{\partial^2}{\partial t^2} \widetilde{\boldsymbol{P}}^{(NL)}. \tag{1.24}$$

The **nonlinear optical wave equation** in this form is valid for isotropic, dispersionless material without dissipation, which shall be sufficient for the scope of this introductory section. It illustrates the role of the nonlinear polarization $\widetilde{\boldsymbol{P}}^{(NL)}$, which can be interpreted as a source term, responsible for the appearance of the new field components discussed in the next section.

1.3.2 Probing the Second-order Nonlinear Susceptibility

As indicated in the previous section, in linear optics the induced polarization in a material depends linearly on the electric field:

$$\widetilde{\boldsymbol{P}}(t) = \epsilon_0 \boldsymbol{\chi}^{(1)} \widetilde{\boldsymbol{E}}(t), \tag{1.25}$$

where $\boldsymbol{\chi}^{(1)}$ is the linear dielectric susceptibility tensor. It is therefore defined as the proportionality constant between the electric field and the dielectric displacement:

$$\widetilde{\boldsymbol{D}} = \epsilon_0 \widetilde{\boldsymbol{E}} + \widetilde{\boldsymbol{P}}^{(1)} = \epsilon_0 (1 + \boldsymbol{\chi}^{(1)}) \widetilde{\boldsymbol{E}} \tag{1.26}$$

A nonlinear response to the applied field can be described by expressing $\widetilde{\boldsymbol{P}}(t)$ as a power series in $\widetilde{\boldsymbol{E}}$:[86,104]

$$\widetilde{\boldsymbol{P}}(t) = \epsilon_0 (\boldsymbol{\chi}^{(1)} \widetilde{\boldsymbol{E}}(t) + \boldsymbol{\chi}^{(2)} \widetilde{\boldsymbol{E}}^2(t) + \boldsymbol{\chi}^{(3)} \widetilde{\boldsymbol{E}}^3(t) + ...) \tag{1.27}$$

$$= \widetilde{\boldsymbol{P}}^{(1)} + \widetilde{\boldsymbol{P}}^{(2)} + \widetilde{\boldsymbol{P}}^{(3)} + ..., \tag{1.28}$$

where the nonlinear susceptibilities $\boldsymbol{\chi}^{(2)}$ and $\boldsymbol{\chi}^{(3)}$ are considerably smaller than the linear susceptibility $\boldsymbol{\chi}^{(1)}$ and result therefore only at high incident field strengths in a detectable signal.

Considering the second-order contribution of the nonlinear polarization

$$\widetilde{\boldsymbol{P}}^{(2)}(t) = \epsilon_0 \boldsymbol{\chi}^{(2)} \widetilde{\boldsymbol{E}}(t)^2 \tag{1.29}$$

it becomes evident that for an incident field

$$\widetilde{\boldsymbol{E}}(t) = \boldsymbol{E}_1 e^{-i\omega_1 t} + c.c.^* \tag{1.30}$$

an additional frequency component $2\omega_1$, the second harmonic, emerges. Going one step further, the second-order polarization induced by two distinct incident fields

$$\widetilde{\boldsymbol{E}}(t) = \boldsymbol{E}_1 e^{-i\omega_1 t} + \boldsymbol{E}_2 e^{-i\omega_2 t} + c.c. \tag{1.31}$$

---

*c.c.: complex conjugated

is given by

$$
\begin{aligned}
\widetilde{\boldsymbol{P}}^{(2)}(t) = \epsilon_0 \boldsymbol{\chi}^{(2)} [&\boldsymbol{E}_1^2 e^{-i2\omega_1 t} + \boldsymbol{E}_2^2 e^{-i2\omega_2 t} \\
&+ 2\boldsymbol{E}_1 \boldsymbol{E}_2 e^{-i(\omega_1+\omega_2)t} + 2\boldsymbol{E}_1 \boldsymbol{E}_2^* e^{-i(\omega_1-\omega_2)t} + c.c.] \\
&+ 2\epsilon_0 \boldsymbol{\chi}^{(2)} [\boldsymbol{E}_1 \boldsymbol{E}_1^* + \boldsymbol{E}_2 \boldsymbol{E}_2^*].
\end{aligned}
\tag{1.32}
$$

The frequencies $2\omega_1$ and $2\omega_2$ correspond again to the second harmonics of the respective incident beams frequencies (SHG). However, now further additional frequencies appear, which are of the sum of ω_1 and ω_2 (SFG) and also of their difference, designated as difference frequency generation (DFG). DFG is another important process which is utilized, for instance, for the generation of laser light in the mid-IR frequency range (Section 2.1.1). The remaining term is frequency-independent and describes the occurrence of a DC field, also known as optical rectification (OR).

From (1.32) we can extract the expression for the second-order nonlinear polarization describing the process of SFG:

$$
\widetilde{\boldsymbol{P}}^{(2)}(t) = 2\epsilon_0 \boldsymbol{\chi}^{(2)} \boldsymbol{E}_{VIS} \boldsymbol{E}_{IR} e^{-i(\omega_{VIS}+\omega_{IR})t}
\tag{1.33}
$$

In order to probe the vibrational resonances at the surface, a typical SFG experiment utilizes mid-IR pulses (further referred to as IR), overlapped with non-resonant upconversion pulses in the near-IR/visible region (VIS) in space and time. The energy scheme in case of a resonant SFG process is illustrated in Figure 1.6.

1.3.2.1 Interface Specificity and Symmetry Considerations

The complex amplitude of the nonlinear polarization which describes SFG can be written as[105]

$$
\boldsymbol{P}_{SF,i}^{(2)} = 2\epsilon_0 \boldsymbol{\chi}_{ijk}^{(2)} \boldsymbol{E}_{VIS,j} \boldsymbol{E}_{IR,k}.
\tag{1.34}
$$

The Cartesian indices ijk can be freely interchanged, considering that each of three field vectors can have components in each of the three dimensions x, y and z. $\boldsymbol{P}_{SF,i}^{(2)}$ therefore describes one of $3^3 = 27$ possible vector combinations, which add up to the complete response

$$
\boldsymbol{P}_{SF}^{(2)} = \sum_i^{x,y,z} \boldsymbol{P}_{SF,i}^{(2)} = 2\epsilon_0 \sum_i^{x,y,z} \sum_j^{x,y,z} \sum_k^{x,y,z} \boldsymbol{\chi}_{ijk}^{(2)} \boldsymbol{E}_{VIS,j} \boldsymbol{E}_{IR,k}
\tag{1.35}
$$

from the surface.

The interface specificity of second-order nonlinear spectroscopy can be derived from consideration of $\chi_{ijk}^{(2)}$.[105] In centrosymmetric media, inversion symmetry demands that

$$\chi_{ijk}^{(2)} = \chi_{-i-j-k}^{(2)}, \tag{1.36}$$

i.e., the value of $\chi_{ijk}^{(2)}$ is equal for opposing directions. However, within the electric dipole approximation, the third-rank tensor $\chi_{ijk}^{(2)}$ describes the material's response to the incident light according to

$$\chi_{ijk}^{(2)} \propto \mu_i \mu_j \mu_k \tag{1.37}$$

and must therefore reverse sign upon inversion transformation. A reversion of all three axes gives

$$\chi_{-i-j-k}^{(2)} = (-1)^3 \chi_{ijk}^{(2)} = -\chi_{ijk}^{(2)}. \tag{1.38}$$

Both equations, (1.36) and (1.38), cannot be satisfied at the same time, except for $\chi_{ijk}^{(2)} = 0$, which thus excludes second-order nonlinear responses from the bulk of centrosymmetric media. The same can be shown for all higher even-order responses. As the centrosymmetry is inherently broken at interfaces, detectable signal ideally originates solely from the interfacial monolayer of molecules. Being based on the electric dipole approximation, validity of this assumption depends on the respective sample and experimental conditions.[107]

Figure 1.7 depicts a typical beam configuration of an SFG experiment. Here, the spatially and temporally overlapping IR and VIS beams share the same plane of incidence. The **phase-matching condition**

$$n_{SFG}k_{SFG}\sin\theta_{SFG} = n_{VIS}k_{VIS}\sin\theta_{VIS} + n_{IR}k_{IR}\sin\theta_{IR}, \tag{1.39}$$

where k_{SFG}, k_{VIS} and k_{IR} are the magnitudes of the beams' wave vectors, respectively, is derived from the conservation of momentum for the wave vectors' projections on the x-axis. It thereby determines the angle θ_{SFG} of the emitted SFG light in dependence of the incidence angles θ_{VIS} and θ_{IR}.

In addition to the principal surface specificity, the 27 tensor elements of $\chi_{ijk}^{(2)}$ reduce to only 4 distinct, unique components when probing media with isotropic surfaces, for
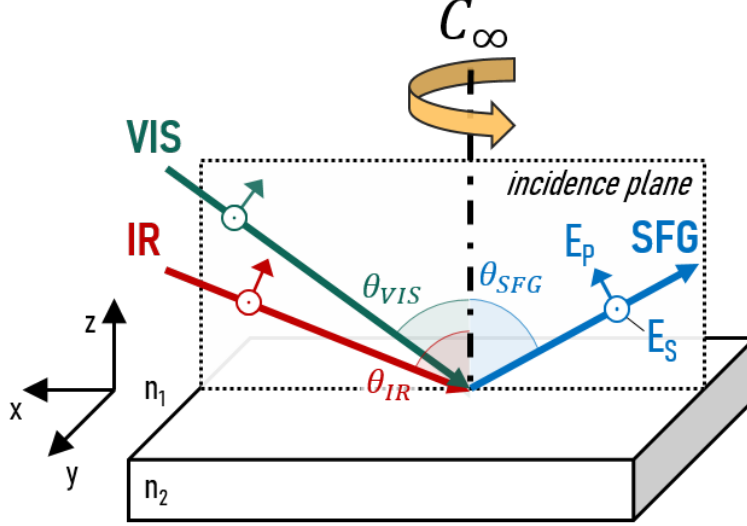
Figure 1.7: Beam geometry of a typical SFG experiment - All beams share the same incidence plane and are dividable into two polarization components; one in-plane, parallel component P and one out-of-plane, perpendicular component S (exemplarily labeled for the SFG beam). n_1 and n_2 denote the refractive indices of medium 1 and medium 2, respectively. The reflections of the incident beams were omitted in favor of clarity.

instance, liquids like water. In these cases, we can assume C_∞ symmetry around the z-axis, i.e, the x and y components are inversion invariant, and a non-zero, contributing component of $\chi_{ijk}^{(2)}$ does not change its sign upon reversion of the x- or y-axis. Reversing one individual axis, however leads to the same result as in (1.38). Therefore, only the following seven vector combinations, respectively four differing, independent components of $\chi_{ijk}^{(2)}$ remain:[105]

$$\chi_{zxx}^{(2)}(\equiv \chi_{zyy}^{(2)}); \quad \chi_{xzx}^{(2)}(\equiv \chi_{yzy}^{(2)}); \quad \chi_{xxz}^{(2)}(\equiv \chi_{yyz}^{(2)}); \quad \chi_{zzz}^{(2)} \tag{1.40}$$

Those elements can be particularly probed utilizing different polarization combinations of incident beams and SFG signal as listed in Table 1.1.

1.3.2.2 Fresnel Factors and the SFG Intensity

To correlate the measured SFG intensity with the probed elements of $\chi_{ijk}^{(2)}$, the relations between the incident beams, the induced polarization in an interfacial layer (Eq. (1.35)) and the emitted electric field have to be described. To this end, the SFG intensity can

Table 1.1: Polarization Combinations and probed elements of $\chi_{ijk}^{(2)}$ - The polarization combinations are denoted with decreasing frequency.

Polarization Combination (SFG, VIS, IR)	$\chi_{ijk}^{(2)}$ Elements
PSS	$\chi_{zyy}^{(2)}$
SPS	$\chi_{yzy}^{(2)}$
SSP	$\chi_{yyz}^{(2)}$
PPP	$\chi_{zzz}^{(2)}, \chi_{zxx}^{(2)}, \chi_{xzx}^{(2)}, \chi_{xxz}^{(2)}$

be expressed as follows:[108,109]

$$\boldsymbol{I}_{SFG}(\omega_{SFG}) \propto \left|\boldsymbol{\chi}_{eff}^{(2)}\right|^2 \boldsymbol{I}_{VIS}(\omega_{VIS})\boldsymbol{I}_{IR}(\omega_{IR}) \tag{1.41}$$

The effective nonlinear susceptibility $\boldsymbol{\chi}_{eff}^{(2)}$ is given by

$$\chi_{eff}^{(2)} = [\hat{\boldsymbol{e}}(\omega_{SFG})\boldsymbol{L}(\omega_{SFG})]\,\boldsymbol{\chi}_{ijk}^{(2)}\,[\boldsymbol{L}(\omega_{VIS})\hat{\boldsymbol{e}}(\omega_{VIS})][\boldsymbol{L}(\omega_{IR})\hat{\boldsymbol{e}}(\omega_{IR})]. \tag{1.42}$$

Here, $\hat{\boldsymbol{e}}(\omega)$ denote the unit polarization vectors and $\boldsymbol{L}(\omega)$ the Fresnel factors for the frequencies of the three electric fields (SFG, VIS and IR), respectively. Summarizing, these coefficients consider that the nonlinear polarization is generated by the total electric field of the incident beams in an interfacial layer, and they combine the phase-matching condition (Eq. (1.39)) for the emitted SFG light with the continuity of the electric fields across the interface. The definition of the Fresnel factors and the full set of equations that describe the effective responses $\chi_{eff}^{(2)}$ for the four polarization combinations (for instance, $\boldsymbol{\chi}_{eff,SSP}^{(2)}$) and their relations to the elements of $\chi_{ijk}^{(2)}$ (in that case $\boldsymbol{\chi}_{yyz}^{(2)}$), can be found in literature.[105,108,109,110,111]

For the calculations, the setup-specific incident angles and the refractive indices of the media are required. A substantial modulation of probed spectra can be observed for buried interfaces, specifically when using prisms as in total internal reflection geometry.[112,113,114,115] Within the studies of water/air or water/protein film interfaces described in this thesis, the Fresnel factors played a minor role, as primarily relative intensity changes were analyzed and data were not compared between different setup geometries. In the following chapters, $\chi_{eff}^{(2)}$ is hence abbreviated as $\chi^{(2)}$, without indices.

1.3.2.3   The Molecular Hyperpolarizability

So far, SFG has been described as the macroscopic response of a material to incident light. The quantum mechanical description is beyond the scope of this introduction,[86,104,106] however, some relations between the SFG response and its molecular-level origin are useful for the interpretation of the obtained spectra:[105,110]

The macroscopic second-order nonlinear susceptibility $\chi^{(2)}_{ijk}$ tensor is related to the molecular hyperpolarizability $\beta_{i'j'k'}$ of the molecules in the given ensemble by

$$\chi^{(2)}_{ijk} = N \sum_{i'j'k'} \langle R_{ii'} R_{jj'} R_{kk'} \rangle \beta^{(2)}_{i'j'k'} \tag{1.43}$$

The Euler rotation matrices $R_{ii'}$, $R_{jj'}$ and $R_{kk'}$ convert from the molecular to the surface coordinate system.[116] The $\langle \rangle$ brackets indicate an orientational average over a number density N of molecules at the interface. The full expression of $\beta_{i'j'k'}$ can be derived using perturbation theory.[87,104] In case of resonant SFG spectroscopy (Figure 1.6), as commonly used to probe the vibrational spectra of a system, it can be simplified as

$$\beta^{(2)}_{i'j'k'} = \beta^{(2)}_{NR} + \sum_q \frac{\beta^q_{i'j'k'}}{(\omega_{IR} - \omega_q + i\Gamma_q)}. \tag{1.44}$$

The first term represents non-resonant contributions to $\beta^{(2)}_{i'j'k'}$. The so-called *sum-frequency strength factor* tensor $\beta^q_{i'j'k'}$ is described by[90,117]

$$\beta^q_{i'j'k'} = -\frac{1}{2\epsilon_0\omega_q} \frac{\partial \alpha^{(1)}_{i'j'}}{\partial Q_q} \frac{\partial \mu_{k'}}{\partial Q_q}, \tag{1.45}$$

where $\partial \alpha^{(1)}_{i'j'}/\partial Q_q$ and $\partial \mu_{k'}/\partial Q_q$ are the partial derivatives of the Raman polarizability tensor and of the IR dipole moment surface of the qth vibrational mode, respectively. Q_q represents the normal coordinate of the respective mode.

These expressions, (1.43), (1.44) and (1.45), are sufficient to address some essential aspects. First, (1.43) provides a tangible explanation why $\chi^{(2)}_{ijk}$ becomes zero in the bulk of most materials, which is the vectorial averaging over the orientations of the molecules. This ensemble average is zero in centrosymmetric crystals and, as evident from this expression, also in gas or liquid were the molecules are randomly oriented. A net orientation of the molecular dipole moments is only found at interfaces, where the

symmetry is broken and their electric fields do not cancel out.

Further, (1.44) shows that $\boldsymbol{\beta}_{i'j'k'}$, and therefore the susceptibility $\boldsymbol{\chi}^{(2)}_{ijk}$, get resonantly enhanced if the tunable IR frequency ω_{IR} coincides with the frequency of a vibrational mode ω_q. Γ_q^{-1} serves as a damping term and describes spectral broadening, which is, inter alia, determined by the relaxation time of the excited state and dephasing. The resulting description of a resonance's line shape is a Lorentzian. In case of dielectric interfaces, the non-resonant contribution is usually small and real-valued, and experimentally probed resonances can hence be fitted presuming Lorentzian line shapes.

Finally, (1.45) elucidates that a probeable vibrational mode has to be both, Raman and IR active, which is the transition selection rule of SFG. This is also intuitive considering the energy diagram in Figure 1.6, which resembles an IR excitation, followed by an anti-Stokes Raman-shifted emission.

2

Experimental Methods

2. EXPERIMENTAL METHODS

2.1 Sum-Frequency Generation Vibrational Spectroscopy

The fundamentals of SFG have been introduced in Section 1.3. This section is divided in three parts: 2.1.1 and 2.1.2 give a brief description of a conventional SFG setup and deals with the methodology of an SFG experiment and the evaluation and basic interpretation schemes of the obtained data. 2.1.3 describes the fundamentals of phase-resolved SFG (PR-SFG), its advantages, technical challenges, and data evaluation as a basis for the discussions in Chapter 3.

2.1.1 SFG Spectrometer

Figure 2.1 illustrates the utilized SFG spectrometer setup as used for the experiments described in Chapters 4, 5, and 6. Seed pulses with a spectral bandwidth of $\sim 60\,\mathrm{nm}$ are generated in a Ti:sapphire laser oscillator (*seed*, Mai Tai, Spectra-Physics). These pulses are amplified in a regenerative amplifier (Spitfire Ace, Spectra-Physics), which is pumped by a Nd:YLF (neodymium-doped yttrium lithium fluoride) laser (Empower, Spectra-Physics). The output ($\sim 5\,\mathrm{mJ}$ pulses, centered at $\sim 800\,\mathrm{nm}$ and with a spectral bandwidth $\sim 60\,\mathrm{nm}$) is divided by a beam splitter. Around $1.7\,\mathrm{mJ}$ is utilized in a commercial optical parametric amplifier (OPA; TOPAS-C, Spectra-Physics) to generate signal and idler (*sig*, *id*) pulses, which are mixed either in a silver gallium disulfide (AgGaS$_2$, IR $\sim 3000\,\mathrm{nm}$) or in a gallium selenide (GaSe, IR $\geq 4000\,\mathrm{nm}$) collinear difference-frequency generation (DFG) crystal unit. The generated mid-infrared (IR) pulses have an energy of ~ 4–$8\,\mathrm{\mu J}$, with a FWHM of ~ 350–$550\,\mathrm{cm^{-1}}$, both depending on the operating central wavelength. The remaining signal and idler pulses are blocked by a longpass filter (*LP*). The output polarization is horizontal and can be rotated to vertical using a halfwave plate ($\lambda/2$). A wire-grid polarizer (*P*) is used to define the transmitted polarization.

The narrowband visible upconversion pulses ($25\,\mathrm{mJ}$; FWHM $\sim 15\,\mathrm{cm^{-1}}$) are obtained by passing another fraction ($\sim 1\,\mathrm{mJ}$) of the broadband $800\,\mathrm{nm}$ amplifier output through a Fabry-Perot etalon (SLS Optics Ltd.). A delay stage is used to adjust the temporal overlap of the VIS and IR pulses on the sample surface. A combination of a cube polarizer (*P*) and two halfwave plates is used to set the polarization and to decrease the intensity of the VIS pulses.

The VIS and IR beams are focused by plano-convex lenses (L_{VIS}, $+250\,\text{mm}$ and L_{IR}, $+50\,\text{mm}$ focal length) and spatially overlapped on the sample surface with incident angles of 36° and 41° with respect to the surface normal.

The SFG signal from the sample is collimated by another plano-convex lens (L_{SFG}, $+250\,\text{mm}$). A half-wave plate and a cube polarizer are used to set the detected polarization. A shortpass filter (SP) removes residual reflected/scattered VIS light before the signal is focused on the entrance slit of a spectrograph (Acton SP 300i, Princeton Instruments) by a plano convex lens (L_{spec}, $+50\,\text{mm}$). The dispersed signal is accumulated by a charge-coupled device (CCD) camera (Newton 970, Andor Technologies).
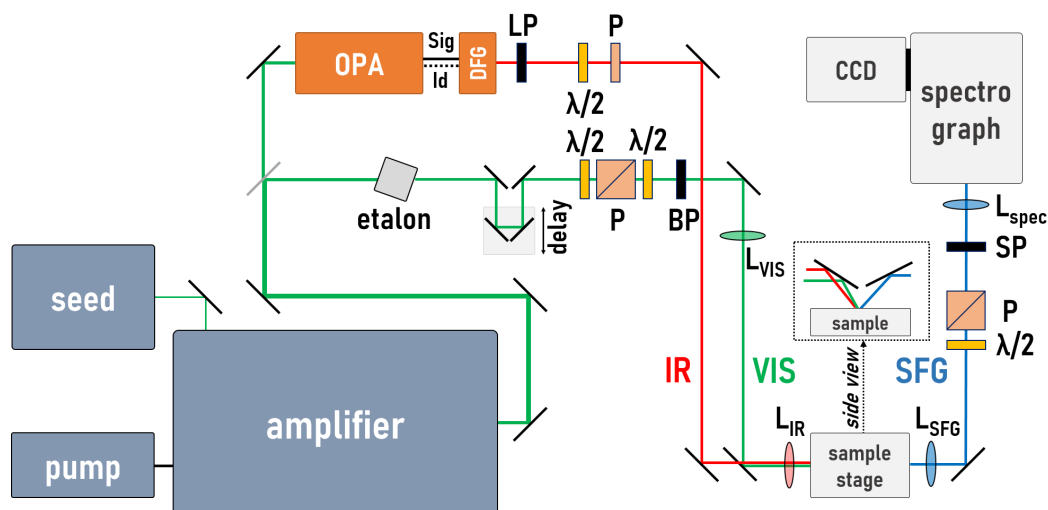
Figure 2.1: SFG spectrometer - The SFG spectrometer setup as it was used for the experiments of the Chapters 4 to 6.

2. EXPERIMENTAL METHODS

2.1.2   SFG Experiment

In the SFG experiments (Figure 2.2), the vibrational resonances with frequencies within the broad spectral bandwidth of the IR pulses were probed simultaneously. The SFG spectra were in the range of ~ 620 to $710\,\text{nm}$ ($\sim 14\,100$ to $16\,100\,\text{cm}^{-1}$), depending on the investigated IR frequency range. The fixed central frequency of the narrowband VIS pulses ($\sim 12\,500\,\text{cm}^{-1}$) was subtracted from the frequencies of the acquired SFG spectra to display them over the IR wavenumber. The bandwidth of the VIS ($\sim 15\,\text{cm}^{-1}$) therefore limited the spectral resolution.

Background signals from residual VIS and room light were acquired at blocked IR beam and subtracted from the raw spectra.
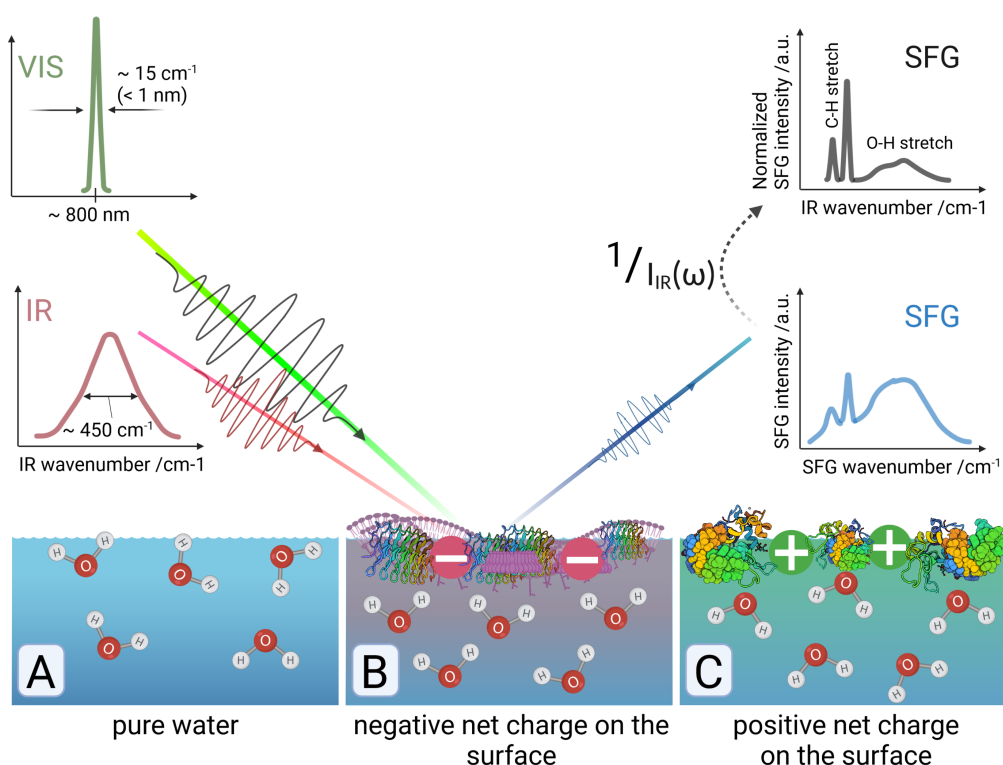
Figure 2.2: SFG experiment - Illustration of an SFG experiment as conducted with the bacterial/INP solutions. The narrowband VIS upconversion pulses were fixed at a central wavelength $\sim 800\,\text{nm}$. The central wavenumber of the broadband IR was varied depending on the region of interest. (A) depicts the neat water/air interface. In (B) and (C), the interfacial water molecules (represented by enlarged illustrations) are aligned by the respective electric fields from the net charges of applied films (e.g., bacterial fragments or proteins).

To obtain the correct shape of a spectrum, the intensity profile of the IR spectra has to be considered. Therefore, the background-subtracted raw spectra were normalized by dividing them by the IR spectrum, which was determined by measuring the non-resonant signal from z-cut quartz (zqz) and subtracting the corresponding background signal.

The sample solutions were filled in PTFE troughs with a diameter of $\sim 3\,\text{cm}$ or $\sim 8\,\text{cm}$ and a volume of $\sim 6\,\text{mL}$ or $\sim 20\,\text{mL}$, respectively. The temperature-controlled experiments were conducted in a PTFE-coated aluminum trough ($\sim 20\,\text{mL}$), mounted on two Peltier elements. The temperature uncertainty was around $\pm 0.5\,°\text{C}$. The measurements of protein and bacterial fragments in solution were based on their affinity to accumulate at the surface. Measurements of the surface tension showed a decrease over several minutes up to two hours, before stabilizing at a minimum, indicating the equilibrium. Further details are described in the respective Supporting Information to each chapter.

Interpretation of SFG Intensity Spectra

In terms of the interpretation of SFG spectra, it is helpful to combine the equations (1.41) and (1.43) from Section 1.3 to

$$I_{SFG} \propto |E_{SFG}|^2 \propto \left|\boldsymbol{\chi}^{(2)}\right|^2 \propto N^2 \left|\left\langle\boldsymbol{\beta}^{(2)}\right\rangle\right|^2. \tag{2.1}$$

The relative intensity of the emitted SFG light for a given IR wavenumber scales with the square of the number density of contributing oscillators. Moreover, it is sensitive to their average alignment: The intensity increases with an increased ordering of the molecules, which is a powerful feature of SFG spectroscopy.

As a reference for the influence of the sample on the interfacial water molecules, we conducted measurements of the neat H_2O/air, respectively the D_2O/air interface (Figures 2.2 A and 2.3). The signal is comparatively weak and is known to consist of two major contributions in the investigated O–H stretch, respectively O–D stretch, region. Thereof, the most important within this thesis is the broad band from ~ 3100–$3500\,\text{cm}^{-1}$ (H_2O), respectively ~ 2200–$2600\,\text{cm}^{-1}$ (D_2O). This band arises, inter alia, from the continuum of individual hydrogen/deuterium bond strengths of the single water molecules, which influence the respective intra-molecular strengths of the O–H/O–D stretch vibrations. Shifts of this band can therefore be interpreted in terms of a change

in the hydrogen bond network, i.e., red-shifts of the spectral centroid indicate stronger inter-molecular bonds.[118,119] This effect is, for instance, observed upon a decrease of the temperature.

A second contribution to the spectrum is a sharp peak at $\sim 3720\,\text{cm}^{-1}$, respectively $\sim 2720\,\text{cm}^{-1}$ in case of D_2O. It hat its origin in the so-called free O–H (free O–D) stretch vibrations of H-/D-atoms, which protrude from the surface and are not hydrogen-bonded. It therefore disappears upon formation of a film, for instance, of proteins or bacterial fragments, on the surface.
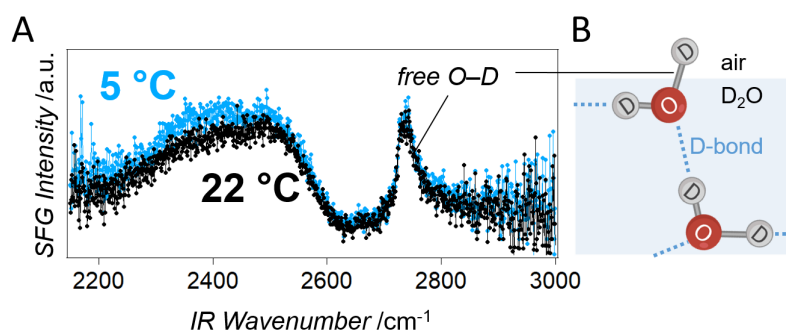
Figure 2.3: SFG spectra of D_2O at room temperature and at 5 °C - (A) The spectrum consists of a broad band from the D-bonded O–D stretch vibrations and a narrow band from the *free O–D* vibrations, both visualized in (B). The normalized SFG spectrum of D_2O 1 °C above its melting point reveals that the intensity of the D-bonded O–D stretch region is increased and the spectral centroid is shifted to slightly lower frequencies at low temperatures.

The investigated proteins mostly possessed strong net charges, which resulted in an alignment of the adjacent water molecules and, therefore, to a drastically increased O–H, respectively O–D stretch signal. This net charge was negative in the case of the bacterial INP samples and led to an alignment as depicted in Figure 2.2 B. In "conventional" SFG, direct information on the sign of the probed interfacial resonances is lost due to the squaring of the electric field (2.1). For this reason, phase-resolved variations of SFG spectroscopy have been developed, which are based on the interference between the SFG signal and a so-called *local oscillator* field. The basics of this technique are explained in the following section. Chapter 3 documents the development of such a setup and discusses some further challenges and advantages of PR-SFG in detail. At the same time, in many applications, the orientation of the water molecules can be derived from

the differing shapes of the conventional SFG intensity spectrum, which result from the shifted O–H, respectively O–D stretch bands upon a flip of the orientation and from the interference with the C–H stretch contributions. A demonstrative example for such a case is the SFG experiment to determine the interfacial isoelectric point of bacterial IN solutions, discussed in Chapter 4.

2.1.3 Phase-resolved SFG Spectroscopy

The SFG intensity is recorded as the square of the magnitude of the electric field as was shown in the previous sections:

$$I_{SFG} \propto |E_{SFG}|^2 \propto \left|\chi^{(2)}\right|^2 \tag{2.2}$$

This induces several disadvantages: The phase information of $\chi^{(2)}$ is lost and hence the valuable information on the orientation (up/down) of the interfacial molecules, as briefly discussed above. Further, the $\left|\chi^{(2)}\right|^2$ spectral band of a resonance is asymmetrically distorted and shifted compared to the "pure" imaginary part of $\chi^{(2)}$, which directly describes its resonant response (equations (1.43) and (1.44)). When the bands of multiple resonances overlap, this distortion additionally complicates the correct decomposition by fitting analysis.[95,120,121]

For these reasons, phase-resolved SFG spectroscopy, also referred to as phase-sensitive or heterodyne-detected SFG, has been developed to obtain the complex spectrum of $\chi^{(2)}$.[90,91,92,94] In this method, the interference between the SFG signal from the sample and an auxiliary electromagnetic wave, the *local oscillator* (LO), is detected (Figure 2.4).[93,121,122,123,124,125,126] The LO is usually generated by sum-frequency mixing of the IR and VIS fields in a medium, for instance a nonlinear crystal. This approach brings some additional, severe technical challenges into the design of an SFG setup. Here, and in Chapter 3, the basics of multiplex PR-SFG (utilizing broadband IR pulses) and some of those challenges are discussed.

Generally, the signal from the sample and the LO are collinearly directed to the spectrograph. Crucial for the phase-resolution, however, is the introduction of a time delay between both pulses. In absence of this delay, mixing the signal from the sample, E_{sa}, and the LO, E_{LO}, and detection in the frequency domain (intensity vs. frequency)
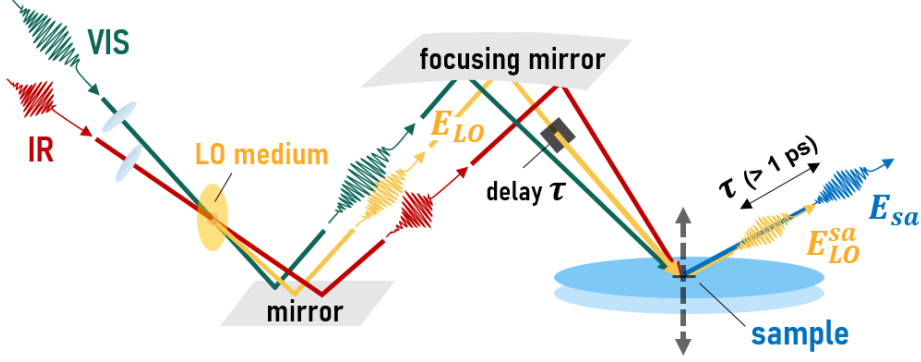
Figure 2.4: Exemplary schematic of a phase-resolved SFG setup - In this example for a noncollinear PR-SFG setup, the LO signal, E_{LO}, is generated before the sample and in transmission mode. The term noncollinear refers to the geometry of IR, VIS and LO beams. A glass plate introduces a delay τ of the E_{LO} signal pulse. All three beams are focused on the sample surface, where IR and VIS generate the sample signal E_{sa}. After its reflection from the surface, the LO signal beam is collinear to the sample signal beam. In this configuration, the relative phase between the two signals is very sensitive to the sample tilt and to its height (dashed arrow).

results in the following spectrum:

$$I_{SFG}(\omega_{SFG}) \propto |E_{SFG}|^2 = |E_{sa}|^2 + |E_{LO}|^2 + E_{sa}E_{LO}^* + E_{sa}^*E_{LO} \qquad (2.3)$$

The asterisks denote the complex conjugated electric fields. Although additional cross-terms with the unsquared fields appear, there is no way to disentangle the complex electric fields of sample and LO signal. The solution for this is to separate and extract one of the two cross-terms. To this end, a time delay τ is implemented between the two signals, which leads to a modulation of the spectrum (2.3):

$$I_{SFG}(\omega_{SFG}) \propto |E_{SFG}|^2 = |E_{sa}|^2 + |E_{LO}|^2 + E_{sa}E_{LO}^*e^{i\omega\tau} + E_{sa}^*E_{LO}e^{-i\omega\tau} \qquad (2.4)$$

This modulation over ω becomes visible in the spectrum as "fringes" (Figure 2.5 A), which are the key to the separation of the two cross-terms, and therefore the extraction of the phase information: The spectrum (2.4) is Fourier-transformed into the time domain (*IFFT*, Figure 2.5 B). Here, the slowly varying components, such as the squared terms, are found around 0, while the modulated cross-terms are shifted by $\pm\tau$, respectively, and are therefore separated from each other. The application of a window function extracts one of the cross-terms (here $+\tau$), which is then once more Fourier-transformed back into
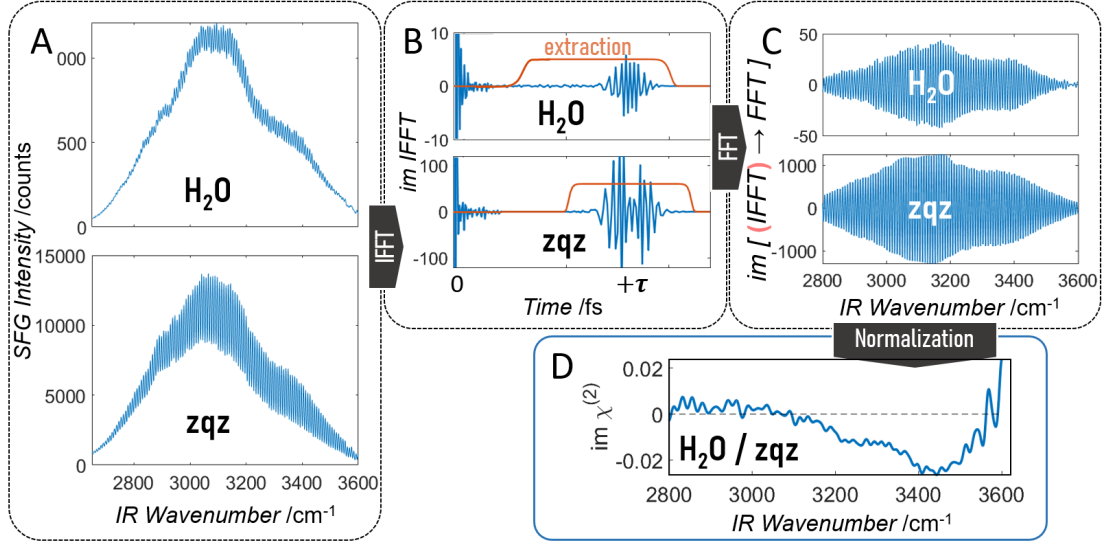
Figure 2.5: Processing of phase-resolved SFG data - The interferograms of water and the z-cut quartz reference are shown in (A). After inverse Fourier transformation (IFFT) into the time domain, a window-function is applied to extract the cross-term ((B), shown are the imaginary parts, respectively). A second Fourier transformation (FFT) yields the complex spectra in the frequency domain ((C), imaginary parts). (D) shows the imaginary part of the $\chi^{(2)}$ spectrum of water after normalization by the quartz spectrum. The data shown in this scheme correspond to the neat water-air interface spectra discussed in Chapter 3.

the frequency domain (*FFT*, Figure 2.5 C). The width of the window function around the signal determines the trade-off between resolution and noise. Normalization by the equally extracted cross-terms from the signal of a reference (for example z-cut quartz, *zqz*) gives then eventually the desired complex spectrum of $\chi_{sa}^{(2)}(\omega_{SFG})$ (Figure 2.5 D):[126]

$$\chi_{sa}^{(2)} \propto \frac{E_{sa}E_{LO}^{sa,*}e^{i\omega\tau}}{E_{ref}E_{LO}^{ref,*}e^{i\omega\tau}} \propto \frac{\chi_{LO}^{(2)}E_{IR}E_{VIS}}{\chi_{ref}^{(2)}\chi_{LO}^{(2)}E_{IR}E_{VIS}}\chi_{sa}^{(2)} \tag{2.5}$$

$\chi_{ref}^{(2)}$ and $\chi_{LO}^{(2)}$ describe the second-order susceptibilities of the reference and the material used for the generation of the LO, respectively.

While $\chi_{LO}^{(2)}$ cancels out, $\chi_{ref}^{(2)}$ can be considered to be a real-valued constant for the non-resonant response from the reference. $E_{LO}^{sa,*}$ and $E_{LO}^{ref,*}$ do not cancel out, as the effective signal from the LO reaching the detector is not the same for sample and reference measurements. For instance, in configurations where the LO is generated before the sample, as in Figure 2.4, it is reflected from the sample surface and hence depends

on the respective reflectivity. Therefore, the exact set of proportionality parameters to consider varies, depending on the setup configuration.

Various different implementations of PR-SFG setups have been realized over the years, with individual strengths and weaknesses. In Chapter 3, a novel PR-SFG setup design is presented, thereby also discussing some of these conceptional and technical aspects in more detail.

2.1.4 Pulse Shaper

The VIS pulses in the SFG spectrometer described above were generated by a Fabry-Perot etalon. An etalon is a robust and common way to create narrowband pulses for SFG experiments, however, it has some disadvantages. First of all, it is via design usually operated at a fixed output bandwidth. In our setup, the etalon transmitted pulses with a bandwidth $\sim 15\,\mathrm{cm}^{-1}$. This fixed bandwidth determines at the same time the pulse duration; the corresponding time profile, however, is asymmetric due to the working principle of the etalon (Figure 2.6). In short, the input is reflected multiple times between two windows, of which one transmits a portion of each reflection. The input angle α determines the path length between two reflections and, therefore, which wavelengths interfere constructively at the output. The asymmetric time profile of the VIS pulses from the etalon can be particularly problematic in the case of some phase-resolved setup configurations, like the implementation described in Chapter 3. Here, the VIS and IR have to overlap in the time domain at two different positions in the setup, at the LO medium and at the sample. The different group velocity dispersions (GVDs) of VIS and IR pulses can usually be readily compensated using a delay stage (Figure 2.1). However, the IR–VIS delay can be significantly different at the two positions (LO and sa), resulting in a situation as depicted in Figure 2.6 B. Depending on this timing difference between IR_{LO} and IR_{sa}, a compromise can be hard to find. Moreover, the steep flank of the etalon's time profile easily leads to distortions of the SFG spectra, or to a drastically increased dependence on the VIS–IR timing. In general, these properties of an etalon limit the versatility of the SFG spectrometer, which can be largely extended by replacing it by a pulse shaper. Its VIS pulse time profile is not only variable in duration; it also doesn't lead to distortions of the spectrum when the VIS–IR timing changes. Moreover, variability of the pulse duration is accompanied

by the possibility to vary the VIS pulse bandwidth and thus the spectral resolution of the experiment (see Section 2.1.2).
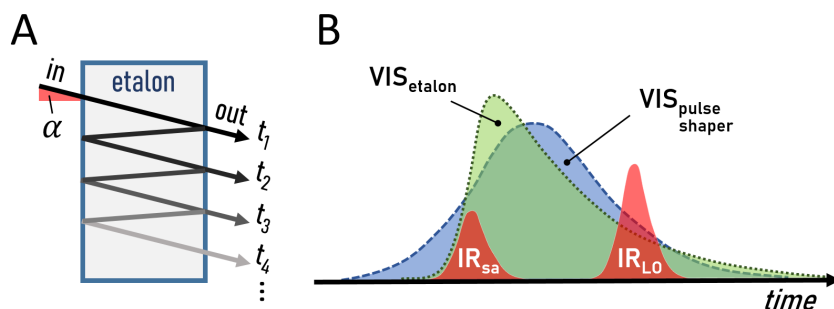

Figure 2.6: Illustrative comparison of visible pulse profiles from an etalon and from a pulse shaper in the time domain. - (A) The constructively interfering fractions of the etalon's output are delayed against each other (t_1, t_2, ...) and their intensities depend on the number of reflections within the etalon. This results in an asymmetric intensity profile in time: (B) Intensity over time for the VIS pulses from an etalon vs. the pulses from a pulse shaper. In case that time overlap has to be achieved at two positions in the setup, with different time delays between IR and VIS (e.g., at the sample and at the local oscillator as in Chapter 3), the pulse shaper's time-symmetric profile with a variable duration is particularly beneficial.

A simple implementation is a 4f pulse shaper,[127] as illustrated in Figure 2.7. The name refers to the beam path, which passes the focal length f of the utilized lenses four times. In Figure 2.7 A, the collimated beam is dispersed by a grating *G1*. The beam can now be understood as a bundle of collimated beams for each "color", which diverge from each other. The lens *L1* recollimates this bundle, which has now been expanded in the plane of the figure, due to the wavelength separation. Therefore, using a slit *S*, a narrow bandwidth of wavelengths can be selected to pass. The beam bundle is then focused by another identical lens *L2* and recombined by a second identical grating *G2* into a collimated beam with the desired narrow bandwidth.

In practice, it is possible to save space and costs by folding this geometry as in Figure 2.7 B, which is the configuration implemented in this work. *L1* only has to focus and collimate in the horizontal plane; therefore, we reduced the fluence on the dielectric mirror *DM* by using a cylindrical lens.

The single-color beams are focused by *L1*, which minimizes their spatial overlap at the slit. Therefore, the quality of this focusing is responsible for the reachable resolution. In the folded configuration the resolution is slightly decreased, as a perfect alignment
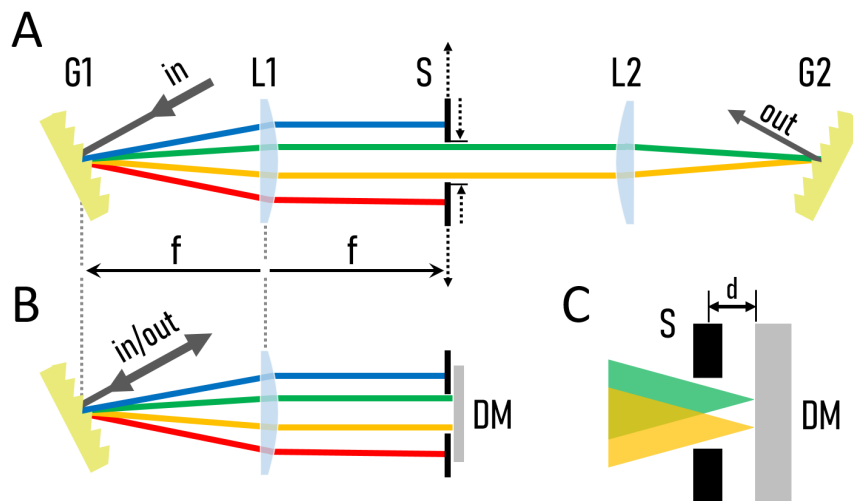
Figure 2.7: Schematic setup of a 4f pulse shaper - (A) 4f pulse shaper with two gratings, *G1* and *G2*, a slit *S* and two plano-convex lenses *L1* and *L2*. The central wavelength of the output is set by shifting the lateral position, the bandwidth by varying the width of the slit. (B) Alternative configuration with a folded geometry. The beam is backreflected by a dielectric mirror *DM*. (C) In the folded geometry the focus of the single color beams has to lie in the plane of *DM* instead of that of the slit (d ∼ 0.5 cm). Therefore, the achievable resolution is slightly reduced.

demands that the single colors are not focused directly on the plane of the slit but on the mirror (Figure 2.7 C). Backreflections from the slit can be eliminated by slightly tilting it against the perpendicular axis.

At a remaining VIS pulse energy of $\sim 20\,\mu$J (input $\sim 3.3\,$mJ), the implemented pulse shaper reached a bandwidth as narrow as $5\,$cm^{-1}, which is an increase in resolution by a factor of 3 compared to the previous configuration using an etalon (Section 2.1.1). The bandwidth used for the experiments of Chapter 3 was $15\,$cm^{-1} in favor of a higher VIS energy ($\sim 40\,\mu$J).

2.2 Twin-Plate Ice Nucleation Assay

Freezing spectra of the investigated ice-nucleating samples constitute, next to SFG, the backbone of the here presented studies, as they provide the only direct quantitative insight in the functionality of the contained INs. The twin-plate ice nucleation assay (TINA) is a well-suited tool for the investigation of highly efficient INs, as it offers fully automated high-throughput droplet freezing experiments, which allow the variation of sample parameters at high-statistics. The experiment is conducted under immersion-freezing conditions, where the INs are immersed in μl-droplets. Additional details to the descriptions in this Section can be found in Kunert *et al.*[45]
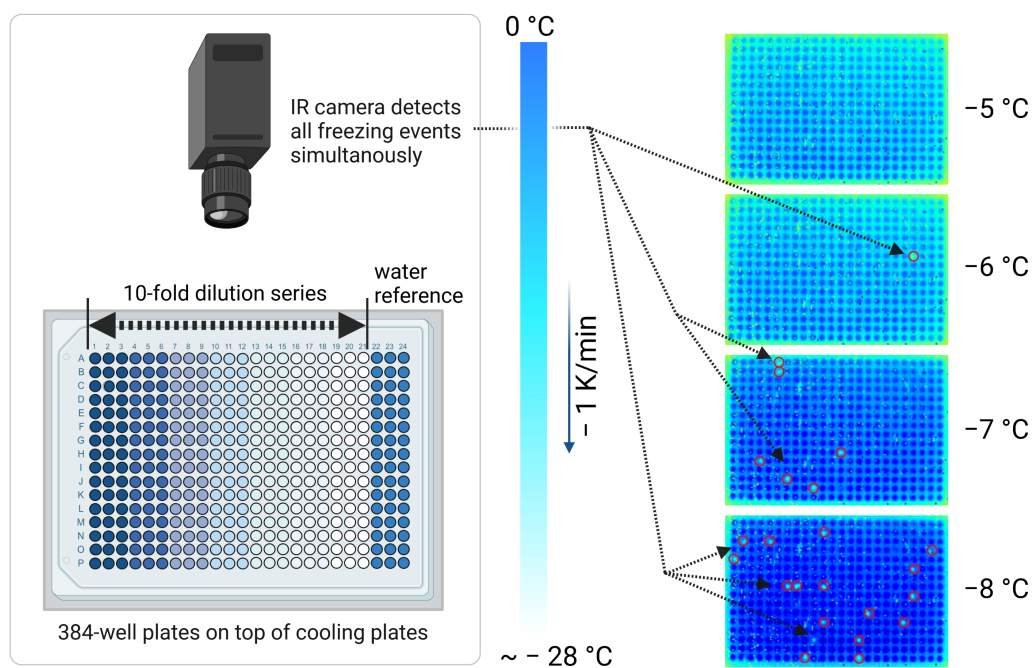
Figure 2.8: Schematic of the TINA droplet freezing assay - In the Twin-plate Ice Nucleation Assay (TINA) a 10-fold dilution series of the sample and a reference of ultra-pure water are deposited in two 384-well plates. In this illustration, only one well plate is shown, with only 48 instead of 96 droplets per dilution. The well-plates are stacked onto a cooling block and cooled at a $-1\,\mathrm{K/min}$ rate. An IR camera detects the latent heat release upon droplet freezing. The infrared camera images in the right part of the figure have been adapted from Kunert *et al.*[45,128] Red rings indicate freezing droplets.

An illustration of TINA's working principle is depicted in Figure 2.8. In a typical experiment, a prepared sample, an IN in an aqueous solution/suspension, is diluted in a 10-fold series and partitioned (96 droplets of $3\,\mu\mathrm{L}$ per dilution) into two 384-well plates,

together with a reference of pure, autoclaved water using a liquid handling station (epMotion ep5073, Eppendorf, Hamburg, Germany). The well plates are stacked onto an aluminum block, which is cooled down to temperatures $\sim -28\,°\mathrm{C}$ at a continuous cooling rate of $-1\,\mathrm{K/min}$, with a temperature uncertainty of $\pm\,0.2\,°\mathrm{C}$. Two IR cameras (Therman Compact XR, Seek Thermal Inc., Santa Barbara, CA, USA) detect the latent heat releases from all freezing droplets at a given temperature simultaneously.
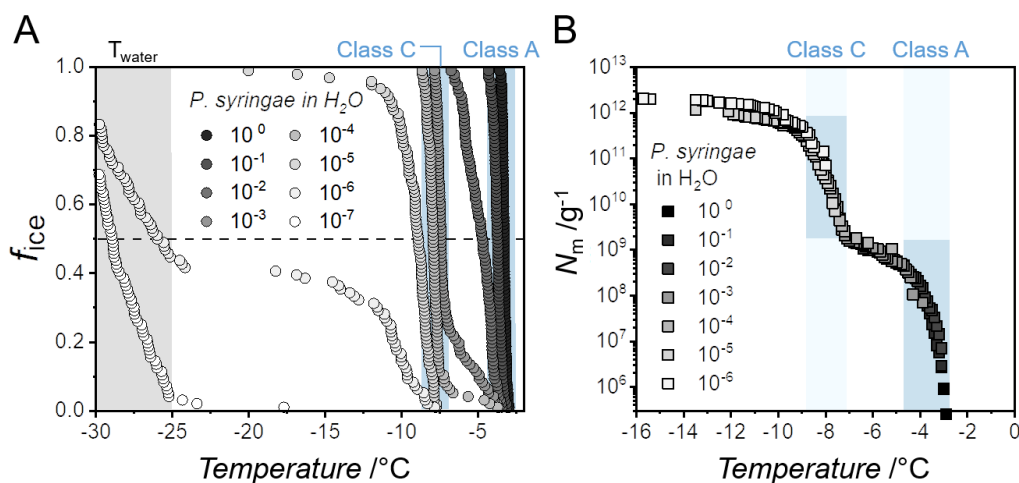
Figure 2.9: Freezing curves and spectra of *P. syringae* in aqueous solution - (A) Fraction of frozen droplets $f_{ice}(T)$ for the different dilutions of the stock solution. Crossings with the dashed line indicate the temperatures at which 50% of the droplets are frozen (T_{50}). (B) Cumulative freezing spectra $N_m(T)$ calculated from the dilution series using Vali's equations.[129] The steep rises observed in this spectrum are attributed to the IN Classes A and C, respectively. The highest dilution in (A) exhibits an activity that is comparable to pure water and is hence neglected in (B). Adapted from Lukas *et al.*[5]

A straightforward evaluation of the obtained data is an overview of the **fraction of frozen droplets (f_{ice})** vs. temperature (Figure 2.9 A). Here, each of the dilutions contributes a separate curve. From this plot, the different threshold/onset freezing temperatures of the single dilutions can be obtained, as well as the T_{50} values, which are the temperatures at which 50% of droplets are frozen, respectively. Background freezing of pure (autoclaved Milli-Q®) water in our system occurred at around $-25\,°\mathrm{C}$ and was presumably caused by remaining impurities and the supporting surface of the utilized well plates.[45,130] The homogeneous freezing temperature for μl-sized droplets at the applied cooling rate predicted by CNT is $\sim -33\,°\mathrm{C}$.[8,15,45] In the case of highly efficient INs from *P. syringae* the background freezing did not affect the experiment, as all

droplets containing INs were frozen at around $-20\,°\text{C}$. This can be seen in Figure 2.9 A, were around 40% of the 10^{-6}-dilution droplets are frozen at $-20\,°\text{C}$, while freezing of the residual droplets occurs in the range of T_{water}. The 10^{-7} dilution doesn't show significant ice nucleation activity anymore.

While the T_{50} values are useful for a comparable parameterization of the freezing experiments, the key feature of the TINA experiment is the possibility to derive so-called **freezing spectra**. These spectra show the cumulative number concentrations of the INs present in the sample, active above a certain temperature. The equations for their calculation were developed by Vali (1971).[129] In short, Vali's equations provide a solution for the problem that the freezing of an individual droplet is a cascade that can be triggered by a single IN; therefore the number of INs in the droplet, active at that temperature, is not directly measurable.

The cumulative number of INs active at a certain temperature $\Delta N_m(T)/\Delta T$ and the cumulative IN number concentration $N_m(T)$ can be calculated by[45]

$$\frac{\Delta N_m}{\Delta T}(T) = -ln\left(1 - \frac{s}{a - \sum_{i=0}^{j} s}\right) \cdot \frac{c}{\Delta T}; \quad 0 \leq j \leq a \tag{2.6}$$

$$N_m(T) = -ln\left(1 - \frac{\sum_{i=0}^{j} s}{a}\right) \cdot c. \tag{2.7}$$

Here, s is the number of freezing events in ΔT, a is the total number of droplets and m is the sample mass (e.g., Snomax®, purified INP) in the initial solution. The factor c is given by

$$c = \frac{V_{ini}}{V_{drop}} \cdot \frac{d}{m}, \tag{2.8}$$

with the volume of the initial solution V_{ini}, the droplet volume V_{drop}, and the respective dilution factor d.

Experimentally, the application of a dilution series ensures the acquisition of all activation temperatures of INs present in samples of *P. syringae* INPs, where the least efficient INs are at the same time the most frequent and hence are observed at the highest dilution.

In this work, the cumulated IN number concentration $N_m(T)$ is referred to as the *freezing spectrum* of a sample. As introduced in Section 1.2, different types of INs can

be identified from distinct activation temperatures observable in the spectrum of the bacterium *P. syringae*. These *Classes* A and C constitute the basis for the discussions in the following chapters.

2.3   Circular Dichroism Spectroscopy

Circular dichroism (CD) spectroscopy was used as a method for the determination of secondary structures of the investigated INPs. It is based on the difference absorption spectra obtained for left- and right-handed circularly polarized light passing the sample solution (Figure 2.10 A). The so-called ellipticity provides information on the structure as it depends on the chirality of the sample in solution. The information about the secondary structure of a protein is contained in the far-ultraviolet range between ~ 190 nm to 240 nm.[131] It refers to the electronic transition $n \rightarrow \pi^*$ at 222 nm, and $\pi \rightarrow \pi^*$ transitions at 190 nm and 208 nm. The CD-spectra of the most common structures are shown in Figure 2.10 B. α-helix, β-barrel and random coil can constitute the predominant fraction of a protein; more complicated structures are obtainable from structural databases.[135]

The magnitudes and positions of the peaks in a CD-spectrum can shift depending on the environment. For instance, the peak positions in the spectra of membrane proteins can be shifted several nanometers against structurally similar soluble proteins. The shift direction again can be opposite for the distinct peaks. The reason has been attributed to the membrane proteins being embedded in hydrophobic structures formed by the membrane fragments, while soluble proteins are isotropically dissolved.[131]
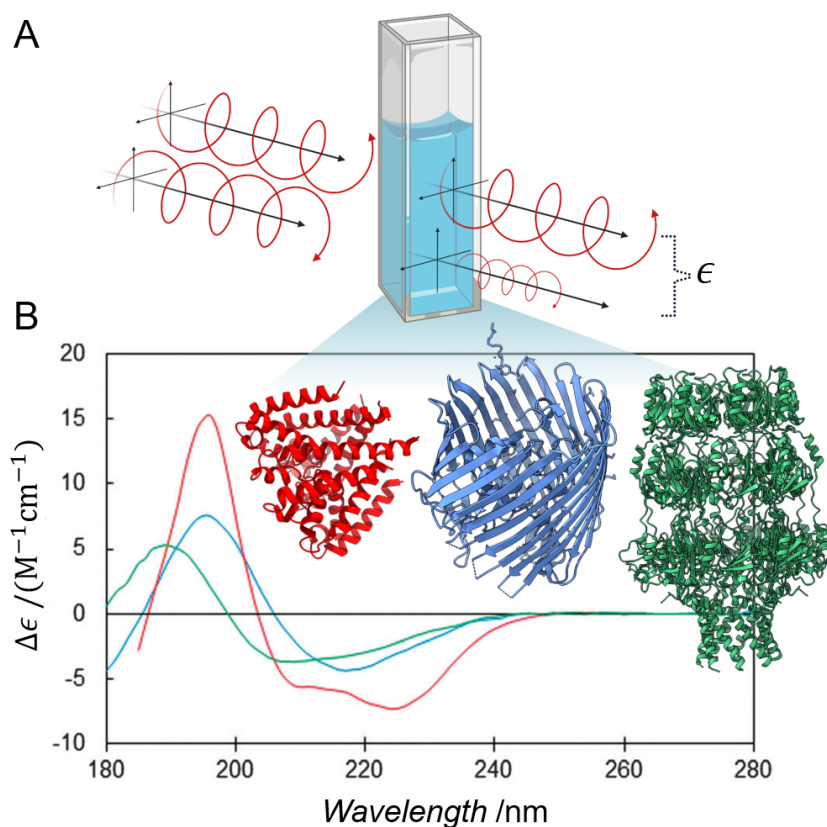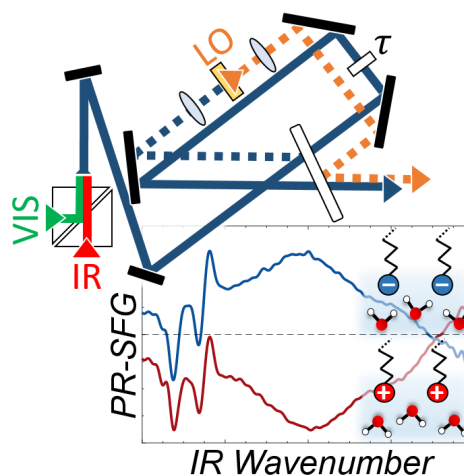
Figure 2.10: Circular Dichroism spectroscopy and spectra of standard secondary protein structures - (A) Principle of CD spectroscopy. The ellipticity is determined from the difference absorption spectra of left- and right-handed circularly polarized light. (B; *adapted from Miles 2016* [131,132]): $\Delta\epsilon$ is the ellipticity difference between the sample and a reference measurement of the pure solvent. α-helix, β-sheet and random coil are typical structures found for membrane proteins. Red: a sodium channel pore, predominantly α-helical;[133] blue: BTUB, an outer membrane cobalamin transporter, predominantly β-sheets (forming a β-barrel);[134] green: WZA translocon for capsular polysaccharides, mixed helical, β-sheet and unordered structure.[134] The shown crystal structures correspond to the PCDDB[135] IDs 4F4L, 1NQE, and 2J58, respectively).

3

Passively Stabilized Phase-Resolved Collinear SFG Spectroscopy using a Displaced Sagnac Interferometer

3. PASSIVELY STABILIZED PHASE-RESOLVED COLLINEAR SFG SPECTROSCOPY USING A DISPLACED SAGNAC INTERFEROMETER

3.1 Abstract

Sum-frequency generation (SFG) vibrational spectroscopy is a powerful technique to study interfaces at the molecular level. Phase-resolved SFG (PR-SFG) spectroscopy provides direct information on interfacial molecules' orientation. However, its implementation is technologically demanding: It requires the generation of a local oscillator wave and control of its time delay with sub-fs accuracy. Commonly used noncollinear PR-SFG provides this control naturally but requires very accurate sample height control. Collinear PR-SFG spectroscopy is less demanding regarding sample positioning, but tuning the local oscillator time delay with this beam geometry is challenging. Here, we develop a collinear PR-SFG setup using a displaced Sagnac interferometer. This scheme allows full, independent control of the time delay and intensity of the local oscillator and provides long-time phase stabilization (better than 5° over 12 hours) for the measured signal. This approach substantially reduces the complexity of an experimental setup and combines the advantages of collinear and noncollinear PR-SFG techniques.

3.2 Introduction

Sum-frequency generation (SFG) vibrational spectroscopy probes molecular vibrational modes and provides information on the microscopic structure and dynamics at interfaces.[136,137,138,139] The value of this method has repeatedly been proven in studies of a variety of interfaces: aqueous mineral surfaces,[31,140] the water/air interface,[123,141,142] surfactants,[97,98,99] and surface-active peptides and proteins.[2,143,144,145,146] The impact of SFG spectroscopy can be substantially increased by obtaining complex-valued spectra, performing phase-resolved measurements.[90,93,121,123,124] The most prominent advantage is the direct acquisition of information on the orientation of the interfacial molecules. However, the implementation of PR-SFG spectroscopy is complicated by the required phase stability and, thus, the high stability of optical pathways. The latter makes this spectroscopy technically demanding and hence hinders its widespread use. Here, we present a collinear phase-resolved SFG setup with passive phase stabilization using a displaced Sagnac (DS) interferometer. Collinear beam geometry and passive phase stabilization significantly simplify the experimental layout, provide long-term phase stability, and reduce the required mechanical constraints on the measured interface.

46

SFG spectroscopy probes the second-order nonlinear susceptibility $\chi^{(2)}$ of a sample. The real part of the complex-valued $\chi^{(2)}$ spectrum reflects optical dispersion of a material, and its imaginary part provides frequencies and line shapes of vibrational resonances (similar to absorption spectra). The $\chi^{(2)}$ spectrum is measured by mixing a mid-infrared (IR) and an upconverting visible (VIS) beam at the sample surface and detecting a signal field emitted at their sum-frequency. In conventional SFG spectroscopy, one measures signal intensity by using a square-law detector (e.g., a CCD camera or photomultiplier tube). This method, usually called homodyne detection, lacks information about the phase of the complex-valued $\chi^{(2)}$ and superposes its real and imaginary parts. In phase-resolved SFG (also called heterodyne detection), one measures the signal's electric field via its interference with an auxiliary electromagnetic wave called local oscillator (LO).[93,121,122,123,124,125,126] To resolve the phase and derive real and imaginary parts of the $\chi^{(2)}$ response, this method requires a time delay τ between the SFG signal and LO pulses. The phase modulation induced by the time delay results in interference fringes in the measured intensity spectrum $I_{SFG}(\omega)$, the spectral interferogram (3.1):

$$
\begin{aligned}
I_{SFG}(\omega) = |E_{SFG}(\omega)|^2 = \\
= |E_{sa}(\omega)|^2 + |E_{LO}(\omega)|^2 + E_{sa}(\omega)E_{LO}^*(\omega)e^{i\omega\tau} + E_{sa}^*(\omega)E_{LO}(\omega)e^{-i\omega\tau}
\end{aligned}
\tag{3.1}
$$

Here, $E_{sa}(\omega)$ and $E_{LO}(\omega)$ are the complex-valued spectra of the signal and local oscillator fields, respectively. The LO is usually generated by sum-frequency mixing of the IR and VIS fields in a nonlinear medium (nonlinear crystal or surface of gold, GaAs, etc.). The complex-valued $\chi^{(2)}$ spectrum is contained in E_{sa} and is deduced from one of the cross terms in Equation (3.1). Details are described in Section 2.1.3. This cross term varies periodically with the detection frequency ω, with a period determined by the time delay τ between the signal and the LO, giving rise to fringes in the spectrum $I_{SFG}(\omega)$. For example, fringes with a period of less than $10\,\mathrm{cm}^{-1}$ require a $\tau > 3.3\,\mathrm{ps}$. From these fringes, we determine the phase of the signal relative to that of the LO. Because the signal and LO are in the visible wavelength range (typically 610–740 nm), the time delay τ needs sub-femtosecond ($\Delta\tau \lesssim 0.05\,\mathrm{fs}$) stability for acquiring a stable interferogram. This implies a stability of the optical pathways of several nanometers. At present, most common implementations of PR-SFG setups use a geometry where the IR and VIS beams are noncollinear. With this geometry, the LO propagates separately

3. PASSIVELY STABILIZED PHASE-RESOLVED COLLINEAR SFG SPECTROSCOPY USING A DISPLACED SAGNAC INTERFEROMETER

from IR and VIS beams after it is generated, and τ is produced by increasing the optical pathway of the LO using a transparent refractive medium (e.g., glass window). The utilization of transmission optics for generating τ and shared reflecting optics for the IR, VIS, and LO beams provides the required high phase stability of the setup.[126]

A noncollinear beam geometry makes the generation of the time delay between the signal and LO straightforward; however, this design is inherently susceptible to a displacement of the sample surface position. For instance, measurements of evaporating samples require frequent or continuous height corrections and therefore either multiple data acquisitions or a feedback loop to account for evaporation.

A collinear geometry of IR, VIS and LO beams overcomes these limitations for PR-SFG.[147,148] In this configuration, the measured phase of the signal is largely invariant to displacements of the sample surface. Implementation of this geometry is, however, in practice hindered by the spatial overlap of the IR, VIS, and LO pathways which complicates control of τ. Xu *et al.* utilized materials with suitable group velocity mismatch (GVM) between LO (~ 630 to $710\,\mathrm{nm}$) and IR ($\geq 3000\,\mathrm{nm}$) pulses to produce a delay of $\sim 2\,\mathrm{ps}$.[149] Because the beams travel via the same reflecting optical elements, the phase stability in this approach is inherently high. However, it requires materials with appropriate transmission and dispersion in the broad range of infrared and visible frequencies.

An alternative approach was elaborated by Thämer *et al.*, employing a Mach-Zehnder type interferometer to separate the pathways of the LO pulse and the IR/VIS pulse pair.[147] Different pathways allow independent control of the time delay, intensity, and polarization of the LO, but require active phase stabilization or continuous sampling of a reference simultaneously with the signal acquisition. Although impressive phase stability and accuracy can be achieved, active phase control considerably complicates the experimental setup.[150]

In the present work, we develop a collinear PR-SFG spectroscopy setup based on a displaced Sagnac (DS) interferometer. The DS interferometer provides passive phase stabilization, which substantially reduces the complexity and cost of the setup. This approach combines the advantages of collinear SFG with the convenience of the passive phase stabilization of many noncollinear SFG implementations.

3.3 Experimental Setup

Our setup is illustrated in Figure 3.1: We utilize broadband mid-IR pulses (IR, FWHM $\sim 450\,\mathrm{cm}^{-1}$) and narrowband near-IR/visible pulses (VIS, FWHM $\sim 15\,\mathrm{cm}^{-1}$) generated from the output of an amplified Ti:sapphire femtosecond laser (see Supporting Information (SI; Section 3.6) for details). The VIS and IR beams are combined using a homemade double CaF_2 prism beam combiner (*PBC*; Figure 3.5 in the SI) and aligned to the DS interferometer (Figure 3.1 B).

At the input of the interferometer, the collinear beams are split into two portions by a 1° wedged CaF_2 window (*beam splitter and combiner, BSC*). The minor, reflected fraction (dashed line) propagates clockwise and is used to generate the LO signal (SFG_{LO}) by focusing it on a $10\,\mu$m thin BBO crystal (*BBO*) with a CaF_2 lens (*L1*, 0.5" diameter, 50 mm focal length). To control the intensity of SFG_{LO}, we move the crystal relative to the focus of *L1* using a linear translation stage.

SFG_{LO} is collimated by a second, similar lens (*L2*) and is combined at the *BSC* with the larger fractions of the IR and VIS beams that propagate counterclockwise. A 4 mm thick CaF_2 window (*PhM*) is installed in the counterclockwise path to partially compensate for the time delay produced by *L1*, *L2*, and *BBO* in the clockwise path, and to adjust the time delay τ. Overall, the throughput of VIS and IR energies through the interferometer is $\sim 75\%$.

After the DS interferometer, IR, VIS, and SFG_{LO} are directed to the sample module (Figure 3.1 C), where they are focused on the sample surface by a 100 mm focal length off-axis parabolic mirror (*PM*). We installed a telescope in the VIS pathway (*Tel*, Figure 3.1 A) to control the VIS focus. The generated signal SFG_{sa} and the fraction of SFG_{LO} reflected from the sample are collimated by a plano-convex lens (*L3*, focal length 100 mm) and directed to the spectrometer (Acton SP 300i, Princeton Instruments) equipped with a CCD camera (Newton 970, Andor Technologies). We use a 750 nm shortpass filter (*SP*, FES0750, Thorlabs Inc.) in front of the spectrometer to block reflected and scattered VIS light.

We use the alignment laser *AL* and the auxiliary alignment path *AP* to align the setup, as detailed in the SI (Section 3.6).

An intrinsic issue of the collinear beam geometry can be the generation of background ("ghost") SFG signals because of the spatial and temporal overlap of IR and VIS at

3. PASSIVELY STABILIZED PHASE-RESOLVED COLLINEAR SFG SPECTROSCOPY USING A DISPLACED SAGNAC INTERFEROMETER
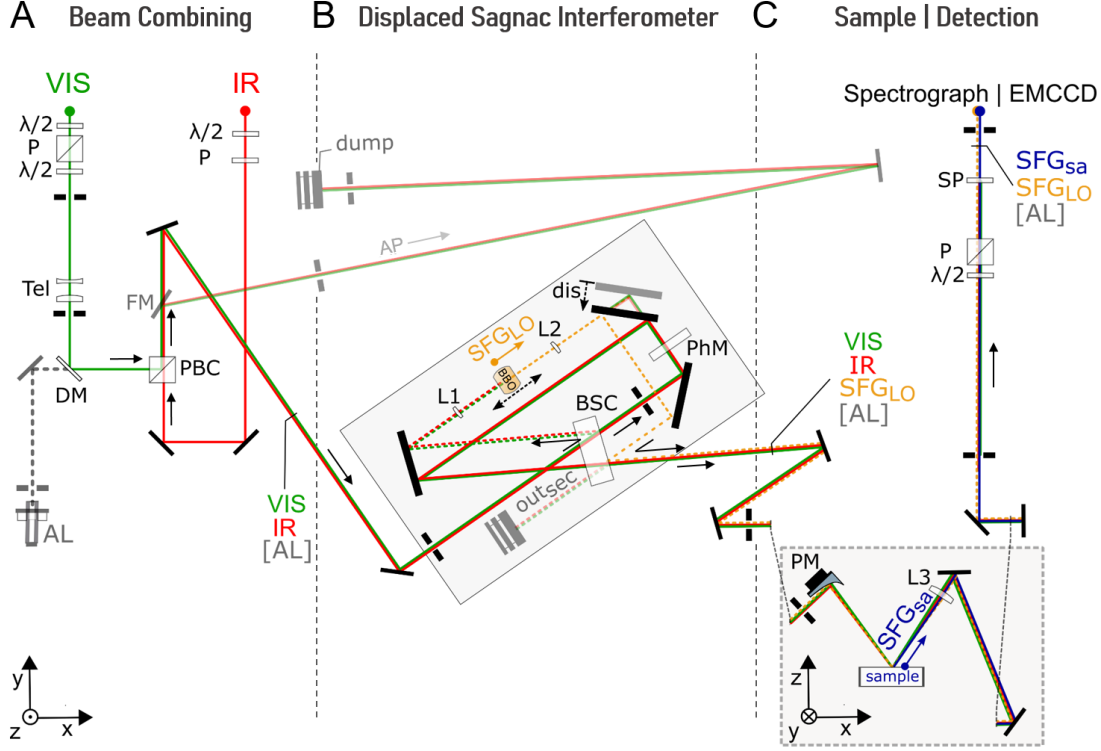

Figure 3.1: Scheme of the collinear PR-SFG spectroscopy setup using a DS interferometer - (A) Prism beam combiner module (*PBC*); (B) DS interferometer module with local oscillator (LO) generation (BBO crystal) and phase modulator (*PhM*); (C) sample and detection module. The alignment laser (*AL*), auxiliary alignment path (*AP*) and flip mirror (*FM*) are used for alignment of the setup.

several optical elements. Such signals can heavily perturb the phase-resolved as well as the conventional SFG spectra. To avoid the generation of ghost signal, we do not use a coated dichroic dielectric mirror to combine the IR and VIS beams before the DS interferometer. Instead, we employ a homemade beam combiner (*PBC*) composed of two CaF_2 right-angle prisms (PS703, Thorlabs Inc., Figure 3.5 in the SI). The prisms are mounted to form a cube, and the air gap between them determines the frustrated total internal reflection of VIS and IR, respectively. Because of the large wavelength difference of these beams, by adjusting the compressive force applied on the prisms (surface flatness $\sim 300\,\mathrm{nm}$) we can achieve simultaneous IR ($3000\,\mathrm{nm}$) transmission and VIS ($800\,\mathrm{nm}$) reflection of $\sim 85\%$ and $\sim 70\%$, respectively. The *PBC* is hence responsible for the majority of the losses. The uncoated CaF_2 of the *PBC* does not generate a detectable SFG response (see also the discussion in the SI).

3.4   Results & Discussion

One of the most important characteristics of a PR-SFG setup is the drift of phase of a measured signal over time. The phase drift can be caused by instability of the DS interferometer and/or instability of other optical equipment (laser, optical parametric amplifier, beam pathways, etc.). To characterize the phase stability of the interferometer, we use the beam from a continuous wave helium-neon (HeNe) laser (SL 02/1, SIOS Messtechnik), which we align into the interferometer. We measure the interference pattern of the HeNe beam at the second output of the interferometer (out_{sec} in Figure 3.1) with a CMOS camera (Zelux 1.6 MP, Thorlabs Inc.). The typical profile of the interference fringes (light intensity over pixels extracted from the images) is shown in Figure 3.2 A for a 180 min measurement period. Figures 3.2 B,C show the phase and intensity drifts of this interference (details of the data processing are provided in the SI, Section 3.6). Thus, the phase stability of the DS interferometer in the course of 3 hrs is better than 5°.

To examine the stability of the whole setup, we acquire PR-SFG spectra of z-cut quartz in intervals of 10 s and 20 min for periods of 20 min and 12 hrs, respectively. The Figures 3.2 D–I show typical spectral interferograms, and phase and intensity drift, respectively. For both, short and long periods, the phase drift is within 5°. Such stability is sufficient for most PR-SFG measurements, and phase accuracy of measured vibrational spectra can be further improved by regularly measuring signal from the reference material or by active beam pointing stabilization.

An essential advantage of the collinear beam configuration in a PR-SFG setup is the low sensitivity of the phase of a measured spectrum to changes in the sample height positioning. To test this for the practically relevant case of evaporating samples, we measure spectra of the H_2O/air interface using an open sample without any adjustment of the sample position. Data acquisition with 2 min accumulation time is performed for 150 min (Figure 3.2 J–L). The estimated evaporation rate of $\sim 5\,\mu$m/min relates to a total height change of $750\,\mu$m. The phase is stable within 5° for the first 20 minutes, followed by a gradual drift of $\sim 10°$ over the next 40 minutes. After 90 minutes, the intensity of the signal declines due to the macroscopic sample surface displacement. This is accompanied by the increasing instability of the signal phase. In contrast, phase drift

3. PASSIVELY STABILIZED PHASE-RESOLVED COLLINEAR SFG SPECTROSCOPY USING A DISPLACED SAGNAC INTERFEROMETER
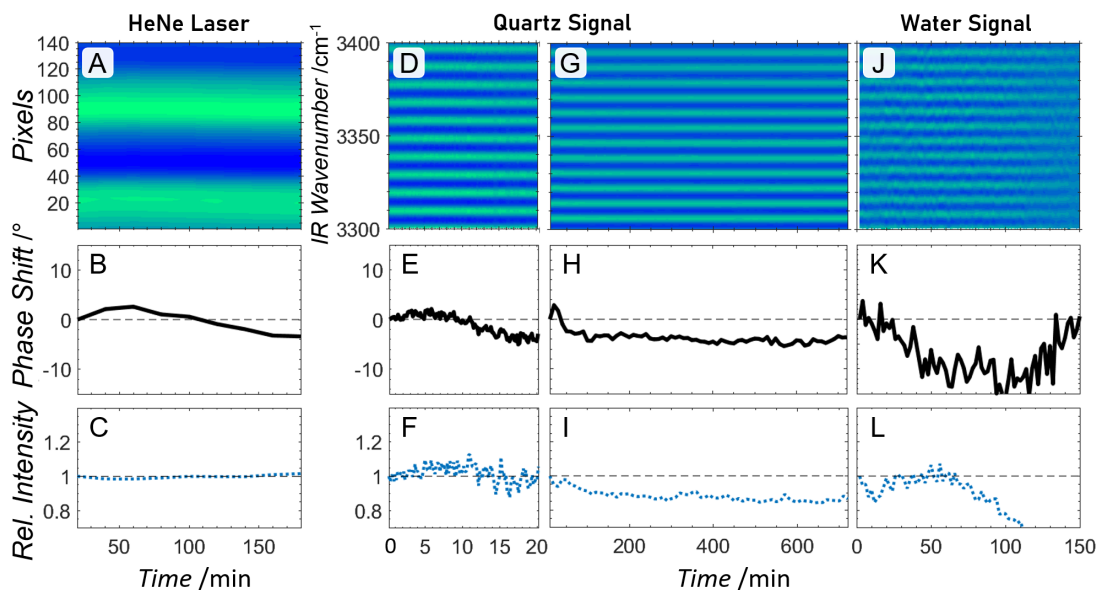

Figure 3.2: Phase stability examination of the collinear PR-SFG setup with DS interferometer - (A–C) DS interferometer stability test using a stabilized HeNe laser: Interference pattern, its phase and intensity, respectively. (D–I) Setup stability test for 20 min and 12 hrs periods using a model z-cut quartz sample: Interference pattern at the detector between the SFG_{sa} and SFG_{LO} (D,G), its phase (E,H) and intensity (F,I). (J–L) Stability test for evaporating H_2O sample (interference pattern, its phase and intensity). Intensity and phase are shown relative to the first measurements of the respective experiments.

of up to 30° in 5 minutes has been reported under comparable experimental conditions using noncollinear beam configurations.[151]

To verify the performance of our setup for spectroscopy of molecular samples, we use four different benchmark interfaces: the neat H_2O/air and D_2O/air interfaces, and monolayers of 1,2 dipalmitoyl-3-trimethylammonium-propane (DPTAP) and 1,2 Dipalmitoyl-sn-glycero-3-phosphoglycerol (DPPG) lipids deposited onto the H_2O surface. All spectra are acquired by the accumulation of the S-polarized signal field for 20 minutes, and using P-polarized IR and S-polarized VIS fields for sample excitation. In these measurements, we use z-cut quartz as reference material to normalize the signal to the spectral intensity of the IR beam and to deduce the phase of the molecular $\chi^{(2)}$ response.[126]

Figure 3.3 A shows the imaginary parts of the complex-valued $\chi^{(2)}$ spectra of the four interfaces. The spectrum of the H_2O/air interface (black trace) consists of a broad negative band in the frequency range ~ 3100–$3600\,\mathrm{cm}^{-1}$, which is generated by the

52

hydrogen-bonded water molecules with a predominant orientation of hydrogens away from the interface, into the bulk.[97,152]

The spectra of DPTAP (red trace) and DPPG (blue trace) lipids contain several vibration bands. The narrow peaks in the ~ 2800–$3000\,\mathrm{cm}^{-1}$ frequency range are assigned to C–H stretch vibrations of the lipids.[93] The negative peaks at $2875\,\mathrm{cm}^{-1}$ and $2937\,\mathrm{cm}^{-1}$ are the Fermi doublet of the symmetric CH_3 stretch mode. The positive peak at $2963\,\mathrm{cm}^{-1}$ has been attributed to the asymmetric CH_3 stretch vibration. The C–H stretch bands of DPPG and DPTAP are similar, indicating the similarity of orientation (towards air) of the lipid tails.[93] The two broad bands around 3200 and $3400\,\mathrm{cm}^{-1}$ are produced by the water O–H stretch vibrations. These peaks have an opposite sign for the two lipids, corresponding to hydrogen atoms oriented away from and towards the water bulk for DPPG and DPTAP, respectively. Therefore, this signal can be attributed to water molecules below the charged lipids' head groups, with their orientation dependent on the respective net charge at the interface (see insets). An additional band with opposite sign at $\sim 3600\,\mathrm{cm}^{-1}$ has previously been attributed to water molecules above the lipids' head groups, oriented opposite to the water below the headgroup.[97]

All measured molecular PR-SFG spectra are in good agreement with previously published data. For an additional test of our setup, we use SFG spectra of the same four interfaces measured with conventional homodyne detection. To this end, we block the LO pathway in the DS interferometer. In Figure 3.3 B we compare the $\left|\chi^{(2)}\right|^{2}$ spectra obtained from the homodyne measurements (solid lines) with those calculated from the phase-resolved data. The two types of SFG measurements are in excellent agreement, which provides a self-consistency check of our apparatus.
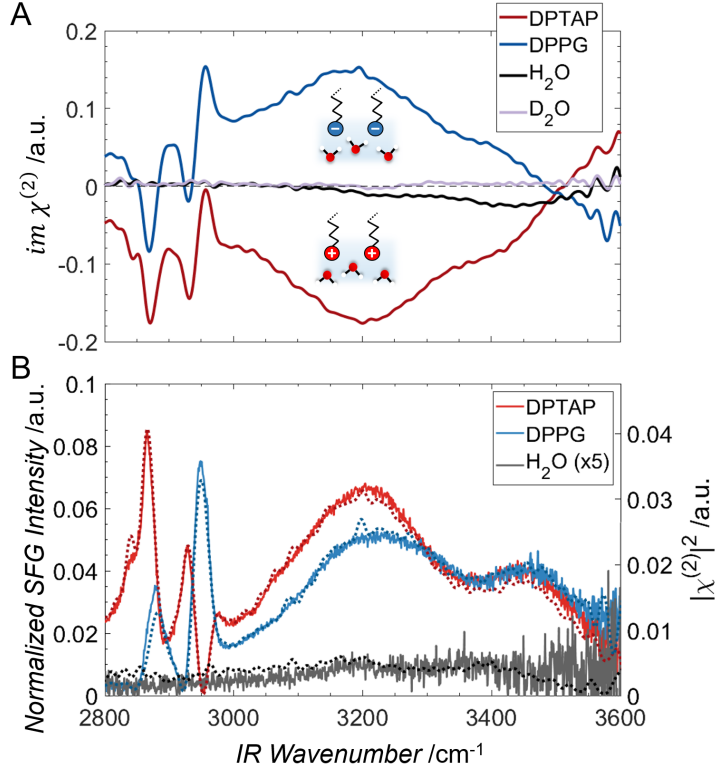
Figure 3.3: SFG spectra of the DPTAP/H₂O (red), DPPG/H₂O (blue), and neat H₂O/air (black) interfaces - (A) Imaginary parts of the $\chi^{(2)}$ spectra. The non-resonant signal from the D_2O/air interface (purple) is used as a reference for the absolute phase. The insets illustrate the alignment of water molecules due to the lipids' charged head groups. (B) $\left|\chi^{(2)}\right|^2$ spectra obtained from conventional (homodyne) SFG spectroscopy measurements (solid lines) and from the data shown in panel A (dashed lines). The H_2O spectra are scaled by a factor of 5. We note that the spectra are not corrected for Fresnel factors' contributions.

3.5 Conclusions

In conclusion, collinear PR-SFG spectroscopy using a displaced Sagnac interferometer features reduced cost and complexity, and provides a convenient way to study the physical properties of surfaces and interfaces. It provides passive phase stabilization together with full independent control of time delay, intensity, and polarization of the local oscillator, and can be readily used over the entire range of mid-IR frequencies.

3.6   Supporting Information

- Details on sample preparation and experimental methods

- Scheme of 4f pulse shaper in reflection configuration

- Schematic illustration of the double CaF_2 prism beam combiner

- Alignment procedure of the DS interferometer

- Interferograms and inferred $im\left[\chi^{(2)}\right]$ spectra of the H_2O measurement

- PR-SFG spectra of H_2O, utilizing a PTB7 anti-ghost filter

Characteristics of the Experimental Setup

In our setup, seed pulses with a spectral bandwidth of $\sim 60\,nm$ are generated in a Ti:sapphire laser oscillator (Mai Tai, Spectra-Physics). These pulses are amplified in a regenerative amplifier (Spitfire Ace, Spectra-Physics) which is pumped by a Nd:YLF (neodymium-doped yttrium lithium fluoride) laser (Empower, Spectra-Physics). The output ($\sim 5\,mJ$/pulse, centered at around $800\,nm$ and with a duration of $\sim 40\,fs$, $1\,kHz$ repetition rate) is divided by a beam splitter. $1.7\,mJ$/pulse are utilized to pump a commercial optical parametric amplifier (TOPAS-C, Spectra-Physics) equipped with a difference-frequency generation (DFG) unit (with a $AgGaS_2$ crystal) to generate mid-infrared (IR) pulses. The IR output of the TOPAS has an energy of $\sim 5\,J$/pulse, and is centered at around $3300\,cm^{-1}$ with a FWHM of $\sim 450\,cm^{-1}$. The remaining fraction of the Ti:sapphire laser output ($\sim 3.3\,mJ$/pulse) is used to produce a narrowband (VIS) pulse using a homemade 4f pulse shaper in reflection configuration (Figure 3.4 and Section 2.1.4).
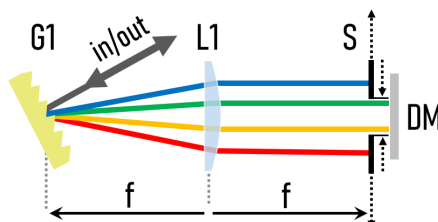

Figure 3.4: Scheme of the 4f pulse shaper in reflection configuration - Grating (G) ($1500\,$groves/mm, AOI 53°), cylindrical plano-convex lens (L) ($f = 20\,cm$), tunable slit (S), dielectric mirror (M).

3. PASSIVELY STABILIZED PHASE-RESOLVED COLLINEAR SFG SPECTROSCOPY USING A DISPLACED SAGNAC INTERFEROMETER

The VIS pulses had an energy of $\sim 30\,\mu$J and a spectral bandwidth of $\sim 15\,\text{cm}^{-1}$ (full width at half-maximum, FWHM). The incident angle of the collinear beams (VIS, IR and SFG_{LO}) on the sample was 36° with respect to the surface normal. At a sample, the IR and VIS beams had an energy of $\sim 2\,\mu$J/pulse and $\sim 13\,\mu$J/pulse, respectively.

The spectra presented in this study were simultaneously recorded in the C–H and O–H stretch regions. The generated SFG signal and fraction of the SFG_{LO} reflected from the sample surface were collimated by a 10 cm focal length plano convex lens, directed to a spectrograph (Acton SP 300i, Princeton Instruments) and detected by an EMCCD camera (Newton 970, Andor Instruments). Half-wave plate and polarizer pairs were used to set the polarizations of VIS, IR, and the detected components of SFG_{sa} and SFG_{LO}. All spectra were obtained in the SSP polarization combination (S-polarized SFG signal, S-polarized VIS, P-polarized IR). Background spectra are recorded with VIS beam only (IR beam being blocked). Measured sample spectra were normalized using reference spectra from z-cut quartz.

The SFG measurements of liquid samples were performed in a custom-made PTFE trough with a diameter of ~ 8 cm and a volume of ~ 20 ml, filled with pure water. Both lipids were drop-casted on the surface in chloroform solution, using a $0.5\,\mu$L click syringe to establish a near monolayer coverage. The coverage was estimated to be complete when the casted droplets did not spread.
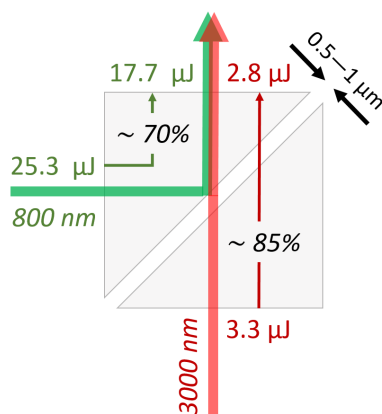

Figure 3.5: Schematic illustration of the double CaF$_2$ prism beam combiner (PBC) with typical reflectivity and transmittance values for VIS and IR, respectively - The surface roughness and the force applied to the prisms determine the gap and hence the frustrated total internal reflection of both beams.

Alignment of the Setup

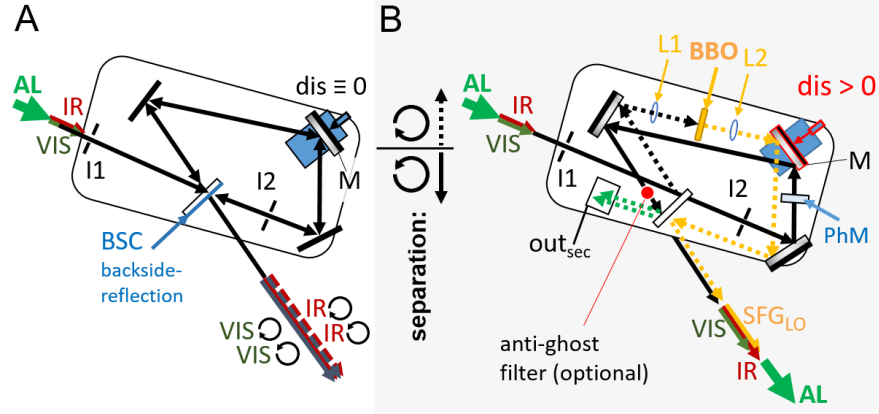### 1. Initial alignment of the DS interferometer

Figure 3.6: Alignment of the DS interferometer - (A) shows the interferometer before, (B) after introduction of the displacement (*dis*) and the additional elements *L1*, *L2*, *BBO*, and *PhM*.

Initially, the interferometer is aligned in its not-displaced configuration using the alignment laser *AL* (Figure 3.6 A). To this end, the AL beam is aligned through the irises *I1* and *I2*. Two fractions of the AL beam, propagating clockwise and counterclockwise, are aligned collinear inside the interferometer by adjusting the *BSC* and mirrors of the interferometer. Collinearity of the beams is monitored by their overlap on a paper card. When the not-displaced interferometer is aligned, we displace it by moving mirror *M* using a manual linear translation stage (Figure 3.6 B). The displacement (*dis*) produces separation of about 3 cm of the counter-clockwise and clockwise pathways. Collinearity of the two paths is then improved in the displaced configuration by adjusting two of the interferometer mirrors and monitoring interference pattern on a paper card at the secondary output (*out$_{sec}$*) of the interferometer. For collinear clockwise and counterclockwise pathways, the interference is uniform across the beam profile. After the displaced configuration is aligned, we install the lenses *L1*, *L2* and a nonlinear crystal (BBO, barium borate) into the clockwise pathway, and the phase modulator (*PhM*) into the counterclockwise pathway. Collinearity of the clockwise and counterclockwise pathways is optimized again, tuning the radial positions of *L1* and *L2*, to achieve uniform interference at *out$_{sec}$*.

2. Daily alignment of the DS interferometer

The daily alignment of the interferometer is performed after all optics (*L1*, *L2*, *BBO* and *PhM*) have been installed into the DS interferometer. *L2* can be used to optimize the interference pattern of the AL beam at the out_{sec} as described above. The final optimization of the interference is performed by tuning the radial position of *L2* and observing the interferogram of SFG_{sa} and SFG_{LO} (for non-resonant reference material (z-cut quartz) at the sample position; Figure 3.7 B).

3. Alignment of the IR and VIS beams

VIS and IR beams, as well as the alignment laser AL, are combined at the prism beam combiner (*PBC*, Figures 3.1 A and 3.5) and subsequently propagate collinearly. To this end, we use a flip mirror (*FM*) to send the beams into an auxiliary alignment path (*AP*) with two irises (distance ~ 1.5 m). The collinear beams are then directed into the DS interferometer, using a second pair of irises (*I1* and *I2* in Figure 3.6).

4. Additional remarks on the setup alignment

Height position and surface tilt of a sample and reference material can be adjusted with sufficient reproducibility using an alignment laser and two irises. We calibrate this alignment path, using an alignment beam reflected from a flat water surface in the height of the IR focus, which is aligned through the two irises using a set of mirrors. When adjusting height and tilt of a sample or reference, it is sufficient to recover the alignment of the alignment beam through these two irises.

Data Processing

Data have been evaluated using Matlab R2020a.

1. Processing of the PR-SFG data

The procedure of obtaining a complex-valued $\chi^{(2)}$ spectrum from a measured spectral interferogram is described in detail elsewhere (also see Section 2.1.3).[95,153,154] Similar to other works, we use z-cut single crystal quartz as a reference material. We apply $-90°$ phase correction to account for the phase difference between the surface and bulk SFG signals.[79,137,155] D_2O data demonstrate that an additional 34° phase correction is

needed to make the $\chi^{(2)}$ spectrum of D_2O real-valued in the 2800–$3000\,\text{cm}^{-1}$ frequency range. This phase correction is consistent with previous work,[152] and thus we use it for spectra of all the samples.
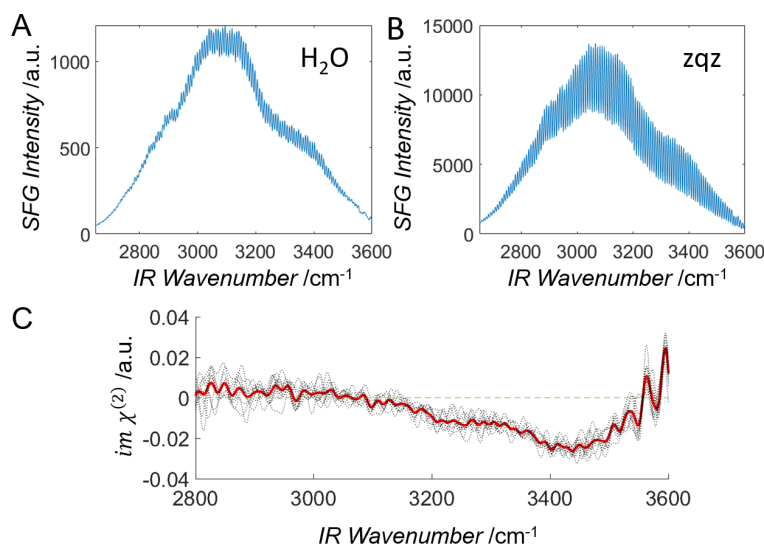

Figure 3.7: Interferograms and inferred $im\left[\chi^{(2)}\right]$ **spectra of the H_2O/air interface** - (A) Interferogram of the H_2O/air interface, averaged from 10 acquisitions of $2\,\text{minutes}$, each. (B) Interferogram of the z-cut quartz reference, averaged from 5 acquisitions of $60\,\text{seconds}$, each. (C) Imaginary part of the inferred $\chi^{(2)}$ spectra of the H_2O/air interface. The black dotted lines show the spectra of the 10 single $2\,\text{min}$ acquisitions. The red line shows their average.

2. Processing of the HeNe laser interference pattern

Acquired images were processed using ImageJ® software. To obtain a one-dimensional interference trace we take a slice of the image orthogonal to the interference lines and the color at the corresponding pixels is converted to signal intensity.

Suppression of a Background SFG Signal in Collinear Geometry

Our experimental setup does not produce a background SFG signal. However, the generation of "ghost" depends on the properties (cross-section, polarization, etc.) of VIS and IR beams as well as on the utilized optics and, thus, can vary between the experimental setups. Therefore, we additionally develop an effective filter to suppress a possible "ghost", which is based on a thin polymer film coating. To this end, we

spin-coat a $\sim 0.4\,\mu$m layer of PTB7 polymer (purchased from Ossila, Ltd.) on a 2 mm thick CaF_2 window. The round CaF_2 windows (diameter 1", thickness 2 mm) were purchased from Korth Kristalle GmbH. We spin-coat $\sim 100\,\mu$L of a 10 mg/ml polymer-chloroform solution at ~ 800 rpm. The film has an optical density (OD) of ~ 1.1 in the range of the SFG wavelength (~ 640 nm), and $\sim 70\%$ transmission of IR and VIS beams. The anti-ghost filter can be installed in the counterclockwise pathway inside the DS interferometer as shown in Figure 3.6 B. Test measurements demonstrate that the filter itself does not generate detectable SFG background. PR-SFG spectra of the H_2O/air interface measured with the filter are shown in Figure 3.8. We note that the OD of the filter at SFG wavelength and its transmission of the IR and VIS beams can be further enhanced by increasing the film thickness and improving its homogeneity, respectively.
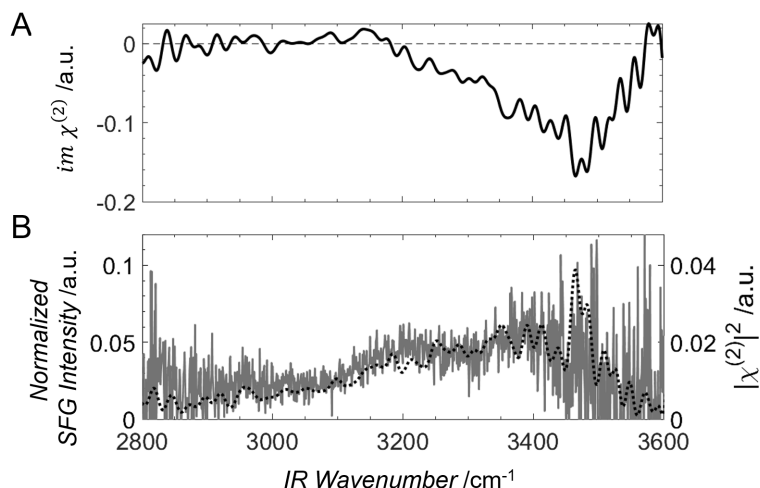
Figure 3.8: SFG spectra of the H2O/air interface measured with a PTB7 anti-ghost filter - (A) Imaginary part of the $\chi^{(2)}$ spectrum. (B) $\left|\chi^{(2)}\right|^2$ spectra measured with homodyne detection (solid grey) and calculated from the phase-resolved data in (A) (dashed black).

4

Electrostatic Interactions Control the Functionality of Bacterial Ice Nucleators

Reprinted with permission from M.
Lukas, R. Schwidetzky, A. T.
Kunert, et al. **Electrostatic In-
teractions Control the Function-
ality of Bacterial Ice Nucleators**.
*Journal of the American Chemical So-
ciety,* **142**(15):6842–6846, 2020. *Copy-
right 2020 American Chemical Society.
Minor changes were made to keep con-
sistency within this thesis.*
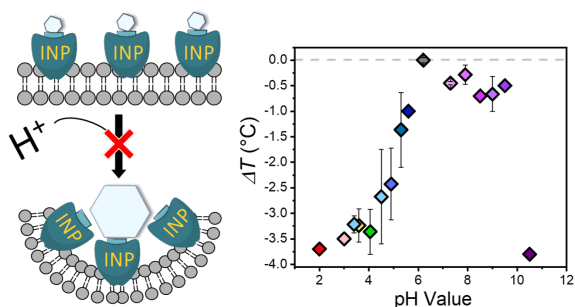
4. ELECTROSTATIC INTERACTIONS CONTROL THE FUNCTIONALITY OF BACTERIAL ICE NUCLEATORS

4.1 Abstract

Bacterial ice nucleation proteins (INPs) promote heterogeneous ice nucleation more efficiently than any other material. The details of their working mechanism remain elusive, but their high activity has been shown to involve the formation of functional INP aggregates. Here we reveal the importance of electrostatic interactions for the activity of INPs from the bacterium *Pseudomonas syringae* by combining a high-throughput ice nucleation assay with surface-specific sum-frequency generation spectroscopy. We determined the charge state of nonviable *P. syringae* as a function of pH by monitoring the degree of alignment of the interfacial water molecules and the corresponding ice nucleation activity. The net charge correlates with the ice nucleation activity of the INP aggregates, which is minimal at the isoelectric point. In contrast, the activity of INP monomers is less affected by pH changes. We conclude that electrostatic interactions play an essential role in the formation of the highly efficient functionally aligned INP aggregates, providing a mechanism for promoting aggregation under conditions of stress that prompt the bacteria to nucleate ice.

4.2 Introduction

Ice formation is the most important liquid-to-solid phase transition on earth and is strongly affected by the presence of nucleators that initiate heterogeneous ice nucleation at temperatures above $-40\,°C$. There is a large variety of compounds that can act as ice nucleators (INs), and their efficiency strongly differs.[14,156,157,158] The most efficient INs are bacteria from *Pseudomonas syringae*, which can initiate the crystallization of water at temperatures as high as $-2\,°C$.[36,41] The ability of bacteria to nucleate ice is caused by specialized ice nucleation proteins (INPs) that are anchored in the outer membrane on the bacterial cell wall.[47] Bacterial INPs contain a large central-repeat domain that has been proposed to be the active site and which is responsible for ice nucleation through a mechanism that likely involves the pre-ordering of water.[65,159] Apart from the specific ice-binding site, the high ice nucleation activity of INPs has been shown to depend on the size of the nucleation sites and the ability to aggregate into larger protein clusters.[26,73,160,161,162] INPs have repeatedly been shown to aggregate in the bacterial outer membranes,[47,71,157,158,162] and both, the number of INPs in the aggregate and

the sub-Ångström distance between the INPs affect the ice nucleation efficiency.[160] Based on their activity, the INP aggregates are typically divided into classes as shown in Figure 4.1.[26] Class A consists of large aggregates (> 50 INPs) that are responsible for freezing at temperatures between $-2\,°C$ and $-4\,°C$.[26] Class B consists of smaller aggregates that induce freezing at $-5\,°C$ to $-6.5\,°C$, and Class C has been assigned to mostly monomeric INPs that induce ice formation between $-7\,°C$ to $-12\,°C$.[26] In nature, the aggregation of INPs occurs under conditions of stress, which require the bacteria to nucleate ice.[36] The INP aggregation mechanism and whether INP aggregation in cell membranes is promoted by a change in chemistry is unknown. Notably, lowering the pH to acidic values has been shown to reduce the ice nucleation activity of bacterial INPs.[26,44,163,164] In contrast, changing the pH to alkaline values did not affect the nucleation activity.[26] The molecular origin for this pH sensitivity is unknown, but a better understanding would provide needed insights into the driving forces of INP aggregation. Moreover, it would have direct implications for understanding biological ice nucleation in the atmosphere, where pH levels are oftentimes acidic due to anthropogenic activities.[163]

4.3 Results & Discussion

Figure 4.1 shows the results of ice nucleation measurements of the bacterial IN Snomax® at three pH values. Snomax® is a commonly used model system for biological and atmospheric ice nucleation studies,[28,44,45] and it consists of a preparation of inactivated bacterial cells of *P. syringae*. The initial Snomax® solutions in water had a concentration of $0.1\,mg/mL$ and a pH of ~ 6.2. In the Twin-plate Ice Nucleation Assay (TINA, Section 2.2), the samples were then serially diluted, resulting in concentrations ranging from $1\,ng/mL$ to $0.1\,mg/mL$. The cumulative IN number concentration (N_m) was calculated using Vali's formula, and it represents the number of INs per unit weight that are active above a certain temperature.[129]

For the bacterial IN solution in water (pH ~ 6.2), the spectrum shows two strong increases in $N_m(T)$ around $\sim -2.9\,°C$ and $\sim -7.5\,°C$ with plateaus between $\sim -4.5\,°C$ and $\sim -7\,°C$ and above $\sim -9.5\,°C$. The two rises in the spectrum reveal that the ice nucleation activity of *P. syringae* stems from two classes of INs with different activation temperatures. The plateaus at temperatures T below each increase of $N_m(T)$ arise

4. ELECTROSTATIC INTERACTIONS CONTROL THE FUNCTIONALITY OF BACTERIAL ICE NUCLEATORS
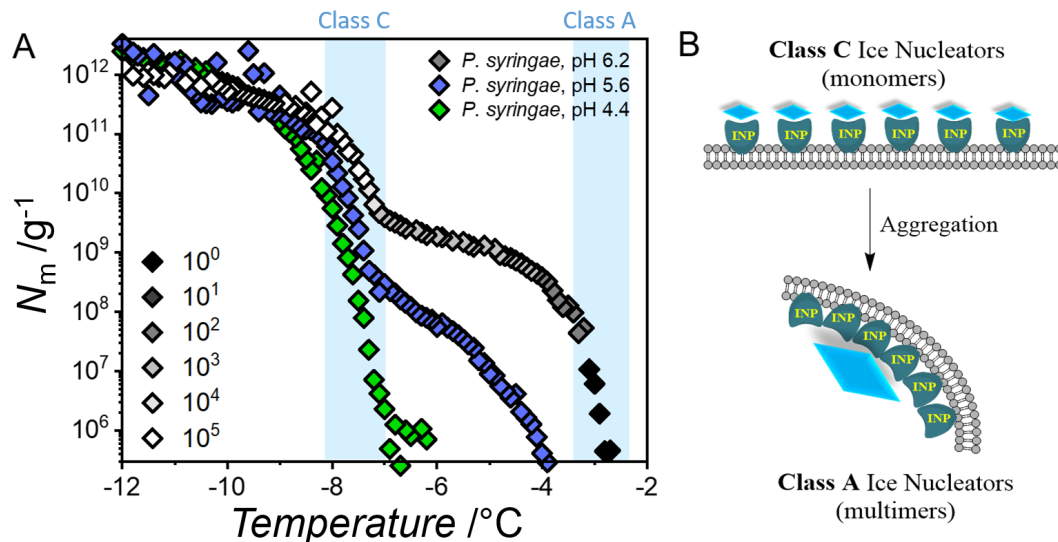

Figure 4.1: Freezing experiments of aqueous solutions of Snomax®, containing bacterial INs from *P. syringae*, in water and at different pH values - (A) Shown is the cumulative number of INs (N_m) per unit mass of Snomax® vs. temperature. Numbers in the legend denote dilution factors. The temperature ranges for Class A and C bacterial INs are shaded in blue.[26] (B) Schematic structure of Class A and C nucleators in a membrane. Class C refers to mostly monomeric INPs, which aggregate to form the highly efficient Class A nucleators. Both the number of INPs in the aggregate and the sub-Ångström distance between INPs affect the ice nucleation efficiency.

when fewer INs at these temperatures are present.[28] We attribute the observed rises at $\sim -2.9\,°C$ and $\sim -7.5\,°C$ to Class A and C INs, respectively.

For lower pH solutions, the trend looks markedly different. At pH 5.6 the rise at $\sim -2.9\,°C$ is absent; instead, we observe a rise at $\sim -4.5\,°C$. Further, the second rise at $\sim -7.5\,°C$ is slightly shifted by $\sim -0.5\,°C$. Evidently, lowering the pH influences the ability of the ice-nucleating proteins to form the more efficient Class A aggregates. Further lowering the pH fortifies this effect, and at a pH of ~ 4.4, the Class C nucleators have disappeared; apparently, Class A nucleators were converted into Class C. While Class A nucleators are very pH-sensitive, Class C nucleators are only weakly affected by pH variations.

To obtain a more detailed picture of the effect of the pH, we conducted a comprehensive evaluation of pH values of 2–10.5, as shown in Figure 4.2. We find that the change of pH gives rise to different effects, as shown in Figure 4.2 B: (i) Lowering the
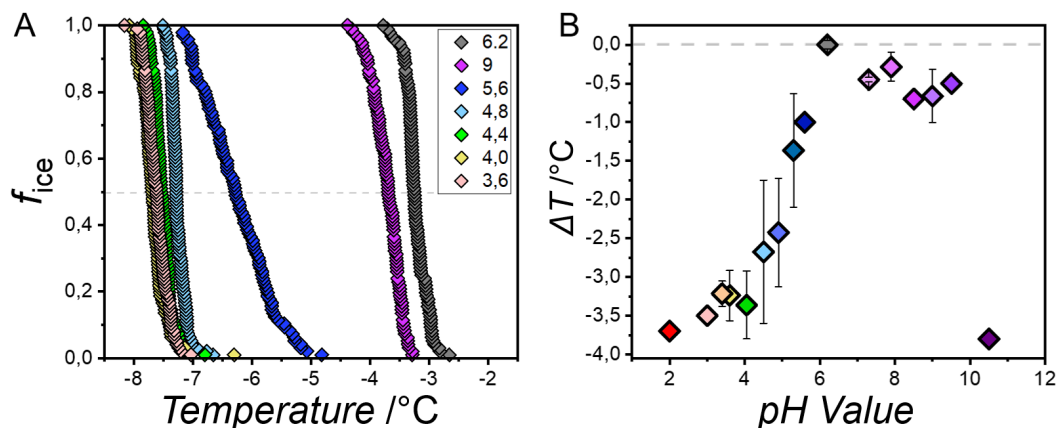
Figure 4.2: Freezing experiments of aqueous solutions of Snomax® containing bacterial INs from *P. syringae* at different pH values - (A) Fraction of frozen droplets (f_{ice}) for highly concentrated (0.1 mg/mL) Snomax® solutions. (B) Temperature shifts ΔT induced by different pH values. Shifts represent the difference at $f_{ice} = 0.5$ between Snomax® in water (pH ~ 6.2) and at different pH values. Error bars represent the standard deviation for multiple independent measurements.

pH to acidic values shifts the freezing point of Class A to lower temperatures. This trend continues until pH ~ 4, where the resulting freezing temperature $\sim -7\,°C$ closely resembles that of Class C nucleators. The more acidic conditions clearly prevent the formation of highly efficient Class A aggregates, reducing the activity of Class A to that of Class C. (ii) Raising the pH to basic conditions has a small effect on Class A ice nucleators, and the resulting response looks similar to that of bacteria in water, only shifted by $\sim 0.6\,°C$ to lower temperatures (Figures 4.2 B and 4.4 in the Supporting Information (SI)). (iii) Raising the pH to extreme basic conditions shifts the freezing point by $\sim 3.5\,°C$ to lower temperatures. The resulting freezing temperature of $\sim -7\,°C$ is again comparable to that of Class C nucleators.

To investigate the molecular origin of the strong pH dependence of bacterial INP's ice nucleation efficiency, we conducted sum-frequency generation (SFG) spectroscopic experiments of Snomax® adsorbed to the air/water interface at different pH values. SFG is a surface-specific method that can be used to probe interfacial water of biomolecules (Section 2.1.2).[165,166] In this technique, an infrared and a visible pulse are combined at a surface to generate light at the sum-frequency of the two incident fields. The technique is bulk-forbidden in isotropic media, and only ensembles of molecules with a
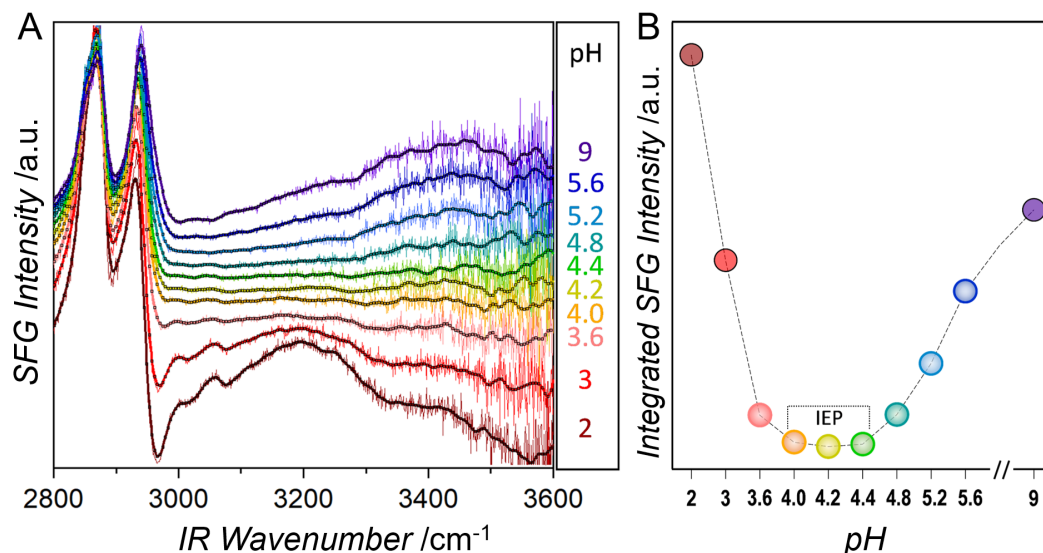
Figure 4.3: Results of the SFG experiments - (A) SFG spectra of aqueous solutions of Snomax® containing bacterial ice nucleators from *P. syringae* at the air-water interface, stacked as a function of bulk pH. The bulk concentration of Snomax® was $0.1\,\mathrm{mg/mL}$. (B) Integrated SFG intensity of the frequency region from ~ 3100 to $3600\,\mathrm{cm}^{-1}$ for Snomax® (*P. syringae*) at different bulk pH values.

net orientation, e.g., at an interface, can generate a detectable signal. The SFG signal intensity depends on the number of aligned molecules at the interface.

At charged surfaces, the surface field can align the water dipoles. Such charge-induced enhanced ordering of the interfacial water molecules causes the signal intensity in the O–H stretch region (3150–$3600\,\mathrm{cm}^{-1}$) to increase, and, inversely, the SFG signal intensity can be used to quantify the amount of charge at the electrified surface (Figure 4.5 in the SI and Figure 2.2). This concept has previously been applied to determine the isoelectric point (IEP) of proteins.[144,145,146,167] Figure 4.3 A shows pH-dependent SFG spectra of aqueous solutions of Snomax® adsorbed to the air-water interface. In the frequency region from 2800 to $3100\,\mathrm{cm}^{-1}$, the SFG spectra show strong signals from C–H stretch vibrations. At frequencies above $3100\,\mathrm{cm}^{-1}$, the spectrum shows a broad response from the O–H stretch band of interfacial water molecules. The SFG intensity of the C–H and O–H groups shows substantial changes when the solution pH is altered. We find that at pH values of ~ 4.2, the intensity of the O–H stretch signal is close to zero, whereas, at values below and above, the intensity of the O–H bands increases markedly and dominates the SFG spectrum of *P. syringae*. The observed changes in

the C–H region can be explained by interferences with the O–H resonances.[145,167] To more accurately determine the IEP of *P. syringae*, we integrated the SFG signal in the frequency region of ~ 3100–$3600\,\mathrm{cm}^{-1}$. Figure 4.3 B shows the pH dependence of the integrated intensity of the O–H stretch region. The lowest value for *P. syringae* was found at pH ~ 4.2, which corresponds to the point of no net charge or IEP of the bacteria. The interfacial IEP of ~ 4.2 is similar to the bulk IEP of 4.0 that was previously reported for *P. syringae* and consistent with the bulk IEP between 3 and 4 that we infer from zeta-potential measurements (Figure 4.6 in the SI).[168]

4.4 Conclusions

Ice nucleation bacteria are being studied extensively due to their important roles in precipitation and frost injury of plants.[169] Elucidating the impact of environmental factors such as the pH is essential for understanding not only atmospheric ice nucleation processes but also the functionality of INP aggregates. Electrostatic properties are governed by the distribution and ratio of charged and polar residues within protein structures and are among the most important factors that determine the functionality, stability, and interactions of proteins. We demonstrate that acidic pH values reduce the ice nucleation activity of non-viable *P. syringae* bacteria and that the effect arises from the inactivation of the highly efficient Class A aggregates active at high subzero temperatures. In contrast, we find no significant influence of mild basic pH values on the ice nucleation activity. The effect of acidic pH on the ice nucleation activity of *P. syringae* has previously been observed, and those results are consistent with our findings.[26,41,163,164] Turner *et al.* proposed that the acidic pH denatures the larger Class A INP complexes and that this process is irreversible.[26] Unlike Turner *et al.*, we observe that the ice nucleation activity of the Class A INP aggregates can be partially recovered upon raising the pH back to neutral values (Figure 4.7 in the SI). Combined, the pH-dependent SFG and droplet freezing experiments revealed that eliminating the net negative charge of *P. syringae* correlates with the decrease of the ice nucleation activity from the large Class A INP aggregates. We explain these observations with the formation of misfolded INP aggregates as a result of the decreased charge repulsion. Upon lowering the pH toward pH 4.2, negatively charged amino acids are protonated, and the net charge is reduced. The large numbers of glutamic acid residues contained in INPs

of *P. syringae* are likely candidates for protonation.[159] As a result of the protonation, the charge repulsion between INP monomers is absent, and hydrophobic interactions cause the INPs to misfold. These newly formed INP aggregates differ substantially from the precisely aligned functional Class A INP aggregates (see dynamic light scattering (DLS) results in the Figures 4.9 and 4.10 in the SI) and lack the ice nucleation activity at high subzero temperatures. Consequently, only single INPs or smaller aggregates, i.e., Class C nucleators, remain active at acidic pH, which is in line with our experimental observations. The finding that the ice nucleation activity can be recovered by going back to neutral pH further provides evidence that no irreversible denaturation of INPs occurs. In contrast, the drop of the freezing point at extremely basic conditions can not be recovered, which we explain with (partial) irreversible denaturation of the INP aggregates (Figure 4.11 in the SI). In nature, the aggregation of INPs occurs in the cell membrane of ice-nucleating bacteria under conditions of stress that require them to nucleate ice.[36] The alteration of the pH in the system would provide a means to trigger INP aggregation in the cell membrane.

4.5 Supporting Information

- Details on sample preparation and experimental methods

- Effect of alkaline pH on ice nucleation activity

- Orientation of interfacial water molecules at different pH values

- Results of the zeta potential measurements

- Reversibility of acidic and alkaline pH changes

- Results of the DLS measurements

Materials and Methods

Samples   Pure water was prepared as described elsewhere.[45] Snomax® was obtained from SMI Snow Makers AG (Thun, Switzerland) and contains a preparation of freeze-dried, irradiated bacteria cells of *Pseudomonas syringae*. Buffer materials (Tris, PBS, acetate) as well as NaOH and HCl were obtained from Sigma Aldrich (Darmstadt, Germany). The concentration of Snomax® was 0.1 mg/mL, and the pH value in pure water was 6.2 ± 0.2. The SFG and TINA experiments were performed in either pure water or in 0.1 M buffer solution (acetate, PBS, Tris,) of the respected pH. The ionic strength of the solutions was 0.1 M and adjusted by adding NaCl. The pH values of all samples were controlled before each measurement.

TINA experiments   Details are described in Section 2.2. Experiments were performed 3–6 times on independent samples.

DLS measurements   The hydrodynamic radii (R_h) of 0.1 g/L and 0.001 g/L Snomax® in ultrapure water and 0.1 g/L in 0.01 M HCl were determined using dynamic light scattering (DLS). Light scattering measurements were performed on an ALV spectrometer consisting of a goniometer and an ALV-5004 multiple-tau full-digital correlator (320 channels), which allows measurements over an angular range from 30 °C to 150 °C. A He-Ne laser (wavelength of 632.8 nm) was used as light source. Measurements were performed at 20 °C at 9 angles ranging from 30° to 150°.

4. ELECTROSTATIC INTERACTIONS CONTROL THE FUNCTIONALITY OF BACTERIAL ICE NUCLEATORS

Zeta potential   The Zeta potential measurements were performed using a Zetasizer (Malvern, UK) and a sample volume of $1\,\mathrm{mL}$. The pH of the Snomax® solutions was altered using NaOH and HCl.

Sum-Frequency Generation Spectroscopy Experiments   The details of the experimental setup have been described in Section 2.1.1 All spectra were obtained in the SSP-polarization combination (S-polarized SFG, S-polarized VIS, P-polarized IR). Background spectra were taken with a blocked IR beam and all spectra were normalized to reference spectra from z-cut quartz. The SFG measurements were performed in a custom-made Teflon trough at room temperature. The Snomax® (*P. syringae*) solutions were measured at a concentration of $0.1\,\mathrm{mg/mL}$. Samples were allowed to equilibrate for two hours before measurements. The equilibration of the samples at the interface was complete, when the SFG spectra did not change within one hour. The concentrations of the salts were adjusted to obtain identical ionic strengths (see *Colligative Effects*).

Colligative Effects   We exclude significant contributions of colligative effects on our results, since we performed measurements in buffer systems or by adjusting the pH value using NaOH and HCl. The ionic strength was kept constant at $0.1\,\mathrm{M}$ for all solutions and adjusted by adding NaCl. The maximum theoretical shift due to colligative effects in the TINA measurements would be $\sim 0.4\,°\mathrm{C}$ which is less than the observed shifts.
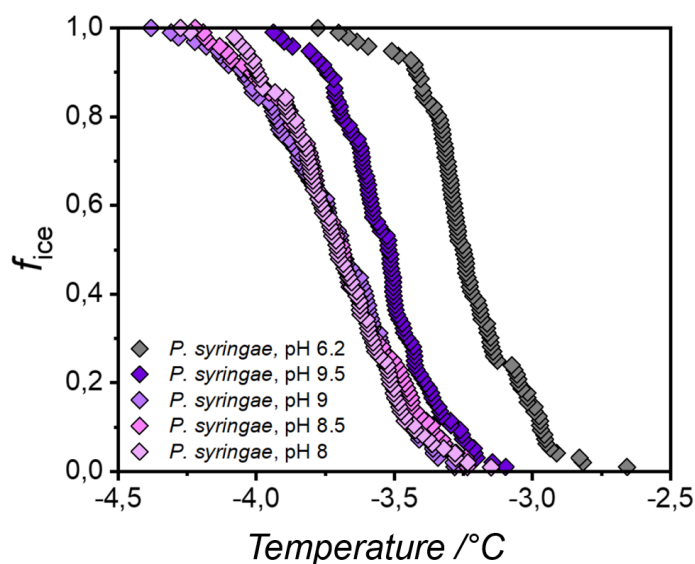
Figure 4.4: Freezing experiments of aqueous solutions of Snomax®, containing bacterial ice nucleators from *P. syringae*, at alkaline pH values. - Fraction of frozen droplets (f_{ice}) for highly concentrated ($0.1\,\text{mg/mL}$ samples) Snomax® (*P. syringae*) solutions.
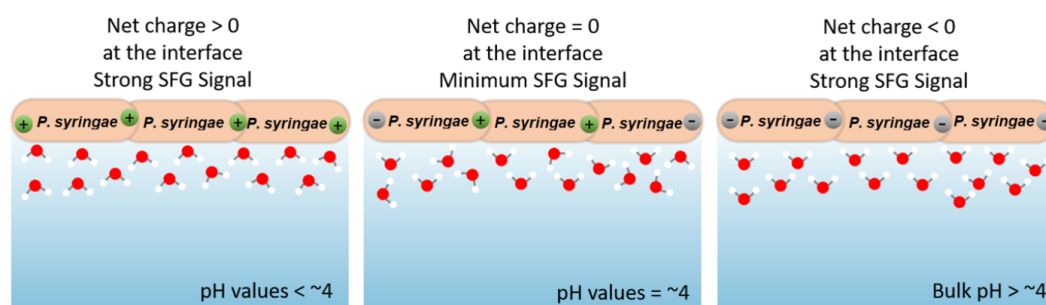

Figure 4.5: Schematic representation of the orientation of interfacial water molecules next to *P. syringae* at different pH values - *Compare Figure 2.2*

71
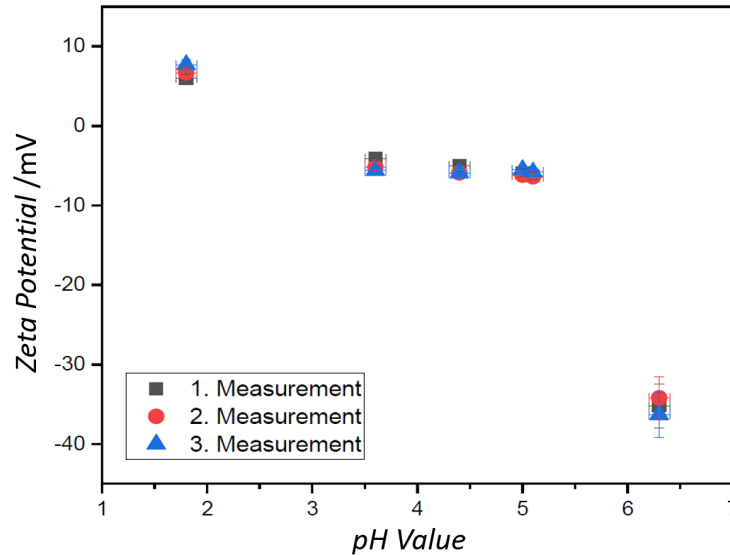
Figure 4.6: Zeta potential measurements of aqueous solutions of Snomax® containing bacterial ice nucleators from *P. syringae*, measured in 0.1 g/L solutions - From this plot, the isoelectric point was estimated to be between 3 and 3.5.
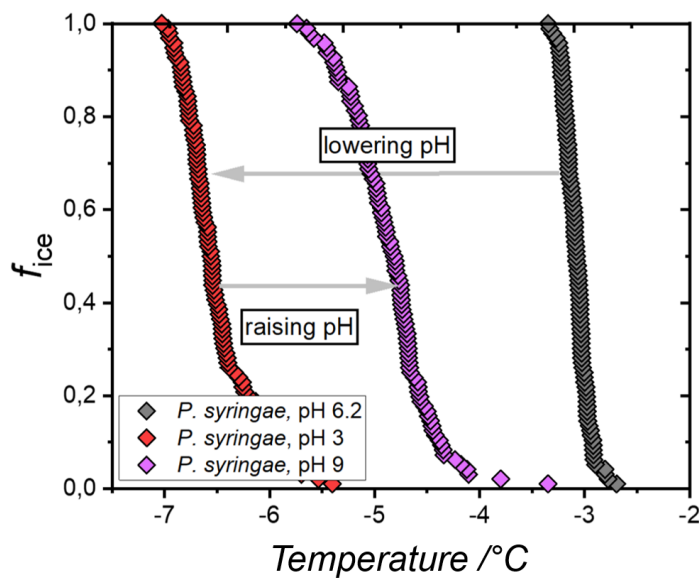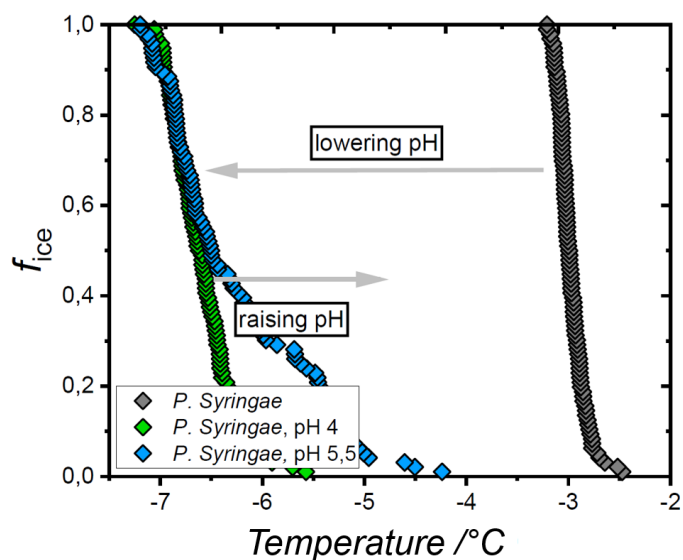

Figure 4.7: Freezing experiments of aqueous solutions of Snomax® containing bacterial ice nucleators from *P. syringae* as a function of pH values - Fraction of frozen droplets (f_{ice}) for highly concentrated (0.1 mg/mL) Snomax® (*P. syringae*) solutions, in which the pH was first decreased using HCl and then increased using NaOH.

Figure 4.8: Freezing experiments of aqueous solutions of Snomax® containing bacterial ice nucleators from *P. syringae* as a function of pH values - Fraction of frozen droplets (f_{ice}) for highly concentrated (0.1 mg/mL) Snomax® (*P. syringae*) solutions, in which the pH was first decreased and then increased using acetate buffer.
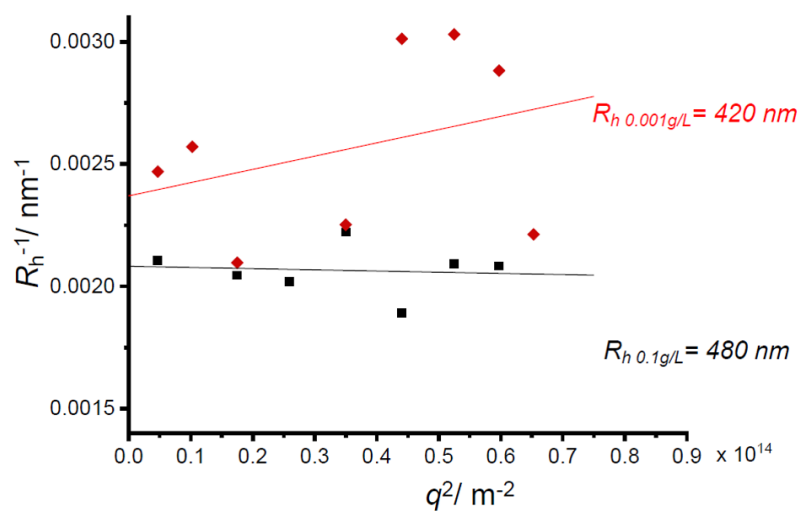

Figure 4.9: Hydrodynamic radii of Snomax® containing bacterial ice nucleators from *P. syringae* at 0.1 g/L and at 0.001 g/L - The radii at higher concentration are larger, suggesting that larger aggregates are present in the solution.
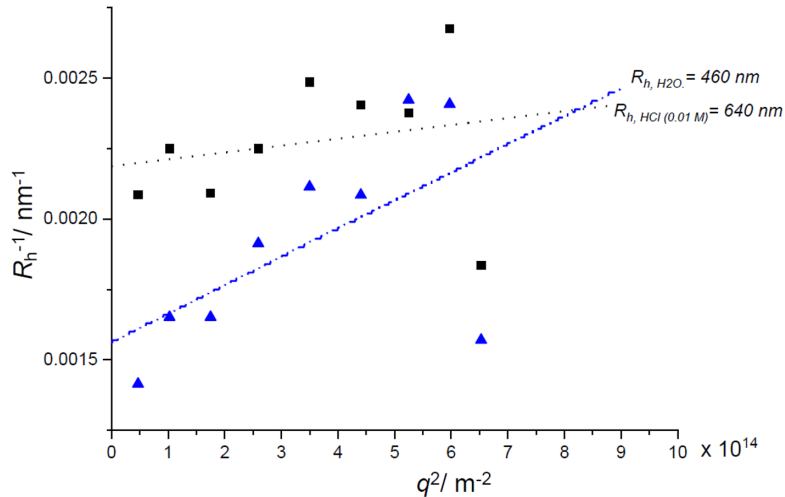
Figure 4.10: Hydrodynamic radii of Snomax® containing bacterial ice nucleators from *P. syringae* at 0.1 g/L in water (pH $\sim$ 6.2) and in 0.1 M HCl (pH $\sim$ 3.6) - The radii at lower pH are significantly larger, which shows that larger aggregates are present in the solution.

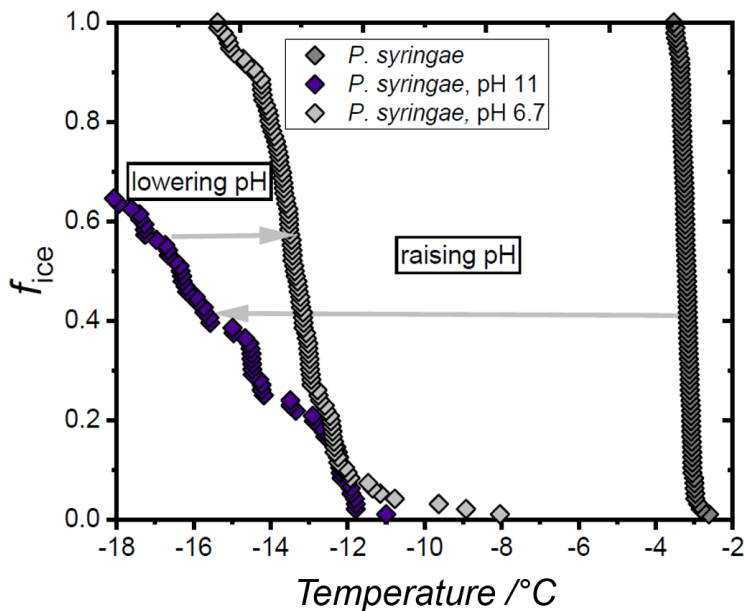**Figure 4.11: Freezing experiments of aqueous solutions of Snomax® containing bacterial ice nucleators from *P. syringae* as a function of pH values -** Fraction of frozen droplets (f_{ice}) for highly concentrated (0.1 mg/mL) Snomax® (*P. syringae*) solutions, in which the pH was first raised to pH 11 and then lowered to pH 6.7.

5

Specific Ion-Protein Interactions Influence Bacterial Ice Nucleation
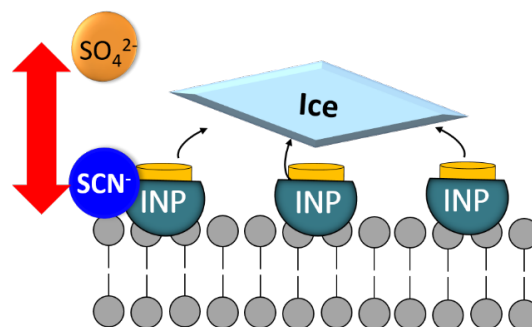
5. SPECIFIC ION-PROTEIN INTERACTIONS INFLUENCE BACTERIAL ICE NUCLEATION

5.1 Abstract

Ice nucleation-active bacteria are the most efficient ice nucleators known, enabling the crystallization of water at temperatures close to $0\,°C$, and thereby overcoming the kinetically hindered phase transition. Using highly-specialized ice nucleation proteins (INPs), they can cause frost damage to plants and influence the formation of clouds and precipitation in the atmosphere. In nature, the bacteria are usually found in aqueous environments which contain ions. The impact of ions on bacterial ice nucleation efficiency, however, has remained elusive. Here we demonstrate that ions can profoundly influence the efficiency of bacterial ice nucleators in a manner that follows the Hofmeister series. Weakly hydrated ions inhibit bacterial ice nucleation, whereas strongly hydrated ions apparently facilitate ice nucleation. Surface-specific sum-frequency generation spectroscopy and molecular dynamics simulations reveal that the different effects are due to specific interactions of the ions with the INPs on the surface of the bacteria. Our results demonstrate that heterogeneous ice nucleation facilitated by bacteria is strongly dependent upon the nature of the ions, and specific ion-protein interactions are essential for the complete description of heterogeneous ice nucleation by bacteria.

5.2 Introduction

At ambient conditions, the formation of ice from water is thermodynamically favored at temperatures below $0\,°C$, however, this crystallization process is kinetically hindered. As a result, pure water can be supercooled to temperatures as low as $-38\,°C$, below which homogeneous ice nucleation occurs.[16] In natural systems, water freezes in a heterogeneous process, facilitated by the presence of ice-nucleating substances of biological and abiotic origins.[161,162,170,171] Ice nucleation-active bacteria from *Pseudomonas syringae* are the best ice nucleators (INs) known, and their ability to induce ice formation at high sub-zero temperatures has direct impacts on agriculture, microbial ecology, geology and precipitation patterns.[163,172] The ability to nucleate ice is attributed to ice nucleation proteins (INPs). INPs are monomeric but have repeatedly been shown to form functional aggregates in the bacterial outer membranes and the largest INP aggregates (> 50 INPs) are thought to be responsible for enabling freezing close to $0\,°C$.[47,65,159] INP-induced ice nucleation usually takes place in ionic solutions, because ions are omnipresent in

76

the environment. Therefore, the effect of salts on the INP-mediated freezing of water is of fundamental interest. For homogeneous ice nucleation, it is established that ice formation depends on the water activity of the given aqueous solution, independently of the nature of the present ions[16]. In contrast, the effect of ions on heterogeneous ice formation facilitated by bacteria has remained largely elusive.[163,173,174]

The interaction of ions with proteins can be categorized by the Hofmeister series and has been observed for numerous processes.[175,176,177] In the 1880s, Franz Hofmeister ranked ions based on their ability to precipitate proteins from solution.[178] The work resulted in the following rankings for anions: $SO_4{}^{2-} > HPO_4{}^{2-} > Acetate^- > Cl^- > Br^- > I^- > SCN^-$ and for cations: $Gdm^+ > Mg^{2+} > Ca^{2+} > Li^+ > Na^+ > NH^{4+} > N(CH_3)^{4+}$, respectively.[179] Ions on the left side of the series stabilize and salt out proteins, whereas ions on the right denature and solubilize proteins. It is generally accepted that the Hofmeister series is an interfacial phenomenon, in which direct protein-ion-water interactions are of central significance.[175,180,181] Here, we investigate the effects of different ions on the ice nucleation activity of the proteinaceous INs from *P. syringae*.[28,44,45]

5.3 Results & Discussion

Figure 5.1 A shows the results of freezing experiments (Twin-plate Ice nucleation assay (TINA), Section 2.2) of a dilution series of the bacterial INs (Snomax®) in water and in aqueous solutions containing either 0.5 mol/kg sodium chloride (NaCl), ammonium chloride (NH$_4$Cl), sodium thiocyanate (NaSCN) or magnesium sulfate (MgSO$_4$). The freezing spectra of the bacterial INs in water and in the presence of MgSO$_4$ look similar and show two increases in the cumulative number of INs per unit mass of bacteria, $N_m(T)$, at $-2.9\,°C$ and $-7.5\,°C$ with plateaus between $-4.5\,°C$ and $-7\,°C$ and below $-9.5\,°C$. The two rises reveal that the ice nucleation activity of *P. syringae* is caused by two classes of INs with different activation temperatures, and we attribute them to Class A and C INs, respectively.[26] Class C ice nucleation is usually attributed to individual INPs or small assemblies in the bacterial membrane, and Class A ice nucleation is thought to originate from larger clusters of Class C INs, as shown in Figure 5.1 B.

5. SPECIFIC ION-PROTEIN INTERACTIONS INFLUENCE BACTERIAL ICE NUCLEATION

In the presence of NaCl, the freezing spectrum looks identical to the one of *P. syringae* in pure water, with a $\sim 2\,°C$ shift of the INP-mediated freezing curve to lower temperatures. This observed shift is in line with the expected shift of $-1.86\,°C$ based on the colligative melting point depression properties of a $0.5\,mol/kg$ NaCl solution (see Supporting Information (SI), Figure 5.5).[182] For NH_4Cl and NaSCN solutions, the trends look markedly different from those of *P. syringae* in pure water or NaCl solution. In the presence of NH_4Cl, the Class A-related rise at about $-2.9\,°C$ is absent; instead, we observe a small rise at $-7\,°C$. Further, the second rise is observed at $-9\,°C$, which again is $\sim 2\,°C$ lower than that in water and which is similar to the shift observed on adding NaCl. For NaSCN, we observe only a single rise centered at $-11.5\,°C$. Evidently, the four salts influence the efficiency of the INP-mediated freezing points differently.
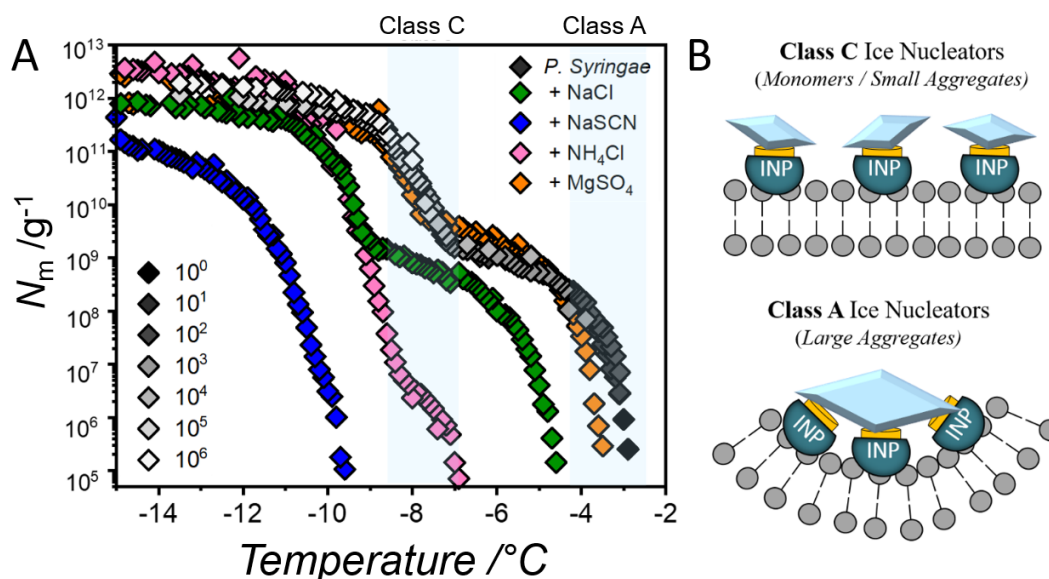

Figure 5.1: Freezing experiments of bacterial ice nucleators from *P. syringae* in aqueous solutions - (A) Results for INs in pure water (grey) and in aqueous solutions of $0.5\,mol/kg$ NaCl (green), NH_4Cl (magenta), NaSCN (blue), and $MgSO_4$ (orange). Plotted is the cumulative number of INs per unit mass of *P. syringae* vs. temperature for various degrees of dilution, starting with $0.1\,mg/mL$. Numbers and grey shades in the legend denote dilution factors and are shown for *P. syringae* in pure water only. The temperature ranges for Class A and C bacterial INs in water are shaded in blue. (B) Proposed schematic illustration of Class C and A ice nucleation structures. The high activity of bacterial INs relies on INPs, which assemble into larger functional protein clusters. The most effective IN clusters are termed Class A, consisting of large INP assemblies. Class C INs are less active and consist of smaller INP assemblies.

We examined whether different water activities in the investigated salt solutions may be the origin of the observed ion-specific effects on bacterial ice nucleation. Accounting for the effects of water activity, we found that they do not alter the respective observed influence of the salts on the INP-mediated freezing point (Figure 5.6 in the SI). In fact, NaCl, NH_4Cl, and NaSCN all have nearly identical water activities at $0.5\,mol/kg$, yet, they differ significantly in their effect on the bacterial ice nucleation activity. Clearly, the effects of salts on heterogeneous ice nucleation facilitated by bacterial INPs are not simply determined by water activity, as holds for homogeneous nucleation, and require further investigations.
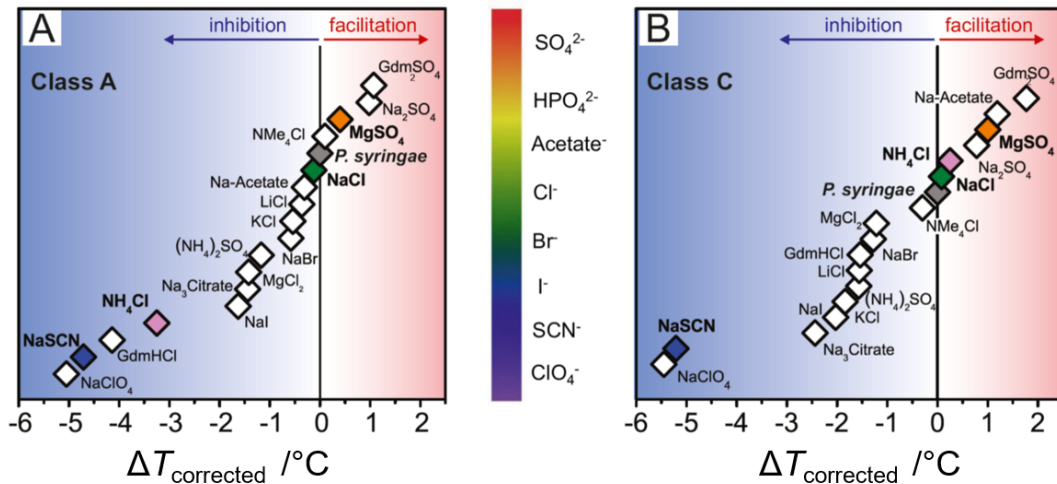

Figure 5.2: Effects of salts on the activity of bacterial INs from *P. syringae* - Shown are the temperature shifts (ΔT) induced by different salts on the freezing temperatures of Class A and Class C INs in water (grey diamonds). Vertically, the salts are ordered by the appearance of their anions in the Hofmeister series. The shifts represent the temperature difference for a frozen fraction of 50% of investigated samples ($f_{ice} = 0.5$) between *P. syringae* in water and the respective $0.5\,mol/kg$ salt solution. The latter are corrected for their water-activity effect (SI 5.5). The concentration of *P. syringae* was $0.1\,mg/mL$ for Class A INs (A) and $10^{-6}\,mg/mL$ for Class C INs (B). The corresponding anion Hofmeister series is shown in the inset.

We conducted a comprehensive experimental evaluation of seventeen salts of the Hofmeister series to obtain more details of the specific effects of ions on the bacterial INPs' activities. The experimentally determined freezing points in the salt solutions shown in Figure 5.2 were corrected for their respective water activity by taking the shifted melting points into account (see SI section 5.5).

5. SPECIFIC ION-PROTEIN INTERACTIONS INFLUENCE BACTERIAL ICE NUCLEATION

Four major categories can be identified from the plotted salt-induced shifts in freezing temperatures: (i) NaSCN influences both bacterial IN classes, Class A and C, and lowers their respective freezing temperatures; (ii) NH_4Cl lowers the freezing temperature of Class A, but does not affect Class C; (iii) NaCl has negligible effects on both freezing temperatures, and (iv) $MgSO_4$ increases the freezing temperatures of Class A and C. Interestingly, the effects of the salts on the INP-mediated freezing temperatures follows the individual anion's position in the Hofmeister series. Weakly hydrated ions such as SCN^- lower the INP-mediated freezing temperatures, whereas salts that have no effects, or apparently facilitate freezing, are more strongly hydrated ions such as Cl^- or SO_4^{2-}.

How can the different effects of the ions on the ice nucleation properties of the bacteria be explained? Different ions affect the local water structure, having different hydrogen bond-forming and -breaking capabilities.[175] Ions can, however, also alter protein conformations, and we surmise that both effects could alter the freezing behavior of INPs.[175] Clearly, molecular-level information is required to explore both possibilities. The combination of sum-frequency generation (SFG) vibrational spectroscopy experiments and molecular dynamics (MD) simulations is ideally suited for elucidating biomolecular conformations and biomolecule-water interactions.[159,165,181] SFG is a surface-specific method (Section 2.1.2) in which an infrared and a visible pulse are combined at a surface to generate light at the sum-frequency of the two incident fields. The selection rule of this spectroscopy dictates that only ensembles of molecules with a net orientation, e.g., at an interface, can generate a detectable signal. The SFG signal intensity depends on the number of aligned molecules at the interface. Changes in the solution pH were shown to strongly affect the SFG spectral response of bacterial ice nucleators (Chapter 4).[2] Therefore, all SFG experiments were performed in PBS buffer since the addition of salts can affect the solution pH in an ion-specific manner. At charged surfaces, the surface field can align the water dipoles, as illustrated in Figure 5.3 A. Such charge-induced enhanced ordering of the interfacial water molecules causes the SFG signal intensity in the O–H stretch region (IR wavenumber ~ 3100–$3600\,cm^{-1}$) to increase and, inversely, the SFG signal intensity can be used to quantify the amount of charge at the electrified surface. This concept has been used previously to investigate the effect of ions on biomolecules.[2,176,181,183]

Figure 5.3 B shows the SFG spectra of aqueous solutions of *P. syringae* adsorbed to the air-liquid interface in PBS buffer and in the presence of salts. The signals
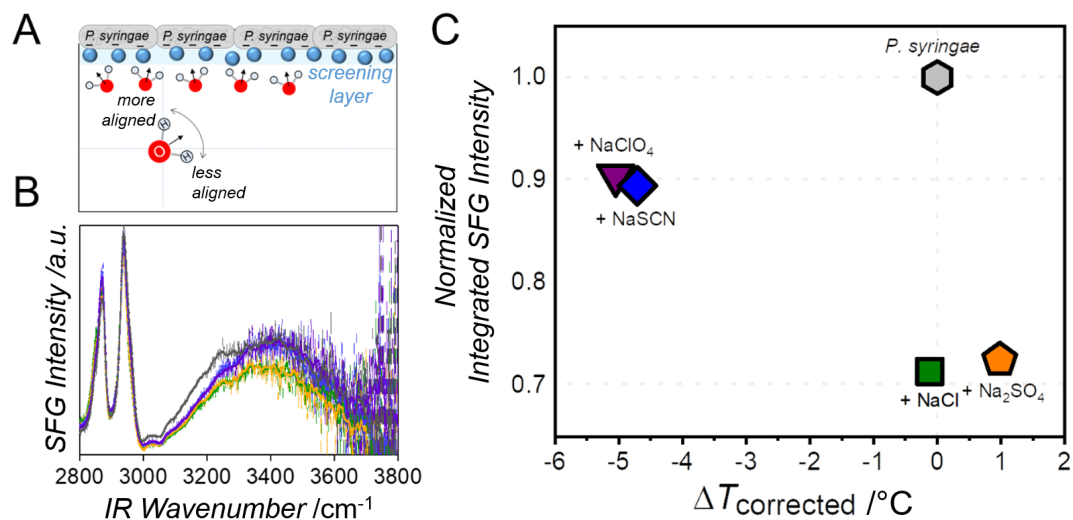
Figure 5.3: Sum-frequency generation spectroscopy measurements of bacterial ice nucleators from *P. syringae* in aqueous salt solutions - (A) Schematic representation of the orientation of interfacial water molecules next to *P. syringae* (grey) possessing a negative net charge. The straight arrows indicate the direction of the water dipoles and the blue spheres depict ions. The curved arrow indicates possible disruptions of the alignment due to the presence of salts. (B) SFG spectra of *P. syringae* layers at the air/liquid interface of a phosphate-buffered saline (PBS) solution (grey) and in the presence of NaCl (green), NaSCN (blue), NaClO$_4$ (purple), and Na$_2$SO$_4$ (orange). The bulk concentration of *P. syringae* was 0.1 mg/mL, and the salt concentrations were chosen to have identical ionic strength. (C) Normalized integrated SFG intensities of the frequency region from 3100–3600 cm^{-1} for *P. syringae* in PBS and in the presence of salts plotted against the respective Class A temperature shifts observed in the TINA experiments (Figure 5.2).

in the frequency region from 2800–3100 cm^{-1} originate from C–H stretch vibrations. The broad signal between 3100–3600 cm^{-1} is assigned to the O–H stretch band of interfacial water molecules. We integrated the SFG signal in the frequency region of 3100–3600 cm^{-1} to allow for a direct quantitative comparison of the effects of the salts as shown in Figure 5.3 C. The SFG intensity is highest in PBS buffer and decreases upon the addition of salts. This observation can be explained as follows: The cations of the salts screen the negative net charge of *P. syringae*, which in turn reduces the water molecules' alignment and causes the O–H stretch signal to decrease.[183] Interestingly, the salts show different efficiencies in screening the net charge despite the solutions having identical ionic strengths. The weakly hydrated anions decrease the SFG intensity less than strongly hydrated anions like SO$_4^{2-}$. One explanation for this observation is the preferred adsorption of weakly hydrated anions to the *P. syringae* surface, rendering

5. SPECIFIC ION-PROTEIN INTERACTIONS INFLUENCE BACTERIAL ICE NUCLEATION

it more negative and, in turn, causing more water alignment and increasing the O–H signal intensity compared to strongly hydrated anions, which prefer to stay solvated (Scenario 1). A second explanation is that the ions can change the INP conformation, thereby affecting the charge distribution of the protein, which would alter the water alignment and thus the SFG signal (Scenario 2).

To distinguish between both scenarios, we performed MD simulations of the solvated INPs in the presence of ions. The INP structure consists of fourteen repetitions of the amino acid sequence GYGSTQTSGSESSLTA as shown in Figure 5.4 A. The INP model adapts a β-helical structure, in excellent agreement with our circular dichroism spectrum of the purified INP (Figure 5.7, SI). We particularly focused on the water orientation and ionic distribution near the proposed active sites of the INP[67] and considered simulation settings, in which we kept the INP structure either flexible or fixed (see Methods, SI 5.5).

We analysed the water orientation ($\langle\cos\Theta\rangle$) relative to the IN-planes of the INP in the presence of the different salts (Figure 5.8, SI), where Θ is the angle between the water molecule's bisector and the plane normal of the active sites (see SI). We can directly compare the experimental and computational findings by obtaining the square of the integrated $\rho\langle\cos\Theta\rangle$ (ρ is the density of water), which is approximately proportional to the SFG intensity.[184]

The comparison of the SFG intensities and the square of $\rho\langle\cos\Theta\rangle$ (calculated SFG intensities) for the INP samples, presented in Figure 5.4 B, reveals that the simulations reproduce the experimental trend and capture the effects of the different ions on the water orientation near the INP well. In agreement with the experiments, we observe that weakly hydrated ions are found near the INP surface, rendering the protein more negative and enhancing water orientation relative to the active INs planes, while strongly hydrated ions show a gradual increase in the population when moving away from the INP surface to the bulk water (Figure 5.4 C). This finding is in line with Scenario 1 and consistent with the Hofmeister series. The depth profiles of the different ion species along the surface normal of the IN-planes are further largely different (Figure 5.4 C), underlining the different ion interactions with the protein.

To elucidate the possible effect of the protein conformation on the water orientation and ion distributions (Scenario 2), we computed the water orientation near the INP by fixing the protein geometry in the MD simulation (see SI 5.5). The fixed structure of

the INP shows the same trend for the ions, but the extent of the effects on the water orientation is reduced (Figure 5.4 B). We also examined the depth profile of the ion distributions for the fixed geometry (Figure 5.9, SI), and, compared to the flexible geometry, the weakly hydrated anions approach the fixed INP much less. Coming back to the two scenarios, these observations manifest that the change of the INP conformation and the propensity of the ions affect the water ordering property as competing scenarios.
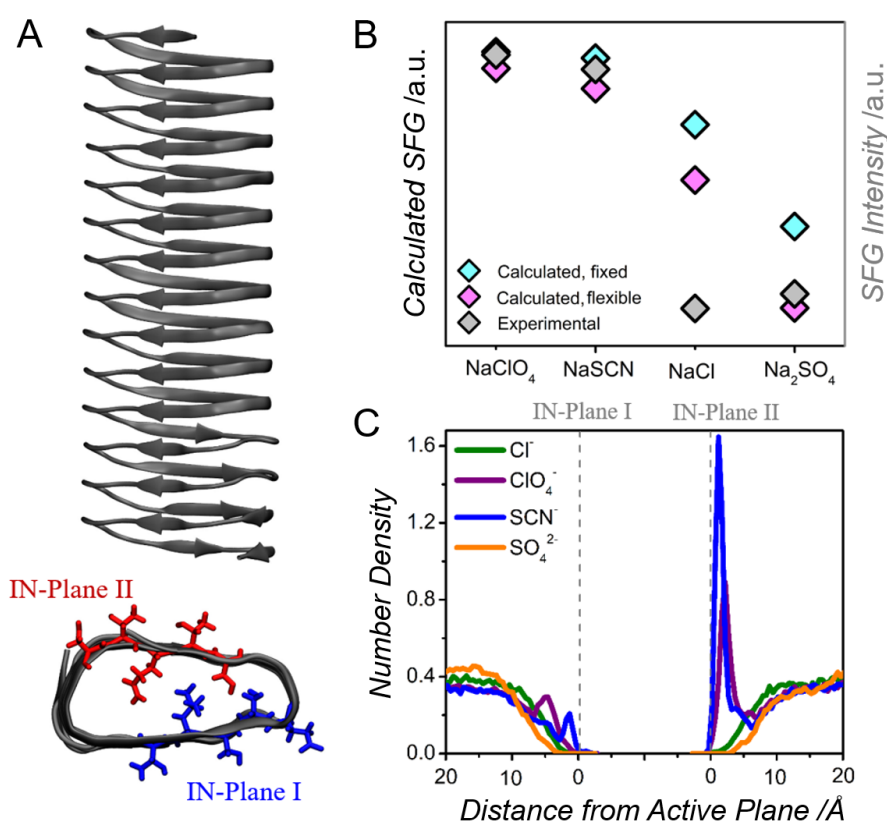
Figure 5.4: Molecular dynamics simulations of the INP from *P. syringae* -
(A) Model of the INP from *P. syringae*, consisting of 14 repeats and forming a β-helical
structure. The two ice-nucleating planes are highlighted in red and blue, respectively.
(B) Calculated and experimental SFG intensities in the presence of four different salts. In
the simulations, the INP structure was kept in either a fixed (cyan) or a flexible (magenta)
geometry. (C) Distribution of the anions with respect to the two active ice-nucleating planes
for the flexible geometry of the INP.

5.4   Conclusions

The above investigations suggest that ions affect the conformation and aggregation behavior of biomolecules in aqueous solutions very specifically, in addition to nonspecific electrostatic interactions. Our study provides unique insights into how different ions influence protein stability, aggregation, and, ultimately, the biological function of an organism. We provide clear evidence that the effect of ions on bacterial ice nucleation is not independent of the nature of the ion, but is due to specific ion-protein interactions that follow the trend of the Hofmeister series.

Weakly hydrated anions like perchlorate can directly interact with individual INP units and change their conformations and disable their individual IN sites (Figure 5.4, Figure 5.7, SI). The change in INP conformation further leads to the loss of the formation of the functional aggregates and collective alignment of INP units that enable freezing at $-2\,°C$ (Figure 5.1). We also note that ion addition can affect the pH value of the aqueous solutions in an ion-specific manner. Such pH changes strongly influence the ice nucleation activity of *P. syringae* as shown before (see Chapter 4),[2,163] and those results are consistent with the observations made for NH_4Cl in this work. Hence, the observed ion-specific inhibitory effect of NH_4Cl is entirely due to the change of the solution pH (Figure 5.10, SI).

Strongly hydrated ions enhance bacterial ice nucleation slightly. Sulfate ions were reported to decrease the reorientation time of water at the ice-binding-site of antifreeze proteins[185] and can create low-mobility water regions next to the active IN-sites of the INP (see Methods, Figures 5.11, 5.12). We speculate that such low-mobility regions may facilitate ice nucleation, in line with a recent MD simulation showing that low-mobility regions are the origin of seeds in homogeneous ice nucleation.[186]

Undoubtedly, fully intact INP structures and a precise sub-Ångström arrangement of INPs and water molecules are required for the extraordinary ice nucleation ability of INPs. The large variety of the salts investigated here, together with the different types of mechanisms by which ions affect bacterial INs, suggest that the general water activity-based ice nucleation criterion is not sufficient for a detailed description of the effects of solutes on bacterial IN. The water activity approach is valid for those cases, where the solutes do not directly affect the INs' surfaces, which is clearly not the case for the bacterial INPs studied here. We note that several of the salts studied here have

direct biological and atmospheric relevance and are found at similar concentrations in the environment, e.g., in natural cloud condensation nuclei.[173,187] As bacterial ice nucleation efficiency is controlled by complex and mutually interacting environmental variables such as the presence of co-solutes or pH, these all must be taken into account for a complete understanding and a validated environmental application of bacterial INs' properties.

5.5   Supporting Information

Experimental Contribution to the Project

- Details on sample preparation and experimental methods

- Melting Point Corrections

- Details of the MD Simulations

- Freezing spectra and temperature shifts; pH effects

- Circular Dichroism Spectra

Materials and Methods

Samples   Pure water was prepared as described elsewhere.[45] PBS-Buffer, the different salts, NaOH, and HCl were obtained from Sigma Aldrich (Darmstadt, Germany). Snomax® was purchased from SMI Snow Makers AG (Thun, Switzerland) and consists of a preparation of inactivated bacteria cells of *P. syringae*. The Snomax® concentration was 0.1 mg/mL, and the pH value in pure water was 6.2 ± 0.2. SFG and TINA experiments were performed in pure water or in 0.15 M PBS buffer. The pH values of all samples were measured before each measurement.

Colligative Melting Point Depression   The theoretical melting point depression of the salts was calculated according to the formula:

$$\Delta T_f = n \cdot c \cdot E_f = n \cdot c \cdot (-1.86 \, \text{K} \cdot \text{kg/mol}) \tag{5.1}$$

where c is the molality of the salt, n is the number of ions of the completely dissociated salt and E_f is the cryoscopic constant of water.[188]

Melting Point Correction   The reported shifts in ice nucleation temperature between *P. syringae* in pure water and in the different salt solutions in Figure 5.2 were corrected for the change in ice melting point due to the presence of the salt. The ice melting point of each salt solution at 0.5 mol/kg was determined as follows: For those salts for which ice melting point data as a function of salt concentration were available, these data were fitted and the interpolated ice melting point at 0.5 mol/kg was obtained. For the remaining salts, we used data of the osmotic coefficient at 0.5 mol/kg (at 25 °C) to

determine the water activity of the solution.[188,189,190] The water activity can then be used to determine the ice melting point using a previously established parameterization (assuming a temperature-independent water activity of the solution).[174] The latter procedure was checked with NaCl, and the two results agreed very well.

TINA Experiments   Details are described in Section 2.2. Experiments were performed multiple times on independent samples.

CD Spectroscopy   Circular dichroism experiments were performed on a Jasco-1500 CD-Spectrometer. Measurements were performed at an INP concentration of $\sim 0.01\,\mathrm{mg/mL}$ in pure water or in $0.5\,\mathrm{mol/kg}$ salt solutions. Samples were measured in a quartz cuvette at room temperature and the scan rate was $5\,\mathrm{nm/min}$ and the scan range was from 180–260 nm with data pitch 0.2 nm and data integration time 2 s. INPs of *P. syringae* (Snomax®) were purified using rotary ice-affinity purification as described elsewhere.[191]

Sum-Frequency Generation Spectroscopy Experiments   The details of the experimental setup have been described in Section 2.1.1 All spectra were obtained in the SSP-polarization combination (S-polarized SFG, S-polarized VIS, P-polarized IR). Background spectra were taken with a blocked IR beam and all spectra were normalized to reference spectra from z-cut quartz. The SFG measurements were performed in a custom-made Teflon trough at room temperature. The Snomax® (*P. syringae*) solutions were measured at a concentration of 0.1 mg/mL. Samples were allowed to equilibrate for two hours before measurements. The equilibration of the samples at the interface was complete, when the SFG spectra did not change within one hour. The concentrations of the salts were adjusted to obtain identical ionic strengths (molalities: $0.5\,\mathrm{mol/kg}$ for NaCl, NaSCN, NaClO$_4$; $0.16\,\mathrm{mol/kg}$ for Na$_2$SO$_4$). The pH-values of all samples were kept constant by measuring in PBS buffer.

MD Simulations

INP Model and Active Ice-nucleating Sites   Force field-based all-atom molecular dynamics simulations were performed using the Gromacs package. The INP model consists of a 16-amino acid ring (GYGSTQTSGSESSLTA), which was repeated 14

times, along the x-axis (Figure 5.4 A). The initial structure for INP was taken from Hudait *et al.*,[67] and its intra- and intermolecular interactions were parameterized using the OPLS-AA force field.[192] The active ice-nucleating sites were chosen based on the previous findings where STQTS and ESSLT sequences were found to induce ice nucleation with comparable efficiency.[67] These two sequences lie on opposite sides of the INP (Figure 5.4 A). We define two active ice-nucleating sites based on the ESSLT sequences on one side of the INP, as well as the STQTS sequence on the opposite side of the INP (IN-plane I and II, respectively). These planes are defined based on the atomic positions. To define a plane, we used two vectors that lie in the plane (V1 and V2). For the STQTS active plane, V1 was defined between the two Ser residues on the two sides of the sequence (<u>S</u>TQT<u>S</u>). Since INP has 14 rings, V1 was averaged over these 14 rings. V2 was defined between the alpha carbon of GLN (Q) in the second and one before the last ring in INP. For the <u>E</u>SS<u>L</u>T<u>A</u> active plane, V1 was averaged over the 14 rings between GLU and ALA residues, while V2 was defined for the LEU residues. Analysis of water orientation was performed based on the angle of water molecules bisectors $(\overrightarrow{OH_1} + \overrightarrow{OH_2})$ and the plane normal of the active ice-nucleating sites.

Simulation Protocols We ran the molecular dynamics simulations for five systems, with an initial dimension of $80 \times 55 \times 55 \text{Å}^3$, and periodic boundary conditions. All systems contained the solvated INP in water (modelled by the SPC/E water model), and 14 sodium ions to neutralize the net charge of INP. One of the systems did not contain any additional ions. The other systems each contained an ionic solution of Na-Cl, Na-ClO$_4$, Na-SCN, and Na$_2$-SO$_4$, with an ionic concentration of $\sim 0.8 \text{M}$, where the number of cationic species was twice for Na$_2$-SO$_4$ compared to the mono-valent anions. A position restraint was applied to the alpha carbon atom of all the Gly residues in INP (42 atoms in total) to stabilize its conformation, and results were compared to simulation, for which all the backbone atoms were under the position restraint. We refer to the former as the flexible and to the latter as the fixed INP geometry. Before the production molecular dynamics runs of 50 ns in using the NPT ensemble at 300 K, all the systems were stabilizing by minimizing the total energy of the systems. Subsequently, we increased the temperature gradually to 300 K during 2 ns, and we ran molecular dynamics simulation at 300 K for an additional 3 ns using the velocity rescaling through canonical ensemble method, followed by an NPT equilibration step of

5 ns, and a production run of 50 ns at 300 K. The pressure of the system was controlled by the Berendsen barostat. A time step of 1 fs was used to integrate the equations of motion and the atomic positions were stored every 10 ps. A cutoff radius of 10 Å was used for short-range van der Waals interactions. Long-range electrostatic interactions were treated by the Fast smooth Particle-Mesh Ewald (SPME) algorithm.

Ionic Species   The intra- and intermolecular force field parameters and the atomic charges for the ionic species are presented in Table 5.1.

Hydrogen Bond Lifetimes   To explore the hydrogen bond dynamics in the systems, and understand the effect of salts on the dynamics, we computed the autocorrelation time function of hydrogen bonds. The data are displayed in Figures 5.11 and 5.12. The hydrogen bond kinetics are not a single-step process[193,194], and should be interpreted considering various mechanisms. In fact, with fitting the hydrogen bond lifetime autocorrelation to a function in the form of $a\,exp\left(-\frac{t}{\tau_1}\right) + b\,exp\left(-\frac{t}{\tau_2}\right) + c_0$, we can correlate the two relaxation times to the breaking and re-formation of bonds, and to the fact that the movement of a molecule, will require collective rearrangement of the neighboring molecules.[195,196] The former is responsible for fast dynamics in the system, and the fast decay of the autocorrelation function (Figure 5.12), while the latter is responsible for the slow dynamics in the system.[195,197] Previous molecular dynamics simulations found that the lifetime of hydrogen bonds grows by $\sim$ 180 times close to the ice nucleation temperature and leads to very slow dynamics in the system.[198] Results for the two relaxation times are presented in Table 5.2, for the flexible and the fixed INP geometry. Corresponding error bars can be seen in Figure 5.12. We observe that for both relaxation times, the system which contains sulfate shows a longer relaxation time for hydrogen bonds, suggesting that this anion causes the dynamics to slow down. Furthermore, the effect of the different salts on the relaxation times is reduced when the fixed geometry of INP is considered (Figure 5.12), highlighting that the conformation of the INP affects the interaction of the ions with the INP.
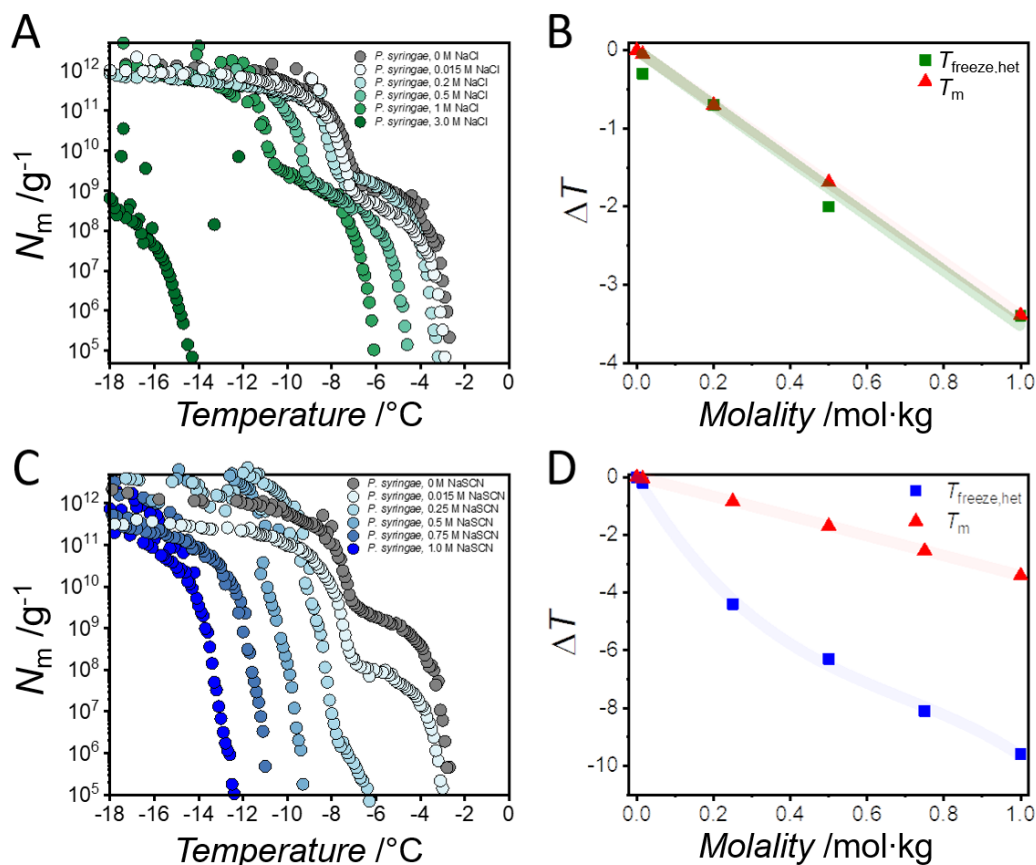
Figure 5.5: Freezing spectra and temperature shifts of aqueous solutions containing bacterial ice nucleators from *P. syringae* in pure water and in NaCl and NaSCN solutions - (A) Freezing experiments of aqueous solutions containing bacterial ice nucleators from *P. syringae* in pure water (grey) and in different NaCl solutions (green). Plotted is the cumulative number of ice nucleators per unit mass (N_m) of *P. syringae* vs. temperature for various degrees of dilution, starting with $0.1\,\mathrm{mg/mL}$. (B) Temperature shifts of the heterogeneous ice nucleation temperature (green squares) induced at different NaCl concentrations. Shifts represent the difference at $f_{ice} = 0.5$ between *P. syringae* in water and in NaCl solutions. The red line represents a linear fit of the ice melting temperatures (red triangles) and the green line is a linear fit of the experimental data. (C) Freezing experiments of aqueous solutions containing bacterial ice nucleators from *P. syringae* in pure water (grey) and in different NaSCN solutions (blue). (D) Temperature shifts of the heterogeneous ice nucleation temperature (blue squares) induced at different NaSCN concentrations. The red line represents a linear fit of the ice melting temperatures and the blue line is a cubic fit of the experimental data.

Table 5.1: Charges, inter- and intramolecular parameters for the ionic species. The references are given in parentheses:(1) Jorgensen *et al.*,[192] (2) Doherty *et al.*,[199] (3) Tesei *et al.*,[200] (4) Wang *et al.*,[201] (5) in-house Gaussian and AIMD calculations.

Ion		q [e]	ϵ [kJ.mol^{-1}]	σ [Å]	r [Å]	Bonds k [kJ.mol^{-1}.nm^{-2}]	α [D]	Angles k [kJ.mol^{-1}.Rad^{-2}]
Na$^+$ (1)		1.0	0.011598	3.33045	-	-	-	-
Cl$^-$ (1)		-1.0	0.492833	4.41724	-	-	-	-
ClO$_4^-$ (2)	Cl	1.176	0.493712	3.5	1.506	636384.0	109.5	1746.36
	O	-0.544	0.87864	2.9				
SCN$^-$ (3)	S	-0.573	1.523	3.83	(S-C) 1.66	577080.0	179.8	1308.72
	C	0.483	0.425	3.35				
	N	-0.910	0.310	3.7	(C-N) 1.19	2453640.0		
SO$_4^{2-}$	S	1.716 (5)	1.05 (4)	3.563 (4)	1.516 (5)	454524.0 (4)	109.43 (5)	626.64 (4)
	O	-0.929 (5)	0.882 (4)	2.960 (4)				

Table 5.2: Relaxation times of hydrogen bonds

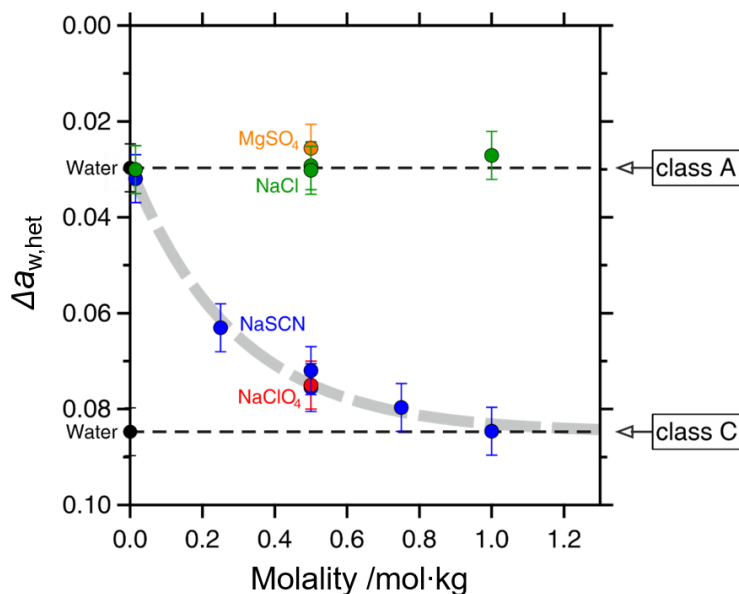|	τ_1 [ps]		τ_2 [ps]	
	INP	Fixed INP	INP	Fixed INP
No ions	9.09	9.24	126.90	126.21
Na-Cl	7.38	8.66	108.58	131.98
Na-ClO$_4$	7.63	9.73	109.29	139.06
Na-SCN	8.99	9.70	118.96	146.33
Na$_2$-SO$_4$	9.89	9.80	146.05	148.56

Figure 5.6: Water activity dependence of the freezing temperature of *P. syringae* in water and at different salt concentration - Plotted is the relative change $\Delta a_{w,het}$ between the water activity of the investigated salt solution (a_w) and that at the ice melting point $(a_{w,ice})$, both at the experimentally observed freezing temperature (T_{50}), as a function of the salt molality. $\Delta a_{w,het}$ was calculated from $\Delta a_{w,het}(T_{50}) = a_w(T_{50}) - a_{w,ice}(T_{50})$. The value of a_w of the different salt solutions was obtained from their ice melting points using a parameterization from the literature.[174] The black data points are the $\Delta a_{w,het}$ values in pure water for Class A and Class C IN, obtained from the T_{50} freezing temperatures at *P. syringae* concentrations of $0.1\,mg/mL$ and $10^{-6}\,mg/mL$, respectively. A constant $\Delta a_{w,het}$ as a function of salt molality (black dashed lines) indicates that the salt has a negligible effect on the efficiency of the particular IN, as is the case for NaCl (green). In contrast, the data for NaSCN (blue) and NaClO$_4$ (red) show an increase in $\Delta a_{w,het}$ with increasing salt molality, implying an inhibition of the particular Class A IN. An exponential fit to these data (grey dashed line) approaches the $\Delta a_{w,het}$ value of the Class C IN, implying that that the Class A INP aggregates are inhibited, while the individual Class C INPs appear not to be affected.
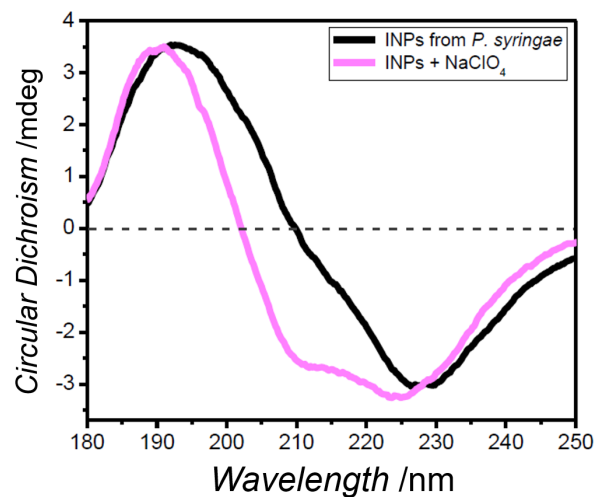
Figure 5.7: Circular dichroism spectra of the INPs from *P. syringae* in water (black) and in a 0.5 mol/kg $NaClO_4$ solution (magenta)
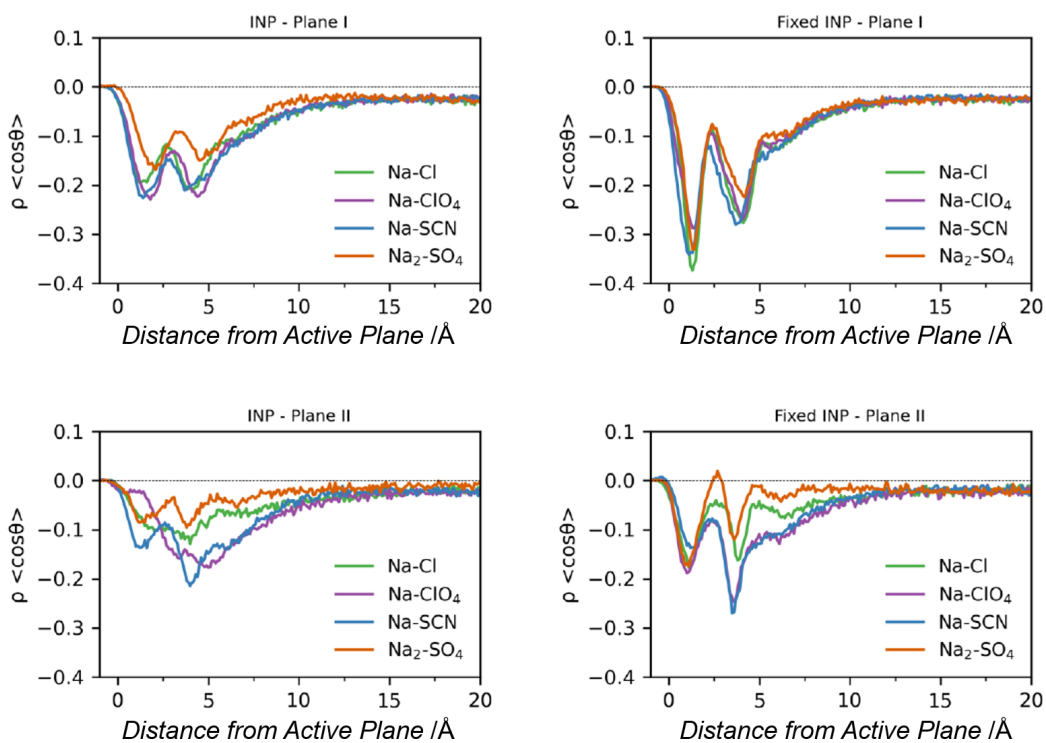

Figure 5.8: Density profile of $\rho \langle cos\theta \rangle$, where ρ is the density of water, and θ is the angle between water molecule's bisector and the plane normal, with respect to INP plane I and II, for INP in its fixed geometry.
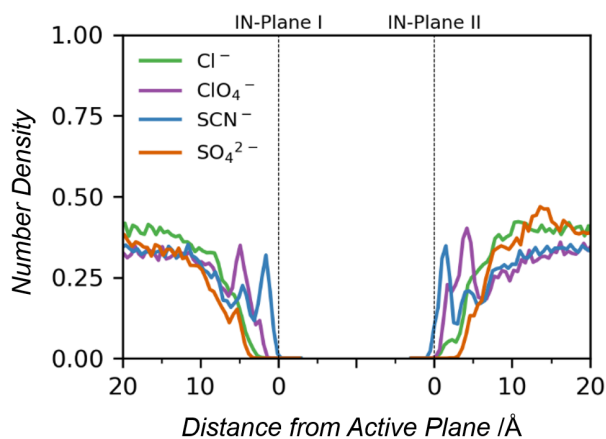
Figure 5.9: Anionic distribution with respect to the active sites for the fixed geometry of the INP.

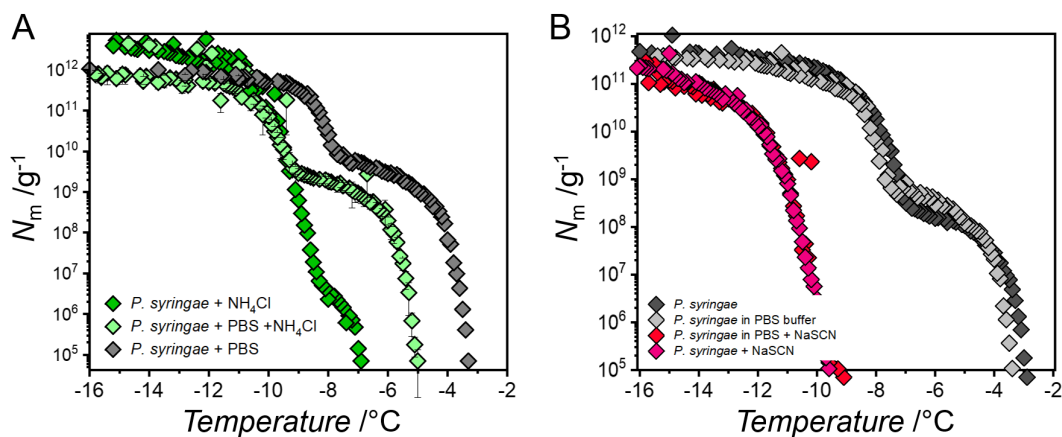**Figure 5.10: Freezing experiments of aqueous solutions of Snomax® containing bacterial ice nucleators from *P. syringae* in pure water compared to solutions containing NH₄Cl or NaSCN.** - Plotted is the cumulative number of INs per unit mass of *P. syringae*, N_m vs.temperature for various degrees of dilution, starting with 0.1 mg/mL. (A) Freezing experiments of aqueous solutions of Snomax® containing bacterial INs from *P. syringae* in pure water (grey), with NH₄Cl and with NH₄Cl in PBS buffer solutions, respectively. (B) Freezing experiments of aqueous solutions of Snomax® containing bacterial INs from *P. syringae* in pure water (grey), with NaSCN and with NaSCN in PBS buffer solutions, respectively
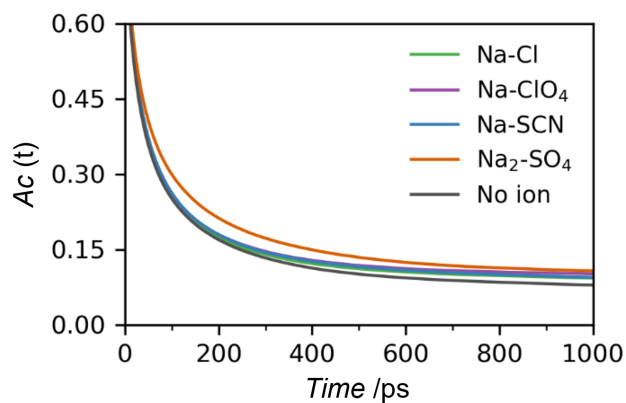
Figure 5.11: Hydrogen bond lifetime autocorrelation function for the INP in the presence of different salts - Water and groups involved in both active sites were considered to define hydrogen bonds. For each system, five tests were performed with a simulation time of 2 ns, where the trajectory was outputted every 50 fs.
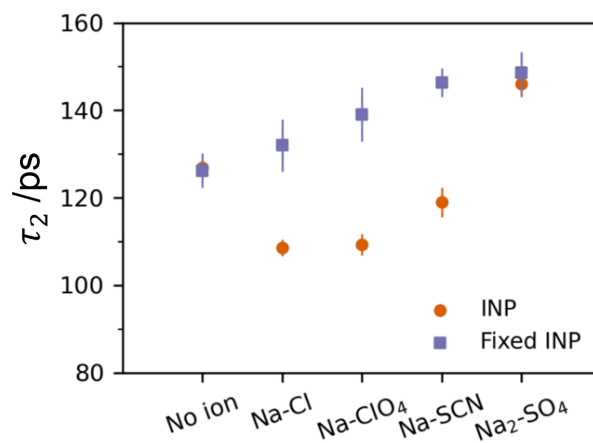

Figure 5.12: Relaxation times of the hydrogen bonds obtained from fitting the hydrogen bond lifetime autocorrelation function (Figure 5.10) to $a\,exp\left(-\frac{t}{\tau_1}\right) + b\,exp\left(-\frac{t}{\tau_2}\right) + c_0$. Values are shown with their standard error bars for the flexible and fixed INP, in the presence of different salts.

6

Interfacial Water Ordering Is Insufficient to Explain Ice Nucleation Protein Activity

6. INTERFACIAL WATER ORDERING IS INSUFFICIENT TO EXPLAIN ICE NUCLEATION PROTEIN ACTIVITY

6.1 Abstract

Ice nucleation proteins (INPs) found in bacteria are the most effective ice nucleators known, enabling the crystallization of water at temperatures close to 0 °C. Although their function has been known for decades, the underlying mechanism is still under debate. Here, we show that INPs from *Pseudomonas syringae* in aqueous solution exhibit a defined solution structure and show no significant conformational changes upon cooling. In contrast, irreversible structural changes are observed upon heating to temperatures exceeding ~ 55 °C, leading to a loss of the ice nucleation activity. Sum-frequency generation spectroscopy reveals that active and heat-inactivated INPs impose similar structural ordering of interfacial water molecules upon cooling. Our results demonstrate that increased water ordering is not sufficient to explain INPs' high ice nucleation activity and confirm that intact three-dimensional protein structures are critical for bacterial ice nucleation, supporting a mechanism that depends on the INPs' supramolecular interactions.

6.2 Introduction

The formation of ice is thermodynamically favored in water at temperatures below 0 °C, but the crystallization is kinetically hindered owing to the energy barrier associated with creating the initial ice seed.[8] As a result, pure water droplets can, depending on their size and cooling rate, be supercooled to temperatures as low as -38 °C.[16] Ice crystals can be formed either by homogenous nucleation at lower temperatures, or by heterogeneous nucleation catalyzed by compounds that serve as ice nucleators (INs). The most effective biological INs known are ice nucleation proteins from bacteria such as *Pseudomonas syringae*.[36,41] Bacterial INPs can have different sizes, but are typically large macromolecules that are anchored to the outer cell membrane of the bacterial cell wall.[36,47] They are typically present as monomers, but have repeatedly been shown to aggregate in the bacterial outer membranes.[47,71,157] Large INP aggregates are thought to be responsible for freezing at temperatures between -2 °C and -4 °C and smaller INP aggregates at temperatures between -7 °C and -12 °C.[26]

Computer-based homology modeling proposed the bacterial INP structure to be β-helical (Figure 6.1 A) with similarities to hyperactive insect antifreeze proteins (AFPs).[65]

More recent models based on molecular dynamic simulations further suggest that a highly conserved threonine-X-threonine motif is used to interact with ice, which again is similar to some AFPs.[202] On the molecular scale, the INPs are believed to work by organizing water into preordered patterns, which increase in size as the temperature decreases until they are large enough to form a stable embryonic crystal, leading to ice growth.[58] However, the role of the INP structure, the interaction of INPs with water, and the underlying working mechanism remain largely unknown. Here, we study the effects of temperature on the structure, hydration shell and ice nucleation efficiency of purified proteinaceous INs of *P. syringae*.

6.3 Results & Discussion

We performed purification of fragmented *P. syringae* (Snomax®) solutions using falling water ice affinity and rotary ice-shell purification (see Supporting Information (SI) section 6.5 for details).[203,204] Both purification methods use the unique property of the INPs to bind to ice and have previously been used to purify AFPs from natural sources.[191] The purification process involved the incorporation of the INPs into the slowly growing ice phase and the exclusion of other biomolecules and impurities. Using this ice affinity purification, we obtained a mixture of all the INPs present in *P. syringae*, including residual protein-associated lipids. The success of the purification was assessed by determining the ice nucleation activity of the purified INPs using the high-throughput Twin plate Ice Nucleation Assay (TINA, Section 2.2).[45] In the following, we will refer to these purified samples as "purified INPs".

Figure 6.1 B shows typical statistical freezing curves of aqueous solutions of fragmented *P. syringae* and purified INPs with 0.1 mg/mL, and Figure 6.1 C shows the cumulated freezing spectra inferred from freezing curves recorded for concentrations spanning from 0.1 mg/mL to 1 ng/mL (see also Figure 6.7 in the SI) using Vali's equation.[45,129] The freezing spectrum of *P. syringae* displays two substantial increases in the cumulative number of IN per unit mass, $N_m(T)$ (Figure 6.1 C) around $-3.0\,°C$ and $-7.5\,°C$ with plateaus between $-4.5\,°C$ and $-7.0\,°C$ and below $-9.5\,°C$. At the plateaus, at temperatures below each increase of $N_m(T)$, fewer INs are active.[28] The two rises in the curve reveal that the ice nucleation activity stems from two distinct classes of INs with different activation temperatures. We attribute the observed rise at $-3.0\,°C$ to large

assemblies of INPs (Class A INs) and the rise at 7.5 °C to smaller assemblies of INPs (Class C INs) in accordance with previous studies.[2,26,36,69,205,206] The freezing curve of the purified INPs looks similar to the non-purified INP solution, with a change in the ratio of the INP number in the two classes at −3.0 °C and 7.5 °C (see also Figure 6.6, SI). Clearly, the purification process was successful and yielded active INPs. The reduction of Class A IN activity for the purified sample indicates that the purification reduced the number of the larger INP aggregates compared to the non-purified solution. This observation is in line with the hypothesis that the bacterial membranes are involved in the formation of larger functional INP aggregates,[47,65,73,207,208,209,210] and we expect bacterial membrane fragments to have no ice affinity.
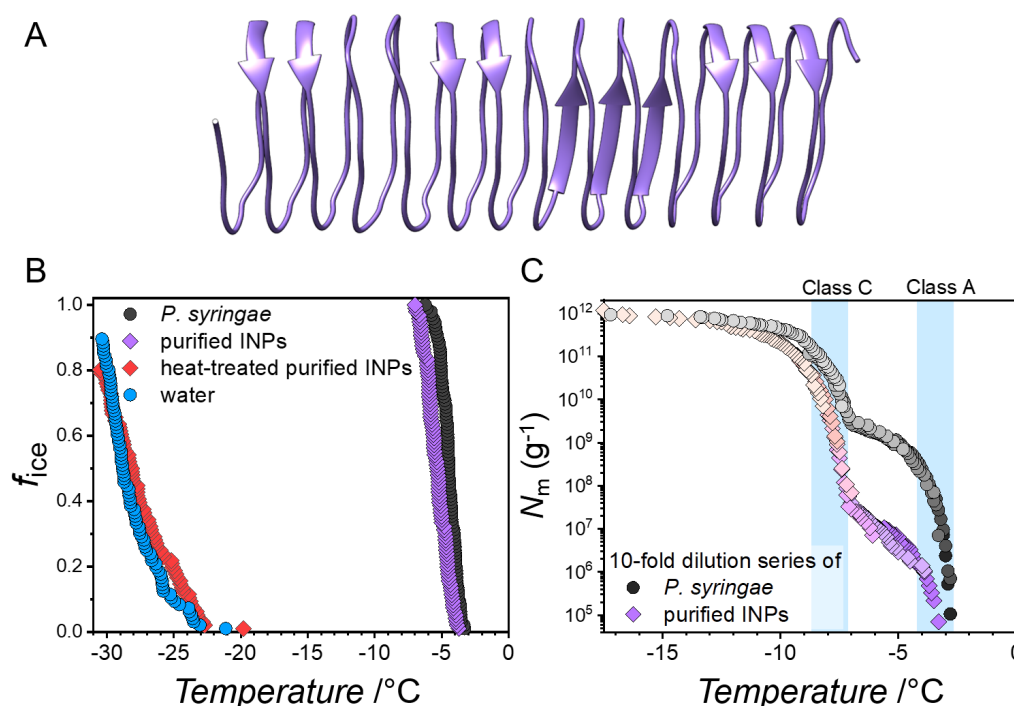

Figure 6.1: Structure and ice nucleation activity of the proteinaceous ice nucleators from *P. syringae* - (A) Model structure of the INP of *P. syringae*, possessing a β-helical fold.[67] (B) Statistical freezing curves of aqueous *P. syringae* solutions and their purified INPs, compared to the heat-inactivated INPs and the freezing curve of pure water in our system. Shown is the fraction of frozen $3\,\mu$L droplets (f_{ice}) vs. temperature for the highest concentrations ($0.1\,$mg/mL) of the utilized dilution series. (C) Freezing spectra of aqueous dilutions ($10^{-1}\,$mg/mL to $10^{-6}\,$mg/mL) of *P. syringae* and their purified INPs. Shown are the cumulative numbers of active INs (N_m) per unit mass vs. temperature. The temperature ranges for Class A and Class C bacterial INs in water are shaded in blue.

Heat-treated INP solutions (see SI section 6.5 for details on heat treatment) behave fundamentally differently. As apparent from comparing the droplet freezing statistics of the highest dilution concentrations shown in Figure 6.1 B, the rises at $-3.0\,°C$ and $-7.5\,°C$ are completely absent. Instead, we only observe activity around $-25\,°C$, which corresponds to background freezing of pure water in our system (Section 2.2). Evidently, the heat treatment of the purified INPs completely inactivates their ice-nucleation abilities.

Using sum-frequency generation (SFG) vibrational spectroscopy, Pandey *et al.* reported that fragmented *P. syringae* bacteria (Snomax®) show an increased capability to order water in their vicinity when cooled to temperatures close to the melting point of deuterated water.[159] Control experiments using misfolded and denatured INP fragments, lipids, and the protein lysozyme did not show this effect. The alignment of water into an ordered structure was concluded to be a condition that will promote interfacial ice nucleation.

Here, we conducted further SFG experiments with active and heat-inactivated INPs to determine whether there is a direct causal correlation between enhanced SFG water signals at low temperatures and bacterial ice nucleation activity. In SFG (Section 2.1.2), a broadband infrared pulse resonant with the probed molecular vibrations and a visible pulse are combined at a surface to generate light at the sum-frequency of the two incident fields. The SFG process is bulk-forbidden in isotropic media, and only ensembles of molecules with a net orientation, e.g., at an interface, can generate a detectable signal.

Figure 6.2 shows the temperature-dependent SFG spectra of aqueous solutions of purified INPs. The broad response from the O–D stretch bands of interfacial water molecules appears at frequencies below $2700\,cm^{-1}$ and is affected by their interactions with the INPs adsorbed to the air/liquid interface. In the frequency region of 2800–$3000\,cm^{-1}$, the SFG spectra show strong signals that we attribute to C–H stretch vibrations.

The SFG intensity of the O–D bands strongly increases upon lowering the temperature close to the melting temperature ($3.82\,°C$ for D2O), indicating an increase in the structural order of the interfacial water molecules. This effect is completely reversible, as evident from the integrals of the water (O–D) bands for two cycles shown in the insets. The observed increase ($\sim 36\%$) is also significantly larger than the increase observed for pure water ($\sim 12\%$, insets in Figure 6.2 and Figure 6.8 in the SI).[211] In
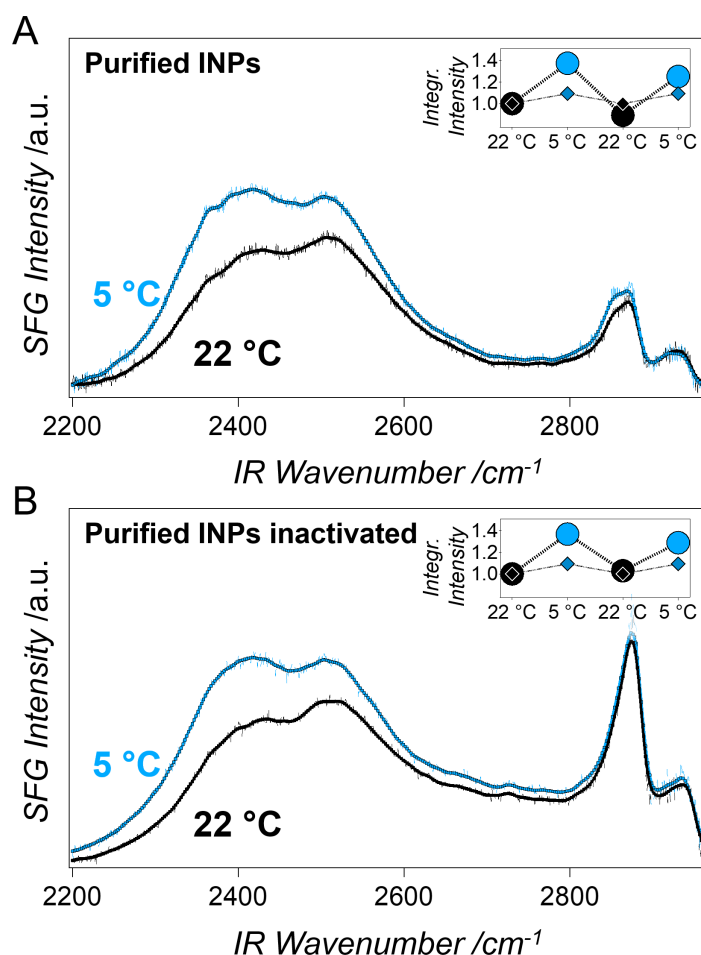
Figure 6.2: Temperature-dependent SFG measurements of aqueous solutions of active and heat-inactivated proteinaceous ice nucleators purified from *P. syringae* - (A) SFG spectra of the active INPs at the air-liquid interface in D_2O at 22 °C and 5 °C, respectively. (B) SFG spectra of the heat-inactivated INPs at the air-liquid interface in D_2O at 22 °C and 5 °C, respectively. The bulk INP concentrations were 0.1 mg/mL. The insets show the integrated SFG intensities in the O–D stretch frequency region of ∼ 2200–2700 cm^{-1} for two temperature cycles (circles) compared to pure D_2O (squares), normalized to the respective first value at 22 °C.

contrast, the signal intensity of the C–H stretch vibrations remains constant upon lowering the temperature. Figure 6.2 B shows temperature-dependent SFG spectra of aqueous solutions of heat-inactivated INPs. Interestingly, we find that the completely inactive INPs adsorbed to the air-liquid interface cause a comparably strong increase in the SFG intensity of the O–D signals upon lowering the temperature. Thus, we conclude that the enhanced interfacial water ordering at low temperatures cannot be directly associated with the presence of ice nucleation active sites.

Interestingly, while the water response is indistinguishable between the active and inactivated INPs, marked changes occur in the C–H stretch region. Although we cannot precisely assign the manifold C–H stretch contributions in the SFG spectra, these changes indicate that there is a substantial change in the protein structure after inactivation.

Figure 6.3 A shows SFG spectra in the Amide I region, which is sensitive to the secondary structure and orientation of proteins.[166,212] The Amide I SFG spectra at room temperature and close to the melting temperature look very similar and show a strong signal at $\sim 1645 \, \text{cm}^{-1}$ and a weak signal at $\sim 1710 \, \text{cm}^{-1}$. We assign the signal at $1645 \, \text{cm}^{-1}$ to the protein backbone of the INPs[143,213,214] and the weak signal at $1710 \, \text{cm}^{-1}$ to carbonyl groups in lipid molecules (see also Figure 6.9, SI).[98,215,216] The lipid signal presumably originates from membrane lipids that remain protein-associated during the purification, which is in line with the presence of Class A aggregates in our freezing experiments (Figure 6.1 B). The observation that the Amide I SFG spectra do not change upon cooling, suggests that no structural or conformational changes of the INPs occur upon approaching biologically relevant working temperatures. These conclusions are supported by temperature-dependent CD spectra that also show very little changes upon lowering the temperature (Figure 6.3 B). Upon heating of the purified INPs, the Amide I SFG response and the CD spectrum undergo marked changes, as evident from Figures 6.3 A and B, respectively. Figure 6.3 A shows that the interfacial protein backbone SFG signal at $\sim 1645 \, \text{cm}^{-1}$ of heat-inactivated INPs is increased, while the lipid signal at $\sim 1710 \, \text{cm}^{-1}$ appears unaffected. The CD spectrum of the active INPs in Figure 6.3 B shows a maximum molar ellipticity at $195 \, \text{nm}$ and a minimum at $228 \, \text{nm}$, after which there is a gradual return to zero from 230 to $260 \, \text{nm}$. Increasing the temperature reduces the molar ellipticity at $195 \, \text{nm}$, and the minimum at $228 \, \text{nm}$ reduces (see also Figure 6.11, SI). These spectral changes following heating above $\sim 55 \, °\text{C}$

suggest significant, irreversible alterations in the secondary structure contents of the INPs. We propose that the observed irreversible conformational changes cause a loss of the proteins' native functional structure and are the origin of the complete elimination of the INP's ice nucleation activity after heat treatment.
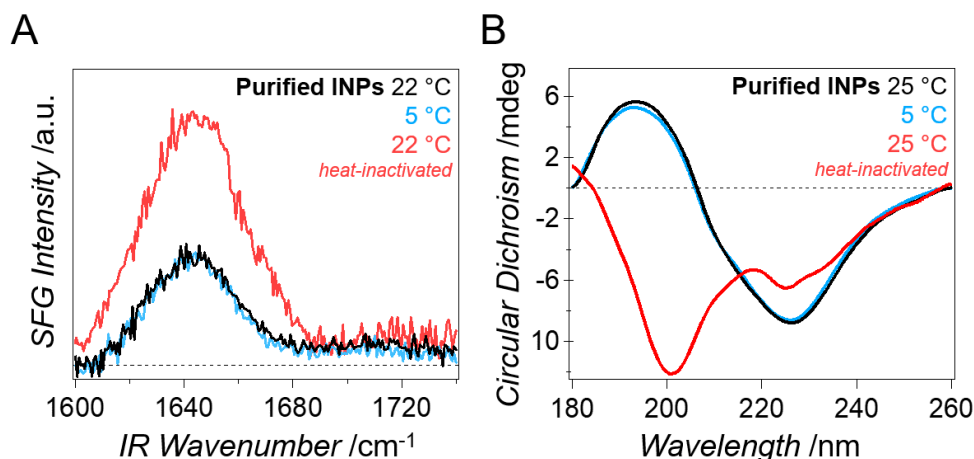

Figure 6.3: Amide I SFG and CD spectra of purified INPs derived from *P. syringae* - (A) SFG spectra of purified INPs in D2O, measured in the Amide I region. The spectra of the active INPs at 22 °C and 5 °C look similar, with signals at ~ 1640 and $1710\,\mathrm{cm}^{-1}$. The heat-inactivated INPs (red), show a considerably increased signal at $\sim 1640\,\mathrm{cm}^{-1}$. (B) CD spectra of purified INPs in water at 25 °C and 5 °C, as well as at 25 °C after heat-inactivation (red). Dashed lines indicate zero in both panels.

The CD spectrum of the purified INPs (Figure 6.4 A) looks unusual and its decomposition using the structural database does not allow a clear distinction into the common secondary structures of α-helix, β-turn, β-strand or random coil.[217] The spectral shape, however, shows similarities with those of AFPs derived from *Marinomonas primoryensis* (*Mp*AFP) and *Rhagium inquisitor* (*Ri*AFP) (Figure 6.4 B and C), but with slightly shifted peak positions. Both AFPs have β-helical folds,[217] which is in agreement with the current theoretical model of the INP as shown in Figure 6.1 A and the inset of Figure 6.4 A.[67] The negligible changes in CD spectra at low temperatures are further consistent with temperature-dependent measurements of structurally similar β-helical AFPs.[218]
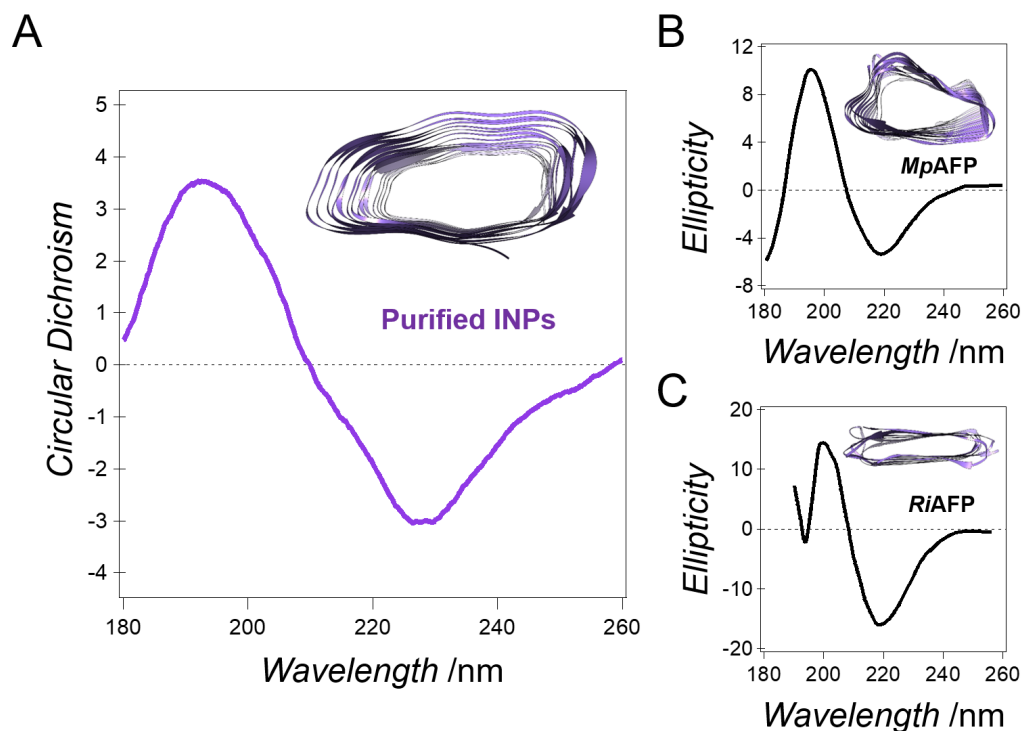
Figure 6.4: Circular dichroism spectrum of purified INPs compared to the spectra of two AFPs - A) CD spectra of purified INPs derived from fragmented *P. syringae* at 25 °C in water [circular dichroism (mdeg)]. B) CD spectrum of an AFP derived from *Marinomonas primoryensis* (*Mp*AFP) [ellipticity (mdeg)]. Data obtained from Garnham et al.[219] C) CD spectrum of an AFP derived from *Rhagium inquisitor* (*Ri*AFP) [mean residue ellipticity (deg cm^{-2}/dmol $\times 10^{-3}$)]. Data obtained from Hakim *et al.*[60] Dashed lines indicate zero in all panels. The insets show cross-sections of the proteins with the β-sheets highlighted in purple.

6.4 Conclusions

In summary, we purified INPs from *P. syringae* using ice affinity methods and report experimental evidence that the purified INPs are ice nucleation active, and that they adopt defined solution structures, which show resemblance with β-helical AFP spectra.[217] We further show that enhanced interfacial water ordering at temperatures close to the melting point of ice is not only found for active, but also for completely inactivated INPs. While protein-induced enhanced interfacial water ordering likely constitutes an essential part of INPs' working mechanism, our results reveal that increased water ordering observed with SFG spectroscopy is, by itself, not a sufficient condition for INP

activity. Instead, our results highlight that the intact three-dimensional fold is essential for the ice nucleation activity of INPs. This observation, combined with the similarity of the protein structure of the INPs from *P. syringae* and other ice-binding proteins, suggests that supramolecular interactions and ordering are key to the exceptional ice nucleation activity of bacterial INPs.[67] We hypothesize that the completely intact native structure of the INP is required for the formation of the functional aggregates that allow the formation of ice nuclei or embryos large enough to enable freezing at $-2\,°C$ ($\sim 104\,kDa$).[2,73,207] Specifically, if the observed water ordering effect plays a role in bacterial ice nucleation, we can surmise that some secondary structures of the INPs remain at least partially intact, inducing a similar degree of order. However, the breakdown of higher-order structures (tertiary, quaternary) leads to the loss of the collective alignment of INP units that explains the substantial loss in effectiveness.[73] This hypothesis would predict a freezing behavior of the inactivated INPs comparable to structurally similar antifreeze proteins and will be tested in future studies.

6.5   Supporting Information

- Details on sample preparation and experimental methods
- Ice Affinity Purification
- Heat Treatment
- INP model

Ice Affinity Purification   Falling water ice-affinity purification and rotary ice-shell purification were used to purify the INPs of the bacteria *P. syringae*. Details of the purification method have been described elsewhere.[203,204] We purified fragmented *P. syringae* cells obtained as the commercial product Snomax®. For falling water ice-affinity purification, a commercially available ice-making machine (K20, Whirlpool, USA) was used to pump an aqueous Snomax® solution (750 mg in 2.5 L H_2O) to the top of a metal plate. As the temperature of the metal plate is cooled down to subzero temperatures, nucleation occurs. The constant *P. syringae* solution circulation leads to the adsorption of the weakly ice-binding INPs to the ice surface. During the purification, $\sim 30\%$ of the solution gradually froze. The obtained ice was melted and freeze-dried to obtain a mixture of all present INPs from *P. syringae*. The large size of the INPs, the presence of protein-associated lipids and the tendency of aggregation and formation of assemblies makes the quantification of the purification challenging. We first assessed the success of the INP purification by determining the ice nucleation activity of the purified INP samples using TINA measurements. We further performed gel electrophoresis experiments to track the removal of impurities of the purified solution. Supporting Figure 6.5 B shows that at similar mass concentrations, the purified and ice active INP samples do not show several of the protein bands that were found for the fragmented *P. syringae* cells. We also do not expect a strong singular bond of an INP in the gel since *P. syringae* produces variants of INPs which can have many different sizes. Moreover, Coomassie blue has been shown to only weakly bind to a protein with a similar structure and amino acid composition.[191] For the preparation of our INP samples, we chose the more efficient falling water ice-affinity purification to obtain the needed large amounts of lyophilized INP samples for SFG and TINA experiments. We further compared the results of the falling water ice-affinity purification with results obtained from rotary ice-shell purification.[204] Here, in a 500 mL flask, 20–30 mL water was used

to form an ice shell using a dry ice-ethanol bath for 30--60 s. The flask was rotated in a temperature-controlled ethylene glycol bath, and the temperature of the bath was set to $-2\,°C$. 100 mL precooled Snomax® solution (0.5 mg/mL) was added, and the flask rotated continuously in the bath until 30% of the solution were frozen. The flask was removed from the motor, and the liquid phase was separated from the ice phase. The ice-phase contained INPs from *P. syringae* and was melted. The obtained solution was then used to confirm the similarity of CD spectra of INPs purified with this method and the falling water ice-affinity method.

Heat Treatment/Inactivation Heat treatments were performed to inactivate the bacterial INs. For this, a 0.1 mg/mL Snomax® solution was autoclaved at 121 °C for 20 min (Laboklav 25). The autoclaved solutions did not show any indication for lowered protein concentrations (visual observation) due to precipitation. Additionally, surface tension measurements of the untreated and heat-treated samples conducted during the Amide I SFG experiments also revealed no significant changes or indications for the formation of precipitates.

TINA Experiments Details are described in Section 2.2. All experiments were performed multiple times with independent samples, as shown in Figure 6.6.

Sum-Frequency Generation Spectroscopy The details of the experimental setup have been described in Section 2.1.1 The spectra presented in this study were simultaneously recorded in the C–H and O–D stretch (IR $\sim$ 2000–3100 cm^{-1}) or in the Amide I (IR $\sim$ 1600—1700 cm^{-1}) region. Spectra were obtained in the SSP polarization combination (S polarized SFG, S polarized VIS, P polarized IR) or in the SPS polarization combination (S polarized SFG, P polarized VIS, S polarized IR). Background spectra were taken with blocked IR and unblocked VIS beam, and all spectra were normalized to non-resonant reference spectra from z-cut quartz. The SFG measurements were performed in a custom-made, temperature controllable PTFE-coated aluminum trough. We conducted measurements at 22 °C and 5 °C. The INP and Snomax® (*P. syringae*) solutions were measured at a concentration of 0.1 mg/mL. Samples were allowed to equilibrate for at least two hours before measurements. The equilibration of the samples at the interface was complete, when the simultaneously measured surface tension

(Wilhelmy plate method, DeltaPi/Dyne Probes, Kibron Inc.) was constant and the SFG spectra did not change within one hour. Calibration of the surface tension measurements was conducted using pure D_2O (Sigma Aldrich, 99.9%) before each SFG experiment. The sample box was purged with nitrogen during the experiments. Comparison of Amide I SFG measurements in two different polarization combinations did not reveal any indication for protein reorientation on the surface.

CD spectroscopy The purified INPs were analyzed at a concentration of 0.5 mg/mL in Milli-Q® water. The sample was measured in a 350 μL quartz cuvette (Hellma Analytics) with a path length of 1 mm. Measurements were conducted using a JASCO 1500 circular dichroism spectrometer. Temperatures were controlled and maintained by a PTC-510 Peltier temperature-controlled sample holder in combination with an external cryogenic bath. Equilibration time for each sample before each set of measurements was 15 min. Spectra were background subtracted and processed using the Spectra Manager Analysis program from JASCO.

INP Model The INP model consists of a 16-amino acid ring (GYGSTQTSGSESSLTA), which was repeated 14 times, along the x-axis. The initial structure for INP was taken from Hudait *et al.* (2018).[67]
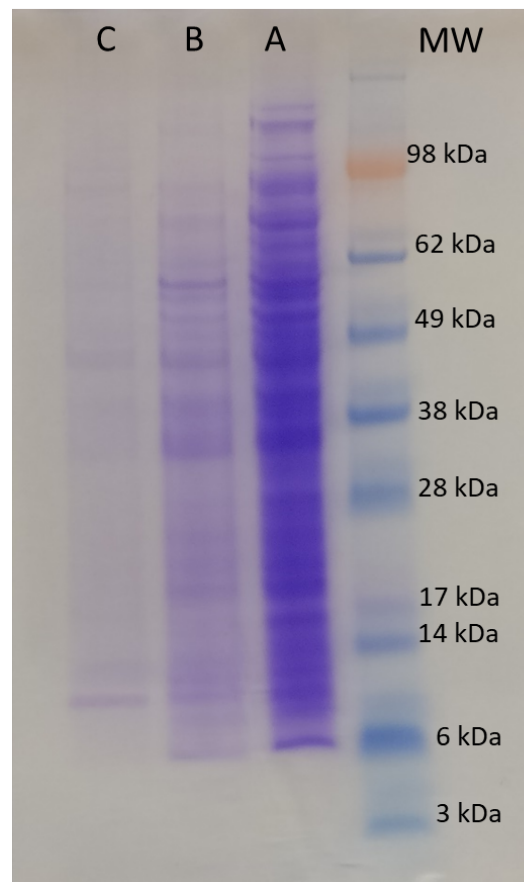
Figure 6.5: Coomassie blue-stained SDS-PAGE analysis of ice-affinity purifications of the INPs - Lanes were loaded with fractions on an equal volume basis relative to the starting material. Samples shown in each lane correspond to protein markers, original *P. syringae* culture (A) and purified sample after the first (B) and second round (C) of falling water ice-affinity purification.
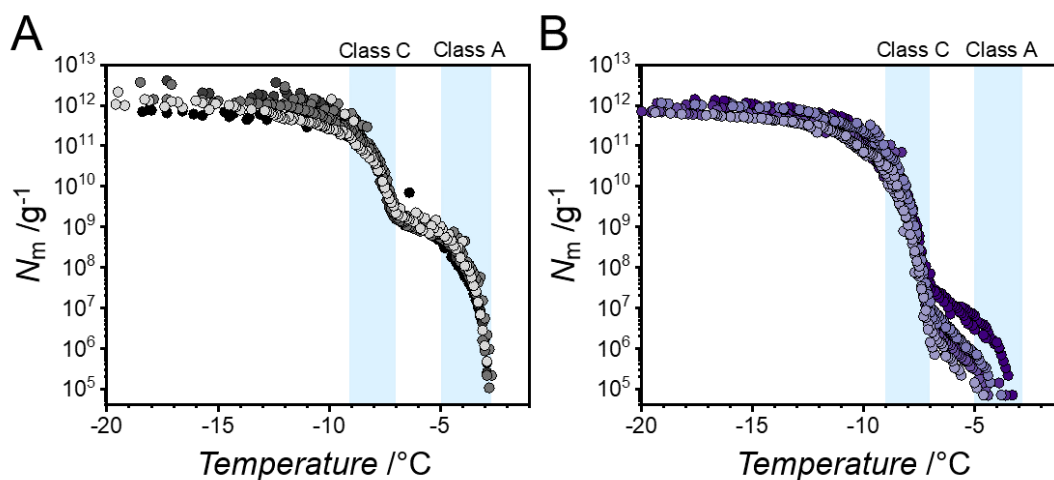
Figure 6.6: Freezing experiments of aqueous solutions of *P. syringae* (A) and purified INPs (B) - Shown are the cumulative number of active ice nucleators per unit mass of *P. syringae* vs. temperature for five independent experiments. The temperature ranges for Class A and Class C INPs are shaded in light blue.
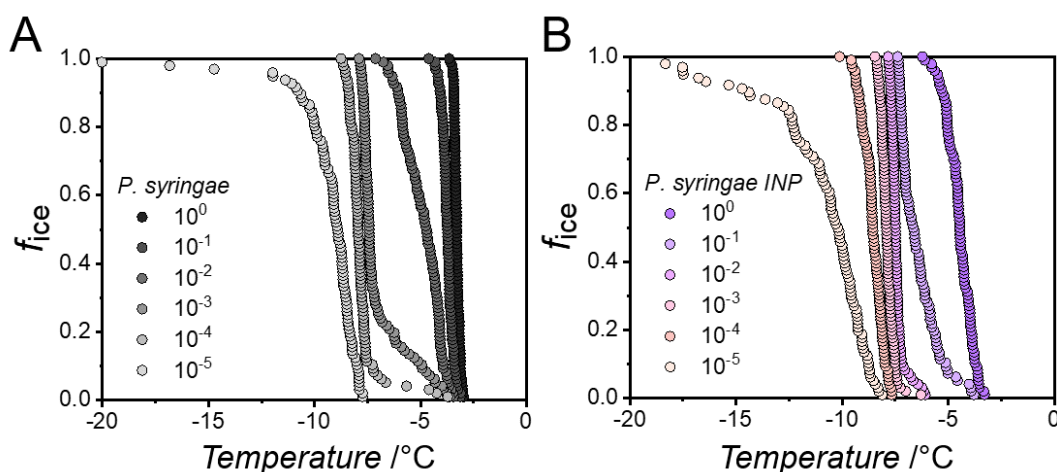
Figure 6.7: Fraction of frozen droplets for *P. syringae* and purified INP solutions corresponding to data shown in Figure 6.6 - The initial concentration of 10^{-1} mg/mL is diluted down to 10^{-6} mg/mL.

111
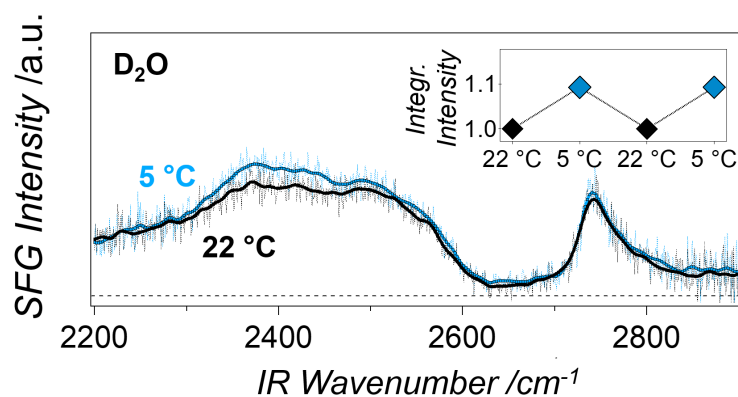
Figure 6.8: Temperature-dependent sum-frequency generation measurements of pure D$_2$O - The peak at $\sim 2720\,\text{cm}^{-1}$ stems from the free O–D stretch mode which arises from non-hydrogen-bonded deuterium atoms at the surface. The free O–D disappears upon surface coverage with sample molecules. The inset shows the integrated SFG intensities of the bonded O–D stretch frequency region ~ 2200–$2700\,\text{cm}^{-1}$ for two temperature cycles.
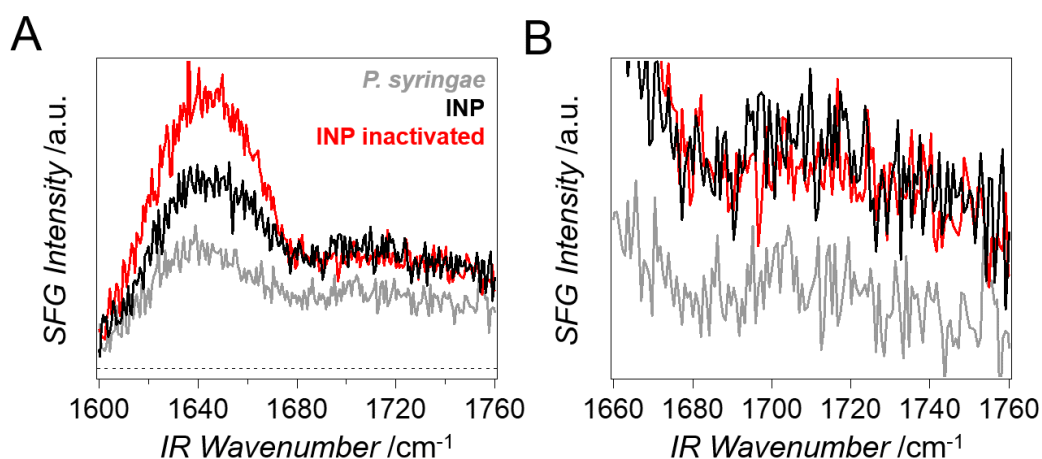

Figure 6.9: SFG spectra of bacterial ice nucleators in the Amide I region - (A) *P. syringae* (grey), purified INPs derived from *P. syringae* (black) and heat-treated INPs, all measured at room temperature in H$_2$O. The dashed line indicates zero. (B) Magnification of the carbonyl region, which reveals weak lipid signals. As a result of the purification, the protein signal of the INP samples is increased compared to that of the bacteria.

112
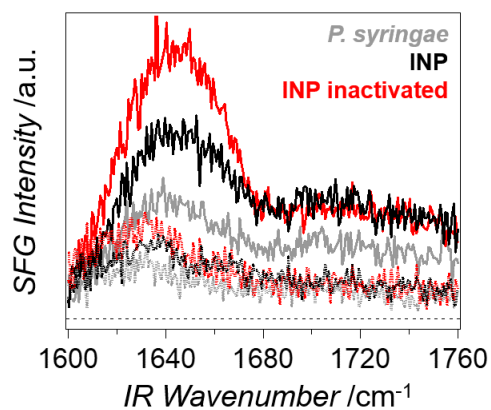
Figure 6.10: Amide I SFG spectra of Snomax® (grey) and purified INPs (black) as well as inactive INPs (red) - Measurements were performed in the SSP (solid lines) and PSP (dotted lines) polarization configuration.
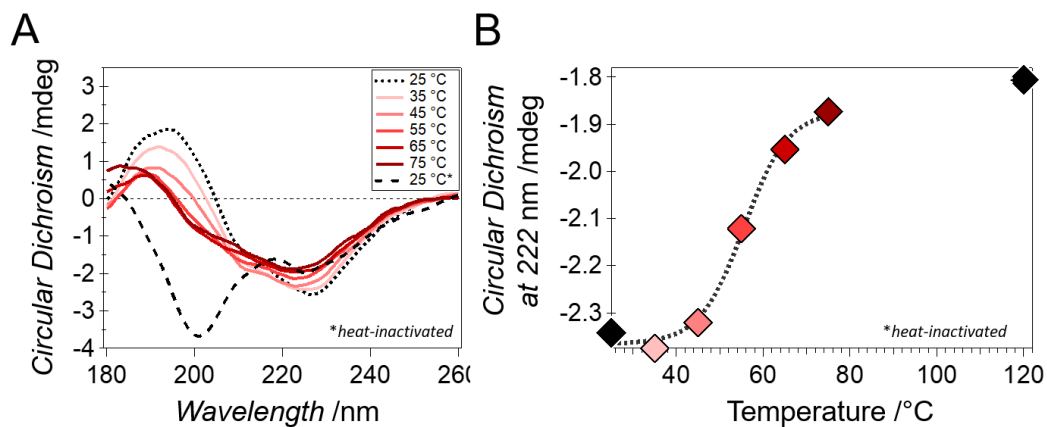
Figure 6.11: CD spectra of purified INPs and melting curve - (A) CD spectra of purified INPs derived from *P. syringae* at temperatures from 25 to 75 °C in water as well as an autoclaved sample (heated to 121 °C, measured at 25 °C), and (B) melting curve of the protein obtained from the circular dichroism values at 222 nm. The dashed line is a guide for the eye. The melting point is estimated to be at around 55 °C.
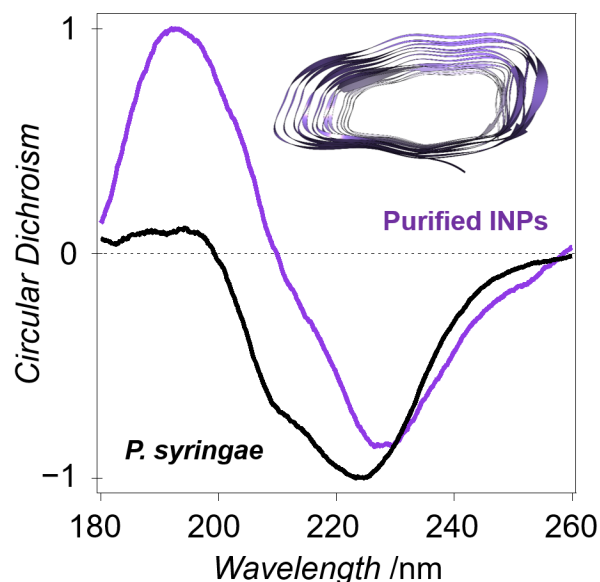
Figure 6.12: CD spectra of purified INPs and fragmented *P. syringae* (Snomax®), normalized to the highest local maximum, respectively. The inset shows the cross-section of the protein with the β-sheets highlighted in purple.
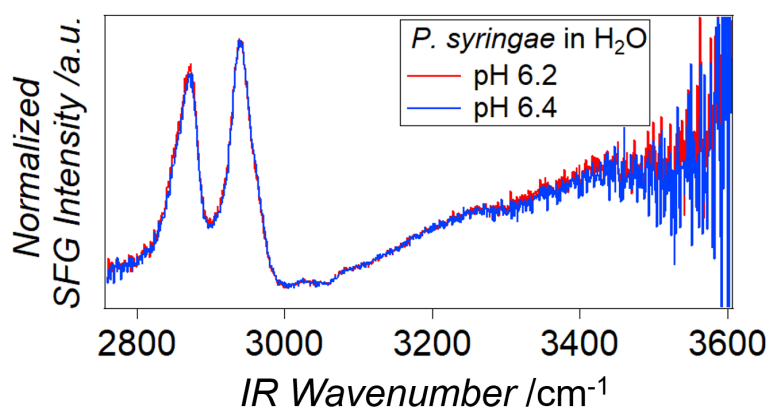
Figure 6.13: SFG spectra of *P. syringae* in PBS-buffered solutions with a pH of 6.2 and 6.4, respectively - The pH of a solution of *P. syringae* (Snomax®) in water is ~ 6.2 and increases by 0.1–0.2 when cooling down to $1\,°C$. As apparent from the identical SFG spectra for the two PBS-buffered solutions (both measured at room temperature), this change does not significantly increase the intensity. The shown spectra are the averages of the spectra of 3 samples per pH value, respectively. The figure has not been published in Lukas *et al.* (2020).[4]
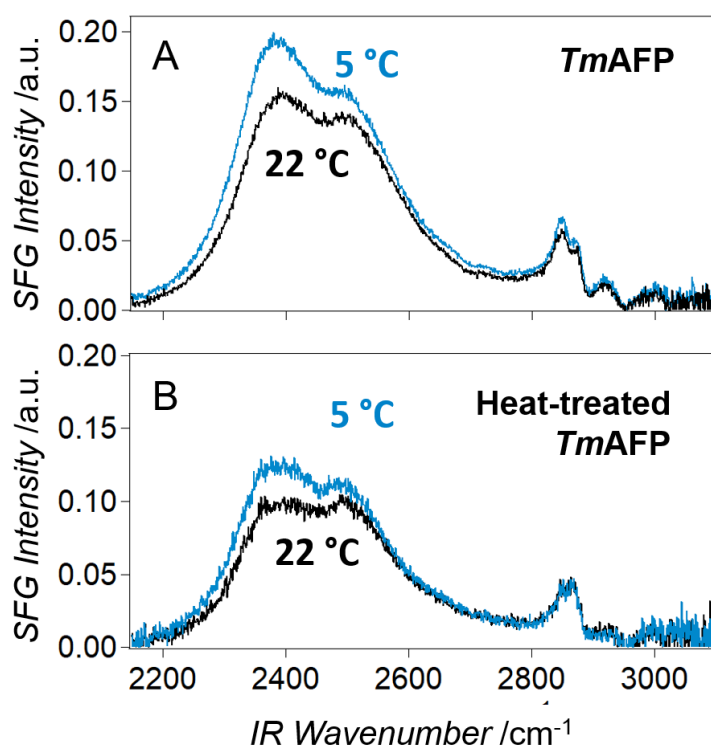
Figure 6.14: Temperature-dependent SFG spectra of purified *Tm*AFP in D₂O solution - (A) Untreated *Tm*AFP. (B) Heat-treated *Tm*AFP. The experiments were performed in different setups. The increase in the integrated O–D band intensity is around 33% in (A), and around 20% in (B). Heat-treatment causes slight changes in the C–H stretch region. The ratio of its amplitudes to those in the O–D band is increased. The experimental conditions are similar to those described for the experiments with the purified INPs. The figure has not been published in Lukas *et al.* (2020).[4]

7

Perspective: Toward Understanding Bacterial Ice Nucleation
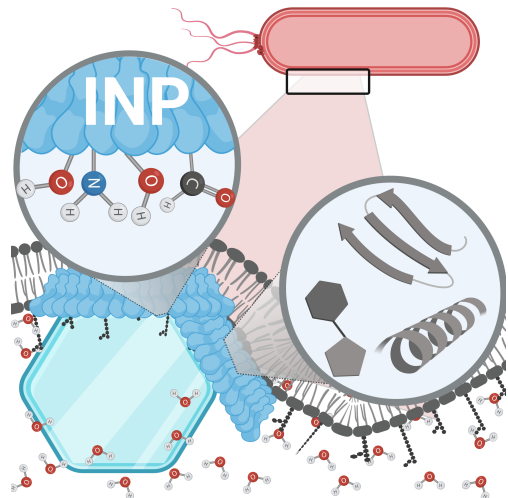
7. PERSPECTIVE: TOWARD UNDERSTANDING BACTERIAL ICE NUCLEATION

7.1 Abstract

Bacterial ice nucleators (INs) are the most effective ice nucleators known and relevant for freezing processes in agriculture, the atmosphere, and the biosphere. Their ability to facilitate ice formation is due to specialized ice nucleation proteins (INPs) anchored to the outer bacterial cell membrane and enabling the crystallization of water at temperatures up to $-2\,°C$. In this perspective, we highlight the importance of functional aggregation of INPs for the exceptionally high ice nucleation activity of bacterial INs. We emphasize that the bacterial cell membrane, as well as environmental conditions, are crucial for a precise functional INP aggregation. Interdisciplinary approaches, combining high-throughput droplet freezing assays with advanced physicochemical tools and protein biochemistry, are needed to link changes in protein structure or protein-water interactions with changes on the functional level.

7.2 Introduction

Freezing processes in the atmosphere have a significant influence on the formation of clouds, on precipitation patterns, and on Earth's energy balance.[6,7] Homogeneous ice nucleation at a given temperature requires a certain number of ice-like water molecules. The homogeneous nucleation temperature depends on droplet volume, pressure, and the water activity in the presence of potential solutes.[16] In clouds, pure water can be supercooled to temperatures as low as $-38\,°C$.[14,15] Above the homogeneous freezing point, ice crystal formation is triggered by particles that serve as heterogeneous ice nucleators (INs). Numerous INs have been identified and their ice nucleation efficiencies are typically characterized using droplet freezing assays.[14,27,42,220,221] In such assays, a large number of droplets containing a well-defined concentration of IN agents is gradually cooled down and the fraction of frozen droplets as a function of temperature is recorded. The temperature at which half of the droplets are frozen, T_{50}, provides a direct measure for the efficacy of the IN agent. While mineral dust-based INs (e.g., feldspars, silicates, clay minerals) play a major role in the atmosphere owing to their ubiquity, the ice nucleation efficiency of biological INs derived from bacteria, fungi, lichen or plants is much higher.[14] Despite its significance and the acceleration of research in this area in the last years, several questions on the details of the molecular-level

mechanisms of heterogeneous ice nucleation remain unanswered. This makes it difficult to predict the decisive properties of efficient INs and their role in the environment. Understanding such molecular-level mechanisms could point to novel ways of triggering ice nucleation, desirable for artificial snow, for instance, but also to new artificial anti-icing surfaces.[222,223,224]

Ice-nucleation activity in bacteria was first discovered in Pseudomonas in the 1970's.[36,37] Subsequently, several other ice-nucleating bacteria belonging to species in the *Pseudomonadaceae*, *Enterobacteriaceae*, *Xanthomonadaceae*, and *Lysinibacillus* families have been identified.[38,39,40] The best-characterized bacterial INs are from *Pseudomonas syringae* which enable ice nucleation at temperatures up to $-2\,°C$. The ability of bacteria to facilitate ice formation is attributed to specialized proteins anchored to the outer bacterial cell membrane. As a plant pathogen, *P. syringae* causes frost injury to the plant tissue by increasing the nucleation temperature of water, which enables access to nutrients.[42] Moreover, like many other ice-nucleating microbes, *P. syringae* was identified in ice, hail, and snow, indicating that they might contribute to freezing processes in the atmosphere.[169,225] The unique standing of *P. syringae* as a source of exceptional bacterial INs is further emphasized by its commercialization as Snomax®. This artificial snow-making product consists of extracts of sterilized *P. syringae*.

The biomolecules responsible for bacterial ice nucleation are large ice nucleation proteins (INPs) anchored to the outer membranes of the bacterial cells, as schematically shown in Figure 7.1. The principal function of the INPs is to order water molecules into an "ice-like" arrangement, thereby facilitating the kinetically hindered phase transition.[11,53,54,60,62,63,226]

The amino acid sequence of the INPs of *P. syringae* has been deduced and is widely used to model its structure as shown in Figure 7.1.[11,49,227,228] The INP consists of three domains: (1) a central repeating domain (CRD) comprising of $\sim 81\%$ of the total sequence, (2) an N-terminal domain comprising of $\sim 15\%$ of the sequence, and (3) a C-terminal unique domain ($\sim 4\%$). The CRD has been proposed to contain the ice nucleation site of the INPs and molecular simulations have shown that the active site consists of similarly effective TxT and ExSxT amino acid motifs.[67]

The large size and embedment into the membrane still hamper experimental attempts to solve the three-dimensional structure and associated molecular-level details of the INPs. In contrast, the structures of antifreeze proteins (AFPs) containing similar TxT

7. PERSPECTIVE:
TOWARD UNDERSTANDING BACTERIAL ICE NUCLEATION
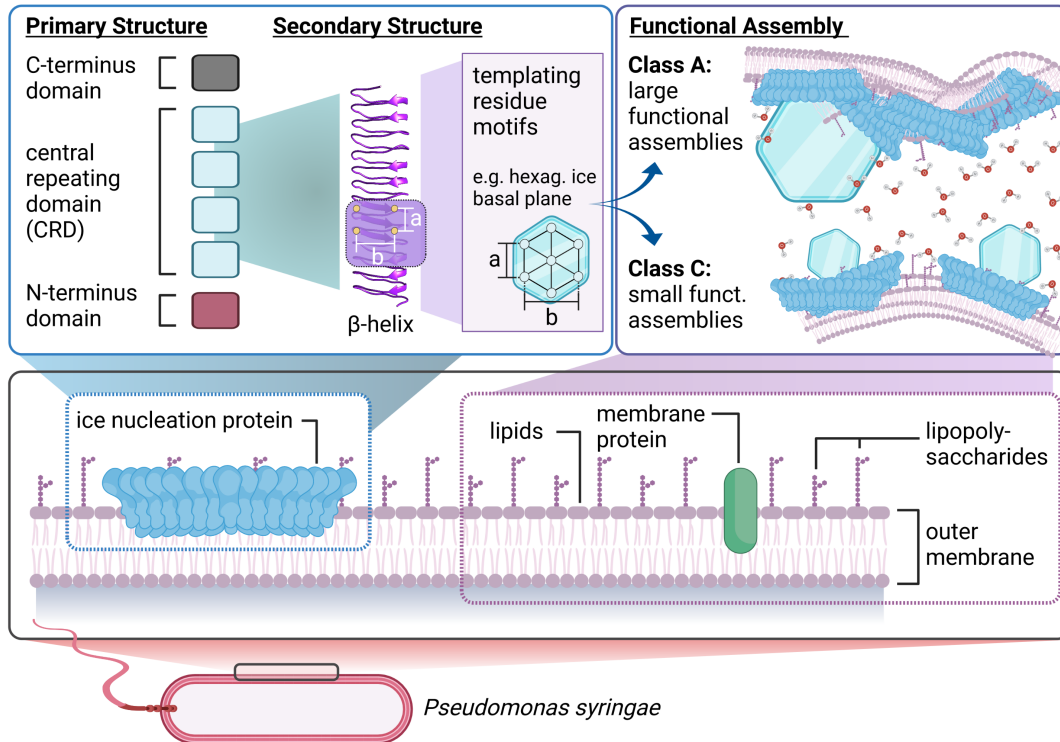
Figure 7.1: Overview of the proposed structure and working mechanism of bacterial ice nucleation proteins anchored to the outer cell membrane of *P. syringae* - The INP consists of an N-terminal, a C-terminal, and a central repeating domain. Its general function is to order water molecules into an "ice-like" arrangement to nucleate ice formation. This process is facilitated when INPs assemble into larger aggregates.

motifs have been solved, oftentimes revealing β-solenoid folds.[51,53,54] A β-helical motif has also been used to model the structure of bacterial INPs,[61] based on the idea that AFPs and INPs share similar folds and ice-binding motifs.[65,67,226]

A central enigma of bacterial ice nucleation arises from the broad distribution of threshold nucleation temperatures ranging from $-2\,°\mathrm{C}$ to $-12\,°\mathrm{C}$. This is reflected in freezing assays that show not one single T_{50}, but a wider range of nucleation temperatures. Based on extensive freezing assays of *P. syringae* for different concentrations, three distinct classes of INs have been proposed.[26,69].

Govindarajan and Lindow showed that the largest structures of INs reach the highest threshold temperature, i.e., nucleate ice most efficiently.[47] Southworth *et al.* revealed a nonlinear relationship between ice nucleation activity and the concentration of INP in bacterial cells.[71] Together, those findings indicate that the different activation

temperatures can be explained by aggregation of INPs, thereby varying the accumulated size of the ice nucleation site. Simulations have addressed the role of size and aggregation of the proteins on the freezing temperature and provided quantitative prediction of the ice nucleation temperature vs. the number of proteins in the aggregates, as well as to the distance between the monomers in the aggregates.[73] The predominant and least efficient fraction of bacterial INs active at $\sim -7\,°C$, Class C, has been attributed to small aggregates of INPs. The most active Class A INs are active at temperatures up to $\sim -2\,°C$ and consist of the largest aggregates of the INPs. Class B INs are rarely observed and responsible for freezing between $\sim -5\,°C$ and $\sim -7\,°C$. Aggregation of the INPs in the cell membrane was described in several studies and it has further been suggested that the membrane plays a major role in enabling the highly active Class A INs.[41,71,72]

7.3   Experimental Approach

Progress in unraveling the mechanism underlying bacterial ice nucleation requires advanced physicochemical methods and interdisciplinary approaches. Essential for any investigation of INs are droplet freezing assays. High-throughput assays, like the Twin-plate ice nucleation assay (TINA), now enable the simultaneous measurement of complete dilution series (typically $0.1\,mg/mL$ to $1\,ng/mL$) with high statistics, enabling the cumulative representation of the complete range of present INs.[45] Observations at the functional level can be accompanied by molecular-scale investigations using spectroscopic tools. Circular dichroism and infrared spectroscopy provide information on the secondary structure, while surface-specific vibrational sum-frequency generation spectroscopy (SFG) is a powerful tool to investigate the molecular-level details of the interface of bacterial INPs and water.[2,3,4,159,229] The biophysical and spectroscopic investigations are further highly dependent on sample quality. Recent progress in ice-affinity purification methods now allows for isolating ice-binding proteins directly from natural sources and with high purity.[4,191,203] In the here presented studies, we utilized inactivated extracts from *P. syringae*, commercially available under the product name Snomax® (Snomax Int.).

7.4 Results
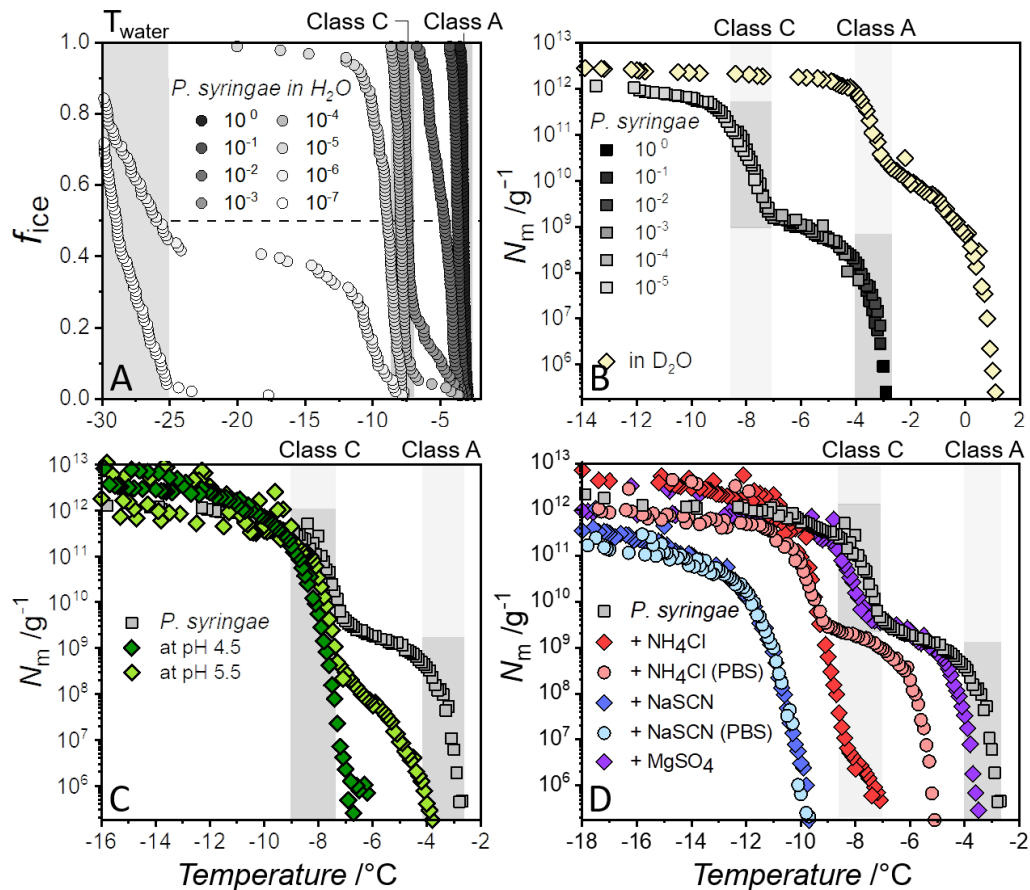
Figure 7.2: Freezing spectra of aqueous solutions of Snomax® containing bacterial ice nucleators from *P. syringae* - (A) Fraction of frozen droplets (f_{ice}) vs. temperature for the dilution series of a *P. syringae* IN measurement in pure water. (B) Cumulative freezing spectra of *P. syringae* INs in pure H_2O and D_2O, respectively. (C) Freezing spectra of *P. syringae* INs at pH 6.2 (grey), pH 5.5 (light green) and pH 4.5 (dark green).[2] (D) Freezing spectra of *P. syringae* INs in pure water and in the presence of 0.5 mol/kg NH_4Cl (red), NaSCN (blue), and $MgSO_4$ (purple) in water, and of NaSCN (light blue) and NH_4Cl (light red) in PBS buffer.[3] The temperature ranges of Class A and Class C are highlighted in grey and correspond to measurements of *P. syringae* in pure water only.

Figure 7.2 shows freezing spectra of bacterial ice nucleators from *P. syringae* under different environmental conditions. All cumulative freezing spectra are composed of measurements of a 10-fold dilution series. The fraction of frozen droplets (f_{ice}) measurements shown in Figure 7.2 A correspond to the spectra of *P. syringae* INs in pure water (grey curves) in the Figures 7.2 B. The cumulative IN concentration (N_m)

is calculated using Vali's equation,[129] and represents the number of ice nucleators per unit weight that are active above a certain temperature. The two strong increases at $\sim -3\,°C$ and $\sim -7.5\,°C$ correspond to the large aggregates (Class A INs) and the smaller aggregates (Class C INs), respectively. The two increases are followed by plateaus, which indicate that fewer INs are active in those temperature ranges.[28]

Figure 7.2 B shows the results of ice nucleation measurements of the bacterial INs in deuterated water (D_2O) as well. The freezing spectrum is shifted $\sim +4\,°C$, which is consistent with the expected shift of $\sim +3.82\,°C$ based on the higher melting point of D_2O compared to H_2O. Turner *et al.* previously described a third intermediate Class B of INs, active at around $-5\,°C$, and that examining the effects of substituting D_2O for H_2O allows for differentiation of the different classes on the basis of their isotope-induced shifts in nucleation threshold.[26] As apparent from Figure 7.2 B, the freezing spectra do not show an additional increase assignable to a third class of INs. However, differences in the freezing curves of *P. syringae* INs in H_2O and D_2O do occur. Measurements in D_2O show a larger number of Class A INs and fewer Class C INs. The differences can tentatively be explained by fewer structural fluctuations and the preferred formation of INP aggregates due to stronger intramolecular D-bonds.[70]

Several studies have reported that pH changes of the aqueous solution or the addition of co-solutes affect the Class A INs differently than Class C.[26,69] Figure 7.2 C shows cumulative freezing curves of *P. syringae* INs as a function of pH (Chapter 4).[2] Upon lowering the solution pH, the first rise at $\sim -3\,°C$ (Class A) gradually decreases and shifts to lower temperatures while the fraction of INs active at $\sim -7.5\,°C$ (Class C) increases. There seems to be a clear interconversion of Class A species into Class C species with decreasing pH. At a pH of ~ 4.5, we observe that only Class C INs remain active.

By using surface-specific SFG vibrational spectroscopy as a tool for the determination of the isoelectric point of the bacterial extract, a possible explanation for this puzzling disappearance of Class A aggregates could be obtained. In SFG spectroscopy, a broadband infrared (IR) beam is used to probe the molecular vibrations in a given frequency region (Figure 7.3 A). The IR beam is combined with a visible beam (VIS) at the sample surface to generate light of the sum-frequency of the two incident fields. This second-order nonlinear process is bulk-forbidden in isotropic media and only ensembles of molecules with a net orientation, e.g., at an interface, generate a detectable signal.

7. PERSPECTIVE:
TOWARD UNDERSTANDING BACTERIAL ICE NUCLEATION

The SFG signal intensity in the O–H stretch region increases with the alignment of the water molecules' dipoles, as, e.g., induced by the net charge of a protein film on the surface (Figure 7.3 A). Consequently, SFG can be used to determine the isoelectric points (IEPs) of proteins by monitoring the O–H stretch signal (Figure 7.3 B).[144,145,146,167]

The IEP of the *P. syringae* extract determined with SFG was found to be ~ 4.2 (Figure 4.3 in Section 4.3), which coincides with the pH at which the Class A INs are completely absent. Apparently, the repulsive forces caused by the net negative charge of the INPs are crucial for the precise alignment of the functional Class A aggregates, which rely on sub-Ångström control over the distances of the single INPs active sites.[11,73,160]
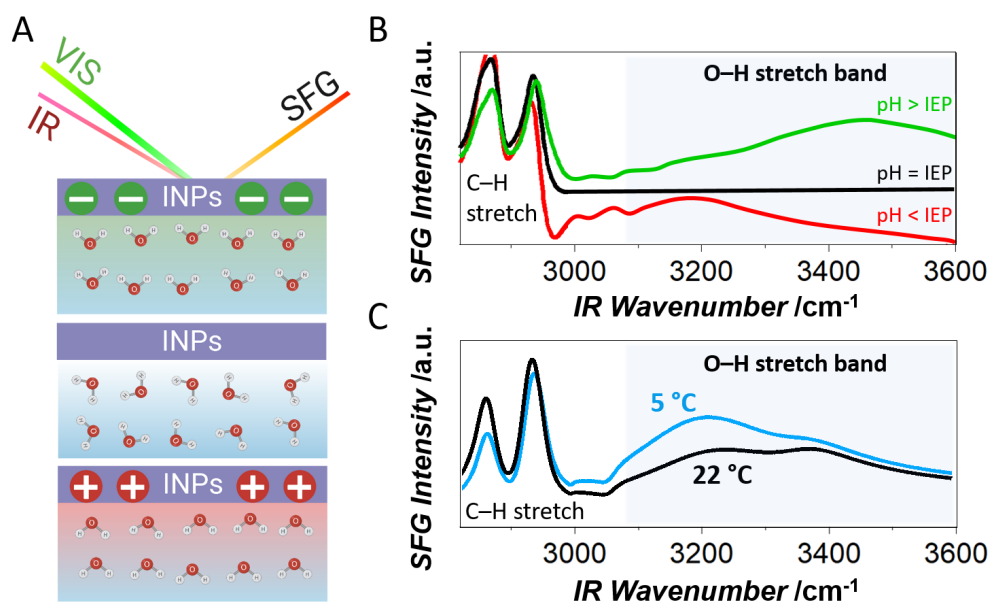
Figure 7.3: Sum-frequency generation (SFG) spectroscopy of bacterial INPs at the surface of aqueous solutions - (A) The incident IR and VIS beams generate a surface-specific SFG signal from the vibrational resonances. The illustration shows the alignment of interfacial water molecules in case of a negative net charge as found at the natural pH of ~ 6.2, in case of zero net charge at the isoelectric point IEP ~ 4.2, and the opposite alignment in case of a positive net charge at pH values below the IEP. (B) Corresponding SFG spectra (stacked): The O–H band intensity is close to zero at the IEP and increases with charge-induced alignment of the water molecules.[2] The flip of the molecules' orientations causes a frequency shift of the O–H stretch band.[96] (C) Temperature-dependent SFG spectra of the O–H stretch band of interfacial H$_2$O molecules and the C–H stretch vibrations. The intensity of the O–H stretch band, and therefore the interfacial water alignment, is significantly higher at low temperatures.[4]

A combination of TINA and SFG experiments further revealed ion-specific effects on *P. syringae* INs that follow the Hofmeister series (Chapter 5).[3] Figure 7.2 D shows bacterial freezing spectra in the presence of different salts. NaCl was found not to affect the bacterial freezing spectrum except a shift of around $-2\,°C$ caused by colligative melting point depression. In contrast, freezing spectra of bacterial solutions containing NH_4Cl, $MgSO_4$, and NaSCN, show ion-specific effects. NH_4Cl causes the first rise at $-3\,°C$ to shift to $\sim-7.5\,°C$, close to the second rise, now found at $\sim-9\,°C$. Interestingly, when comparing freezing spectra of buffered and unbuffered solutions containing NH_4Cl, this effect is solely explainable by salt-induced solution pH changes (Section 5.4 and Figure 5.10). In the presence of NaSCN, only a single increase at $\sim 11.5\,°C$ remains, indicating a complete loss of Class A and a partial inhibition of Class C INs. The effect is similar for the buffered solution, excluding a pH effect. In the presence of $MgSO_4$, no inhibition is observed. In fact, after correcting for the colligative freezing point depression, the freezing curve is shifted to warmer temperatures, suggesting enhanced ice nucleation efficiency. Comprehensive experiments with sixteen salts showed that their effects on the INP-mediated freezing temperatures follow the trend of the anions in the Hofmeister series. Weakly hydrated ions, such as thiocyanate, lower the threshold temperatures while more strongly hydrated ions, such as sulfate, have no effect or can apparently facilitate ice nucleation.

SFG experiments revealed that although the ionic strengths and counter ions are identical, the salts have different efficiencies in screening the net charge of the bacteria (Figure 5.3 in Section 5.3). Weakly hydrated anions decrease the SFG intensity less than strongly hydrated ions. Supported by MD simulations (Figure 5.4), we explained these results in terms of two effects: Compared to strongly hydrated anions, the weakly hydrated anions preferentially adsorb to the bacterial surfaces, which would render the bacterial surfaces more negative and increase the order of the interfacial water molecules. Additionally, the ions might induce changes in the INP conformation and thereby affect the charge distribution.

The high sensitivity of SFG to the ordering of interfacial water molecules raises the question of whether specific ice-like ordering of water in contact with INPs can be observed close to their biologically relevant working temperature. Pandey *et al.* reported SFG experiments of *P. syringae* extract (Snomax®) in D_2O at room temperature and $1\,°C$ above the melting point and showed that the SFG signal in the O–D stretch region

is increased and red-shifted at low temperature, indicating an increase in the alignment of the water molecules.[159] Shortened INPs with low IN activity expressed in *E. coli* showed a similar effect and the observation was attributed to an activation of INPs at lower temperature and the ability to order water which increases close to the respective freezing temperature.[229]

While providing much needed experimental insights into the INP/water interface, these studies and interpretations must be taken with a caveat, given that more recently, it has been shown that water ordering at lower temperatures observed with SFG (Figure 7.3 C) is identical for active INPs and INPs that completely lost their ice nucleation activity due to heat denaturation (Chapter 6, Figure 6.2).[4] Hence, making a connection between increased O–H/O–D signals in SFG and ice nucleation activity, or even the presence of ice-templating sites on the adjacent water molecules, must be performed with care.

7.5 Conclusions

From our recent studies, we can conclude that the outstanding ice nucleation efficiency of bacteria can only be understood when studying the natural, functional aggregation of the protein. It is evident that a membrane-associated mechanism is responsible for the formation of large Class A aggregates, which are responsible for the exceptionally high freezing temperatures ($\sim -2\,°C$) close to water's melting temperature. The process of bacterial ice nucleation at warm temperatures requires an appropriate pH value and intact INP structures (Chapters 4 and 6).[2,4] Moreover, the activity of both classes of bacterial INs is strongly influenced by specific interactions with ions (Chapter 5).[3] These interactions are highly relevant to correctly predict the ice nucleation efficiency of bacterial INs under natural conditions (e.g., in the atmosphere).

The important role of functional aggregation is further underlined by simulation studies, which have shown that not only Class A, but also the smaller Class C INs, active at around $-7.5\,°C$, are a product of functional aggregation of the proteins and merging of their active sites.[73] Our studies of purified INPs from *P. syringae* underlined the importance of the membrane for the formation of Class A aggregates (Chapter 6, Figure 6.1),[4] emphasizing its essential role for the ice nucleation activity. We hypothesize that the formation of Class C aggregates might have another molecular mechanism

than the membrane-associated mechanism responsible for forming the larger Class A aggregates. Clarification of whether the membrane's role lies merely in providing a matrix or whether it is part of the active ice nucleation site is another critical step for unraveling the molecular origin of bacterial ice nucleation. In addition to unsolved questions regarding the 3D structure of the INP monomer and the interfacial structure of water at the functional site of the INP, information on the precise numbers of INPs in the aggregates, their alignment, and which interactions drive the aggregation are needed (Figure 7.4). Understanding the molecular-level processes driving bacterial ice nucleation may provide further insights into the role of biological INs in the environment. Answering these questions will likely also enable the community to unravel how nature precisely aligns INPs to be the most efficient ice nucleators known and illuminate how this strategy can be copied for new freezing products and technologies.
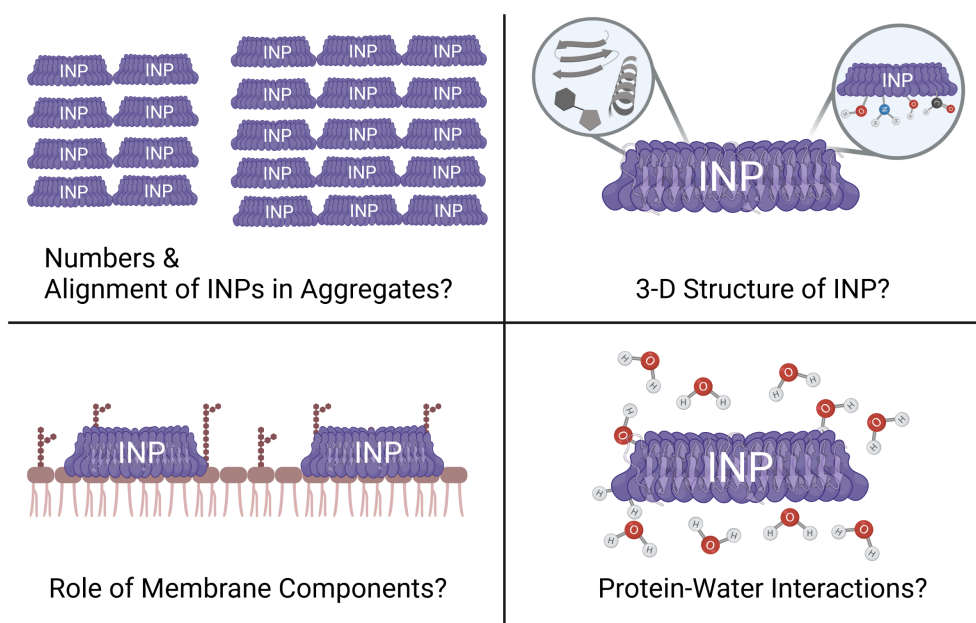
Figure 7.4: Overview of open questions towards understanding the molecular-level mechanisms of bacterial ice nucleation

8

Conclusions & Outlook

The main conclusions of our studies of bacterial ice nucleation proteins (INPs) from *Pseudomonas syringae* have been summarized and discussed in the previous chapter. This additional conclusion chapter supplements the implications from Chapter 7 for future studies, by stressing another aspect: The role of sum-frequency generation (SFG) spectroscopy for studies of bacterial INPs.

In this work, we investigated INPs from the plant-pathogenic bacterium *P. syringae*, one of the most efficient, atmospheric relevant ice nucleators (INs) known. As discussed in Section 1.2, the consensus sequences of bacterial INPs, including the repetitive sequences of the ice nucleation sites that order water into an ice-like structure, have been deduced; however, the membrane-integration of the INPs hampers investigations of their three-dimensional structure and hence the understanding of their working mechanism. Promising models have suggested a beta-helical fold as found for antifreeze proteins (AFPs). Besides the water interaction of the ice nucleation-active amino acid motifs there is another central aspect of bacterial ice nucleation: The functional aggregation of the INPs. The outstanding ice nucleation efficiency at $-2\,°\mathrm{C}$ is only reached by the largest assemblies of INPs.

Our approach to unravel the mechanism of bacterial ice nucleation was primarily based on a combination of interface-specific sum-frequency generation vibrational spectroscopy (SFG, Section 2.1.2) and high-throughput droplet freezing assays (TINA, Section 2.2). Thereby, we were able to link molecular-level information on the interaction between the INPs and water to effects on the functional level. Applying ice-affinity pu-

rification methods on the INPs, we could further obtain information on the temperature dependence of their secondary structure using circular dichroism (CD, Section 2.3) and SFG in the Amide I region (Figure 6.3 in Section 6.3).

As confirmed in the Chapters 4 and 5, the functional INP aggregation depends largely on the solution pH. Since mostly the largest INs (the largest INP aggregates) are affected, this effect had in the past been discussed as an indicator for chemical heterogeneity of the INs present in the freezing spectrum of the bacteria (Section 1.2).[11,26,50] The SFG signal in the O–H stretch region is very sensitive to the net charge of applied protein films, due to the charge-induced alignment of the interfacial water molecules (Figure 2.2, Section 2.1.2).[144,145,146,167] The determination of the INP's isoelectric point with SFG revealed new insight in the underlying mechanism of the pH dependence: In the absence of the natural net charge, and therefore of a strong source of electrostatic forces, the functional aggregation ceases to exist in the freezing spectrum. This is in line with another important assumption on INP aggregation, which is that any assembly of ice nucleation sites of the INPs has to rely on a highly accurate and precise ($\sim$ Ångström) alignment (Section 1.2).[73,160] In addition, again utilizing the sensitivity of SFG to the charge state of the INP layer on the water surface, we could show that ice nucleation activity of the INPs is influenced by the addition of salts in an ion-specific manner, following the Hofmeister series of ions (Chapter 5). Both findings are highly relevant for predictions of bacterial ice nucleation efficiency under natural conditions, for instance, in the atmosphere, or as a plant pathogen in agriculture.

In a previous study, SFG had revealed an increased alignment of water in contact with INPs when the solution is cooled from room temperature down to the melting point.[159] This was supported by MD simulations and gave an indication, that SFG might not only be sensitive to charge-induced, but also to alignment caused by the presence of the ice nucleation sites. Disentangling these two effects, by excluding any effect of pH change over temperature and by comparing the temperature-dependent ordering of INPs with that of other proteins, is challenging. In Chapter 6, we initiated the discussion of that issue by showing that the temperature effect on water ordering is similar to heat-treated, ice-inactive INPs, which exhibited a significantly changed secondary structure. Moreover, we could exclude that the effect stems from the slight pH change over temperature, as evident from Figure 6.13, added to the Supporting Information of Chapter 6.

While the possibility persists that water ordering at low temperatures as observed with SFG is unspecific for INPs, or generally for ice nucleation activity, an interesting discussion emerges from the opposite assumption. Originally, the Class C INs in the freezing spectrum of the bacteria had been attributed to single, "monomeric" INPs. Recent studies have indicated that also these less efficient INs must be the product of an assembly of the ice nucleation sites.[73,208] In Chapter 7, we surmise that the difference between the assembly mechanisms of the two classes could be rather found in the underlying steering mechanism. For instance, we found that the functional aggregation forming the highly efficient Class A INs, as opposed to Class C, largely depends on interaction with the bacterial membrane.[4,70] Based on the predictions of simulations,[73] however, we can assume that the demand for highly accurate alignment also applies to the hypothetical Class C assembly. Therefore, any structural change of the protein, as observed in Chapter 6, likely disables Class C ice nucleation, just by disturbing this alignment mechanism. Simulations predict that a single INP, independent of the length of its ice-binding site, cannot trigger ice nucleation at temperatures higher than $\sim -24\,°\mathrm{C}$,[73] which is close to the limit of temperatures observable with TINA (freezing of pure water occurs at $\sim -28\,°\mathrm{C}$). These aspects taken together, it cannot be excluded that the alignment of water molecules observed with SFG at low temperatures is similar for active and heat-inactivated bacteria and caused by the persisting ability of the functional motifs to align water.

At this point, the SFG-specific discussion stopped in the previous chapters. But how could one solve the open questions regarding the use of SFG for studies of INPs, or, inferred from this, for other ice-nucleating or even for all kinds of ice-binding biomolecules? Is it only a tool, enabling to observe the ice nucleation-unspecific alignment of water molecules induced by the strong net charge of the INPs, or do ice-nucleating sites induce a measurable increase in the water SFG signal?

We performed the temperature-dependent SFG experiments in the O–H/O–D stretch region from Chapter 6 with further proteins in H_2O/D_2O to find some first indication on how INP-specific the observed effect is. In the case of TmAFP (an antifreeze protein from mealworms, *Tenebrio molitor*), we find a remarkably similar increase of the O–D stretch band intensity ($\sim 33\%$) upon cooling (Figure 6.14 added to Section 6.5). In these initial experiments, the effect was reduced (to $\sim 20\%$) but remained after heat treatment. The structure and protein-water interactions of TmAFP have been used

to model the INP of *P. syringae* in MD simulations.[67,202] This similarity is hence in line with the hypothesis outlined in Section 1.2, that INPs and hyperactive insect AFPs have substantially similar active sites.

We investigated benchmark proteins with known structures (lysozyme, bovine serum albumin (BSA), and hydrophobin) in the same way, and find that all three possibilities can occur when lowering the temperature, SFG intensity increase, decrease and no change. Moreover, the results indicate and that heat-treatment can change this behavior for the respective protein. However, it turned out that the reproducibility of these results is not readily given, as it is in experiments with INPs and *Tm*AFP, which so far impedes any general conclusions. Moreover, while a pH effect could be excluded for INPs, this has to be checked carefully for every investigated protein.

Taking these difficulties aside, we believe that an advanced study, comparing the temperature effects on natural and heat-treated benchmark protein solutions, would be very instructive. The investigation of the water alignment observed in the O–H/O–D stretch region can, as in Chapter 6, be accompanied by Amide I region SFG and CD spectroscopy, to investigate the respective effects on the structures of the proteins. Although clear evidence for a sensitivity of the SFG water signal for ice nucleation sites might eventually remain hardly obtainable, the results could serve as a reference for studies of INPs and other ice-binding proteins. Besides that, insights into the interface between benchmark proteins with known 3D structures and water, and its temperature and structure dependence, might be of high interest for further fields of research.

The phase-resolved SFG setup presented in Chapter 3 is well-suited for the proposed studies. Its collinear geometry and phase-stability enable long-term measurements of liquid samples in all required frequency regions. Phase-resolution provides increased possibilities for decomposing the spectra, while the tunable VIS bandwidth using the implemented pulse shaper enables measurements at high spectral resolution.

In fact, there is a large variety of other ice-binding proteins, for which the experimental methodology described in this thesis could be applied: INs of ice-nucleating fungi (e.g., *Fusarium acuminatum* and *Mortierella alpina*)[130,156,230,231] are not membrane-bound and can hence be purified to very high qualities using ice-affinity purification methods. The same assumption can be made in regard to ice-nucleating pollen and lichen. Recently, performing droplet freezing assays, Cascajo-Castresana *et al.* have

demonstrated decent ice nucleation activity for a series of further biomolecules, of which the iron storage protein (apo)ferritin reached the highest ice nucleation efficiency.[232]

Finding an applicable parameterization of the spectroscopic results, and referencing them to suitable TINA data, might help to quantify the results and thereby to trace which molecular-level observations are characteristic for ice nucleation mechanisms. Examples for such parameters are the integrated intensity and the shift of the spectral centroid of the O–H/O–D stretch band. Figure 8.1 compares temperature-dependent SFG spectra of *P. syringae*, *Fusarium acuminatum* and *Mortierella alpina* in H_2O and D_2O. They represent an early attempt to realize the above proposed quantification of the effects on the spectra via fitting parameters. While the described increase and red-shift at low temperatures can be observed for all investigated ice nucleators, the magnitudes of the effects are varying significantly when comparing individual samples, demanding for higher statistics, normalization approaches, or advanced control over the sample quality and homogeneity.

Taken together, the investigation of ice-binding biomolecules is obviously still far from being concluded. Undoubtedly, high statistics ice nucleation assays, and sample purification and modification methods remain the main tools for unraveling the complex mechanisms of the manifold of known and still unrevealed ice nucleators. However, complemented by advanced spectroscopic methods, our investigations on the ice nucleators from *P. syringae* have provided valuable insights in their working mechanism, and could possibly serve as a guide for future studies.
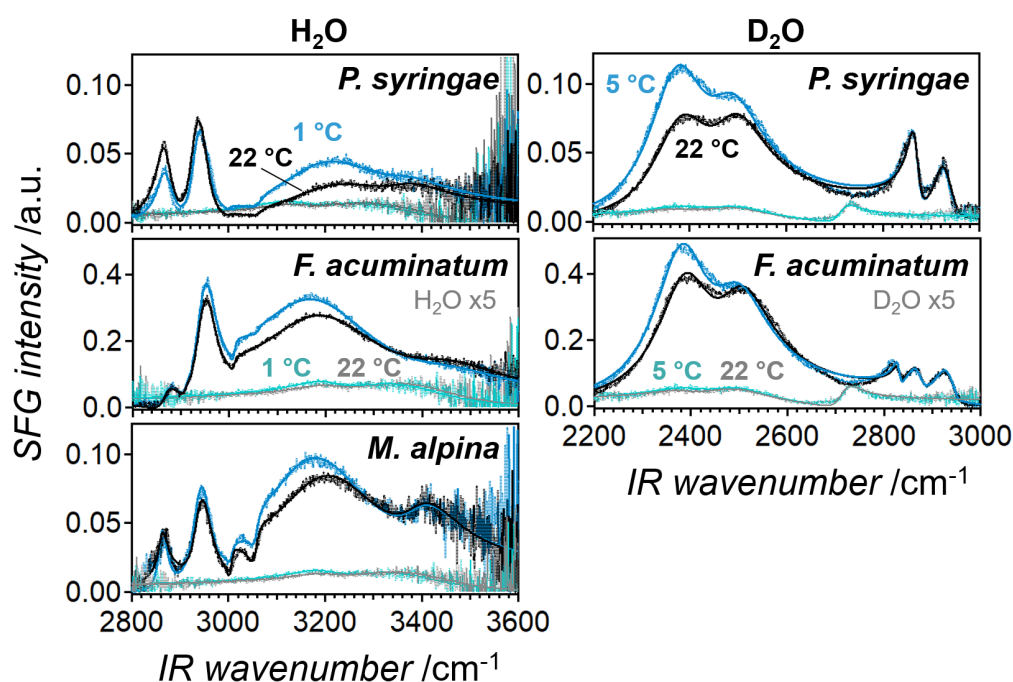
Figure 8.1: Temperature-dependent SFG measurements of *P. syringae*, *Fusarium acuminatum* and *Mortierella alpina* in H$_2$O and D$_2$O - Experiments were conducted at room temperature (black) and at low temperature (blue), $\sim 1\,°C$ above the melting point as in Chapter 6. Grey and cyan spectra correspond to temperature-dependent reference measurements of pure H$_2$O or D$_2$O and are scaled by a factor of 5 in the panels corresponding to *Fusarium acuminatum*. All spectra show the debated increase and red-shift in the low-frequency region of the O–H/O–D stretch band. The spectra shown in this overview represent only one cooling cycle of several datasets, each consisting of multiple cycles. Solid lines indicate spectral fits. Fungal solutions were prepared by, and as described in, Kunert *et al.*[231] and were not further purified.

References

[1] M. Lukas, E. H. G. Backus, M. Bonn, and M. Grechko. **Passively Stabilized Phase-Resolved Collinear SFG Spectroscopy Using a Displaced Sagnac Interferometer**. *Submitted to the Journal of Physical Chemistry A*, 2021.

[2] M. Lukas, R. Schwidetzky, A. T. Kunert, et al. **Electrostatic Interactions Control the Functionality of Bacterial Ice Nucleators**. *Journal of the American Chemical Society*, **142**(15):6842–6846, 2020. 46, 80, 85, 100, 106, 121, 122, 123, 124, 126

[3] R. Schwidetzky, M. Lukas, A. YazdanYar, et al. **Specific Ion–Protein Interactions Influence Bacterial Ice Nucleation**. *Chemistry – A European Journal*, **27**(26):7402–7407, 2021. 121, 122, 125, 126

[4] M. Lukas, R. Schwidetzky, A. T. Kunert, et al. **Interfacial Water Ordering Is Insufficient to Explain Ice-Nucleating Protein Activity**. *The Journal of Physical Chemistry Letters*, **12**(1):218–223, 2020. 114, 115, 121, 124, 126, 131

[5] M. Lukas, R. Schwidetzky, R. J. Eufemio, et al. **Towards Understanding Bacterial Ice Nucleation**. *Submitted to the Journal of Physical Chemistry B*, 2021. 8, 40

[6] V. Ramanathan, R. D. Cess, E. F. Harrison, et al. **Cloud-Radiative Forcing and Climate: Results from the Earth Radiation Budget Experiment**. *Science*, **243**(4887):57–63, 1989. 2, 118

[7] Q. Fu and K. N. Liou. **Parameterization of the Radiative Properties of Cirrus Clouds**. *Journal of Atmospheric Sciences*, **50**(13):2008–2025, 1993. 2, 118

[8] B. J. Murray, S. L. Broadley, T. W. Wilson, et al. **Kinetics of the homogeneous freezing of water**. *Physical Chemistry Chemical Physics*, **12**(35):10380–7, 2010. 2, 40, 98

[9] C. Hoose and O. Möhler. **Heterogeneous ice nucleation on atmospheric aerosols: a review of results from laboratory experiments**. *Atmospheric Chemistry and Physics*, **12**(20):9817–9854, 2012. 2, 5

[10] N. H. Fletcher. *The Chemical Physics of Ice*. Cambridge Monographs on Physics. Cambridge University Press, 1970. 2, 3, 4, 5

[11] P. K. Wolber. **Bacterial Ice Nucleation**. **34** of *Advances in Microbial Physiology*, pages 203–237. Academic Press, 1993. 2, 3, 4, 5, 6, 7, 10, 119, 124, 130

[12] J. Mullin. *Crystallization*. Chemical, Petrochemical & Process. Elsevier Science, 2001. 2, 3

[13] T. Koop. **Homogeneous Ice Nucleation in Water and Aqueous Solutions**. *Zeitschrift für Physikalische Chemie*, **218**(11):1231–1258, 2004. 2

[14] B. J. Murray, D. O'Sullivan, J. D. Atkinson, and M. E. Webb. **Ice nucleation by particles immersed in supercooled cloud droplets**. *Chemical Society Reviews*, **41**(19):6519–6554, 2012. 2, 3, 4, 5, 6, 62, 118

[15] H. R. Pruppacher and J. D. Klett. *Microphysics of clouds and precipitation*. Atmospheric and Oceanographic Sciences Library. Springer, Dordrecht, 2., rev. and expanded ed., with an introduction to cloud chemistry and cloud electricity edition, 1997. 4, 5, 40, 118

[16] T. Koop, B. Luo, A. Tsias, and T. Peter. **Water activity as the determinant for homogeneous ice nucleation in aqueous solutions**. *Nature*, **406**(6796):611–4, 2000. 4, 76, 77, 98, 118

[17] A. Korolev, G. McFarquhar, P. R. Field, et al. **Mixed-Phase Clouds: Progress and Challenges**. *Meteorological Monographs*, **58**:5.1–5.50, 2017. 4

[18] J. F. Leslie and B. A. Summerell. *The fusarium laboratory manual*. Blackwell Pub, Ames, Iowa, 1st ed. edition, 2006. 4

[19] P. Forster, V. Ramaswamy, P. Artaxo, et al. *Changes in Atmospheric Constituents and in Radiative Forcing Chapter 2*. Cambridge University Press, United Kingdom, 2007. 4

[20] D. v. Spracklen, K. S. Carslaw, J. Merikanto, et al. **Explaining global surface aerosol number concentrations in terms of primary emissions and particle formation**. *Atmospheric Chemistry and Physics*, **10**(10):4775–4793, 2010. 4

[21] D. V. Spracklen, K. S. Carslaw, U. Pöschl, et al. **Global cloud condensation nuclei influenced by carbonaceous combustion aerosol**. *Atmospheric Chemistry and Physics*, **11**(17):9067–9087, 2011. 4

[22] P. J. DeMott, A. J. Prenni, X. Liu, et al. **Predicting global atmospheric ice nuclei distributions and their impacts on climate**. *Proceedings of the National Academy of Sciences of the United States of America*, **107**(25):11217–11222, 2010. 4

[23] J. H. Seinfeld and S. N. Pandis. *Atmospheric chemistry and physics: From air pollution to climate change*. Wiley, Hoboken, New Jersey, 3rd edition edition, 2016. 4

[24] B. J. Mason and J. Maybank. **Ice-nucleating properties of some natural mineral dusts**. *Quarterly Journal of the Royal Meteorological Society*, **84**(361):235–241, 1958. 5

[25] G. Vali, M. Christensen, R. W. Fresh, et al. **Biogenic Ice Nuclei. Part II: Bacterial Sources**. *Journal of Atmospheric Sciences*, **33**(8):1565 – 1570, 1976. 5

[26] M. A. Turner, F. Arellano, and L. M. Kozloff. **Three separate classes of bacterial ice nucleation structures**. *Journal of Bacteriology*, **172**(5):2521–6, 1990. 5, 7, 9, 10, 62, 63, 64, 67, 77, 98, 100, 120, 123, 130

REFERENCES

[27] J. D. ATKINSON, B. J. MURRAY, M. T. WOODHOUSE, ET AL. **The importance of feldspar for ice nucleation by mineral dust in mixed-phase clouds.** *Nature*, **498**:355, 2013. 5, 6, 118

[28] C. BUDKE AND T. KOOP. **BINARY: an optical freezing array for assessing temperature and time dependence of heterogeneous ice nucleation.** *Atmospheric Measurement Techniques*, **8**(2):689–703, 2015. 5, 63, 64, 77, 99, 123

[29] D. BEISCHER. **Kinetik der Phasenbildung. Von Prof. Dr. M. Volmer. (Die chemische Reaktion, Bd. 4.) 220 Seiten mit 61 Abbildungen und 15 Tabellen. Format 8°. Verlag Theodor Steinkopff, Dresden 1939. Preis geb. RM 20.—, brosch. RM 19 —.** *Zeitschrift für Elektrochemie und angewandte physikalische Chemie*, **46**(5):327–327, 1940. 5

[30] A. KISELEV, F. BACHMANN, P. PEDEVILLA, ET AL. **Active sites in heterogeneous ice nucleation—the example of K-rich feldspars.** *Science*, **355**(6323):367–371, 2017. 6

[31] A. ABDELMONEM, E. H. G. BACKUS, N. HOFFMANN, ET AL. **Surface-charge-induced orientation of interfacial water suppresses heterogeneous ice nucleation on α-alumina (0001).** *Atmospheric Chemistry and Physics*, **17**(12):7827–7837, 2017. 6, 46

[32] M. A. HOLDEN, T. F. WHALE, M. D. TARN, ET AL. **High-speed imaging of ice nucleation in water proves the existence of active sites.** *Science Advances*, **5**(2):eaav4316, 2019. 6

[33] M. ANDREAE AND D. ROSENFELD. **Aerosol–cloud–precipitation interactions. Part 1. The nature and sources of cloud-active aerosols.** *Earth-Science Reviews*, **89**(1):13–41, 2008. 6

[34] O. MÖHLER, P. J. DEMOTT, G. VALI, AND Z. LEVIN. **Microbiology and atmospheric processes: the role of biological particles in cloud physics.** *Biogeosciences*, **4**(6):1059–1071, 2007. 6

[35] C. HOOSE, J. E. KRISTJÁNSSON, J.-P. CHEN, AND A. HAZRA. **A Classical-Theory-Based Parameterization of Heterogeneous Ice Nucleation by Mineral Dust, Soot, and Biological Particles in a Global Climate Model.** *Journal of the Atmospheric Sciences*, **67**(8):2483 – 2503, 2010. 6

[36] L. R. MAKI, E. L. GALYAN, M. M. CHANG-CHIEN, AND D. R. CALDWELL. **Ice nucleation induced by pseudomonas syringae.** *Applied Microbiology*, **28**(3):456–9, 1974. 7, 62, 63, 68, 98, 100, 119

[37] D. C. ARNY, S. E. LINDOW, AND C. D. UPPER. **Frost sensitivity of Zea mays increased by application of Pseudomonas syringae.** *Nature*, **262**(5566):282–284, 1976. 7, 119

[38] S. E. LINDOW, D. C. ARNY, AND C. D. UPPER. **Erwinia herbicola: a bacterial ice nucleus active in increasing frost injury to corn.** *Phytopathology*, **68**(3):523–527, 1978. 7, 119

[39] H. K. KIM, C. ORSER, S. E. LINDOW, AND D. C. SANDS. **Xanthomonas campestris pv. translucens strains active in ice nucleation.** *Plant Disease*, **71**(11):994–997, 1987. 7, 119

[40] K. C. FAILOR, D. G. SCHMALE, B. A. VINATZER, AND C. L. MONTEIL. **Ice nucleation active bacteria in precipitation are genetically diverse and nucleate ice by employing different mechanisms.** *The ISME Journal*, **11**(12):2740–2753, 2017. 7, 119

[41] L. M. KOZLOFF, M. A. SCHOFIELD, AND M. LUTE. **Ice nucleating activity of Pseudomonas syringae and Erwinia herbicola.** *Journal of Bacteriology*, **153**(1):222–231, 1983. 7, 10, 62, 67, 98, 121

[42] S. E. LINDOW, D. C. ARNY, AND C. D. UPPER. **Bacterial ice nucleation: a factor in frost. injury to plants.** *Plant Physiology*, **70**, 1982. 7, 118, 119

[43] **Snomax International.** https://www.snomax.com/. Accessed: 2021-09-30. 7

[44] H. WEX, S. AUGUSTIN-BAUDITZ, Y. BOOSE, ET AL. **Intercomparing different devices for the investigation of ice nucleating particles using Snomax® as test substance.** *Atmospheric Chemistry and Physics*, **15**(3):1463–1485, 2015. 7, 63, 77

[45] A. T. KUNERT, M. LAMNECK, F. HELLEIS, ET AL. **Twin-plate Ice Nucleation Assay (TINA) with infrared detection for high-throughput droplet freezing experiments with biological ice nuclei in laboratory and field samples.** *Atmospheric Measurement Techniques*, **11**(11):6327–6337, 2018. 7, 39, 40, 41, 63, 69, 77, 87, 99, 121

[46] L. WENG, S. N. TESSIER, A. SWEI, ET AL. **Controlled ice nucleation using freeze-dried Pseudomonas syringae encapsulated in alginate beads.** *Cryobiology*, **75**:1–6, 2017. 7

[47] A. G. GOVINDARAJAN AND S. E. LINDOW. **Size of bacterial ice-nucleation sites measured in situ by radiation inactivation analysis.** *Proceedings of the National Academy of Sciences*, **85**(5):1334–1338, 1988. 7, 8, 10, 62, 76, 98, 100, 120

[48] S. E. LINDOW, E. LAHUE, A. G. GOVINDARAJAN, ET AL. **Localization of ice nucleation activity and the iceC gene product in Pseudomonas syringae and Escherichia coli.** *Molecular Plant-Microbe Interactions*, **2**(5):262–272, 1989. 7

[49] C. ORSER, B. J. STASKAWICZ, N. J. PANOPOULOS, ET AL. **Cloning and expression of bacterial ice nucleation genes in Escherichia coli.** *Journal of Bacteriology*, **164**(1):359–366, 1985. 7, 119

[50] P. WOLBER AND G. WARREN. **Bacterialice-nucleation proteins.** *Trends in Biochemical Sciences*, **14**(5):179–182, 1989. 7, 9, 10, 130

[51] P. L. DAVIES AND B. D. SYKES. **Antifreeze proteins.** *Current Opinion in Structural Biology*, **7**(6):828–834, 1997. 9, 120

[52] F. SICHERI AND D. S. C. YANG. **Ice-binding structure and mechanism of an antifreeze protein from winter flounder.** *Nature*, **375**(6530):427–431, 1995. 9

[53] Y. C. LIOU, A. TOCILJ, P. L. DAVIES, AND Z. JIA. **Mimicry of ice structure by surface hydroxyls and water of a beta-helix antifreeze protein.** *Nature*, **406**, 2000. 9, 119, 120

[54] S. P. Graether, M. J. Kuiper, S. M. Gagné, et al. **Beta-helix structure and ice-binding properties of a hyperactive antifreeze protein from an insect**. *Nature*, **406**, 2000. 9, 119, 120

[55] E. K. Leinala, P. L. Davies, and Z. Jia. **Crystal Structure of β-Helical Antifreeze Protein Points to a General Ice Binding Model**. *Structure*, **10**(5):619–627, 2002. 9

[56] B. L. Pentelute, Z. P. Gates, V. Tereshko, et al. **X-ray structure of snow flea antifreeze protein determined by racemic crystallization of synthetic protein enantiomers**. *Journal of the American Chemical Society*, **130**, 2008. 9

[57] J. A. Raymond and A. L. DeVries. **Adsorption inhibition as a mechanism of freezing resistance in polar fishes**. *Proceedings of the National Academy of Sciences*, **74**(6):2589–2593, 1977. 9

[58] J. G. Duman. **Antifreeze and ice nucleator proteins in terrestrial arthropods**. *Annual Review of Physiology*, **63**(1):327–57, 2001. 9, 99

[59] P. Naullage, Y. Qiu, and V. Molinero. **What Controls the Limit of Supercooling and Superheating of Pinned Ice Surfaces?** *The Journal of Physical Chemistry Letters*, **9**(7):1712–1720, April 2018. 9

[60] A. Hakim, D. Thakral, D. F. Zhu, and J. B. Nguyen. **Expression, purification, crystallization and preliminary crystallographic studies of Rhagium inquisitor antifreeze protein**. *Acta Crystallographica Section F*, **68**(Pt 5):547–50, 2012. 9, 105, 119

[61] S. P. Graether and Z. Jia. **Modeling Pseudomonas syringae ice-nucleation protein as a beta-helical protein**. *Biophysical Journal*, **80**, 2001. 9, 120

[62] Y. Kumaki, K. Kawano, K. Hikichi, et al. **A circular loop of the 16-residue repeating unit in ice nucleation protein**. *Biochemical and Biophysical Research Communications*, **371**, 2008. 9, 119

[63] A. V. Kajava and S. E. Lindow. **A model of the three-dimensional structure of ice nucleation proteins**. *Journal of molecular biology*, **232**(3):709–717, 1993. 9, 119

[64] H. Mizuno. **Prediction of the conformation of ice-nucleation protein by conformational energy calculation**. *Proteins: Structure, Function, and Bioinformatics*, **5**(1):47–65, 1989. 9

[65] C. P. Garnham, R. L. Campbell, V. K. Walker, and P. L. Davies. **Novel dimeric beta-helical model of an ice nucleation protein with bridged active sites**. *BMC Structural Biology*, **11**:36, 2011. 9, 62, 76, 98, 100, 120

[66] U. S. Midya and S. Bandyopadhyay. **Interfacial Water Arrangement in the Ice-Bound State of an Antifreeze Protein: A Molecular Dynamics Simulation Study**. *Langmuir*, **33**(22):5499–5510, June 2017. 9

[67] A. Hudait, N. Odendahl, Y. Qiu, et al. **Ice-Nucleating and Antifreeze Proteins Recognize Ice through a Diversity of Anchored Clathrate and Ice-like Motifs**. *Journal of the American Chemical Society*, **140**(14):4905–4912, 2018. 9, 82, 89, 100, 104, 106, 109, 119, 120, 132

[68] Y. Kobashigawa, Y. Nishimiya, K. Miura, et al. **A part of ice nucleation protein exhibits the ice-binding ability**. *FEBS Letters*, **579**(6):1493–7, 2005. 9

[69] S. A. Yankofsky, Z. Levin, T. Bertold, and N. Sandlerman. **Some Basic Characteristics of Bacterial Freezing Nuclei**. *Journal of Applied Meteorology*, **20**(9):1013–1019, 1981. 9, 10, 100, 120, 123

[70] R. Schwidetzky, P. Sudera, A. T. Backes, et al. **Membranes Are Decisive for Maximum Freezing Efficiency of Bacterial Ice Nucleators**. *The Journal of Physical Chemistry Letters*, pages 10783–10787, November 2021. 10, 123, 131

[71] M. W. Southworth, P. K. Wolber, and G. J. Warren. **Nonlinear Relationship between Concentration and Activity of a Bacterial Ice Nucleation Protein**. *Journal of Biological Chemistry*, **263**(29):15211–15216, 1988. 10, 62, 98, 120, 121

[72] L. M. Kozloff, M. Lute, and D. Westaway. **Phosphatidylinositol as a Component of the Ice Nucleating Site of Pseudomonas syringae and Erwinia herbiola**. *Science*, **226**(4676):845–846, 1984. 10, 121

[73] Y. Qiu, A. Hudait, and V. Molinero. **How Size and Aggregation of Ice-Binding Proteins Control Their Ice Nucleation Efficiency**. *Journal of the American Chemical Society*, **141**(18):7439–7452, 2019. 10, 62, 100, 106, 121, 124, 126, 130, 131

[74] I. Newton. *Opticks: or, A treatise of the reflections, refractions, inflections, and colours of light*. Good Press, 2019. 11

[75] P. W. Atkins. *Atkins' physical chemistry*. Oxford University Press, Oxford, tenth edition edition, 2014. 12, 13

[76] P. A. Franken, A. E. Hill, C. W. Peters, and G. Weinreich. **Generation of Optical Harmonics**. *Physical Review Letters*, **7**:118–119, Aug 1961. 14

[77] M. Bass, P. A. Franken, A. E. Hill, et al. **Optical Mixing**. *Physical Review Letters*, **8**:18–18, Jan 1962. 14

[78] J. A. Armstrong, N. Bloembergen, J. Ducuing, and P. S. Pershan. **Interactions between Light Waves in a Nonlinear Dielectric**. *Physical Review*, **127**:1918–1939, Sep 1962. 14

[79] N. Bloembergen and P. S. Pershan. **Light Waves at the Boundary of Nonlinear Media**. *Physical Review*, **128**:606–622, Oct 1962. 14, 58

[80] J. Ducuing and N. Bloembergen. **Observation of Reflected Light Harmonics at the Boundary of Piezoelectric Crystals**. *Phys. Rev. Lett.*, **10**:474–476, Jun 1963. 14

[81] T. Rasing, Y. R. Shen, M. W. Kim, and S. Grubb. **Observation of molecular reorientation at a two-dimensional-liquid phase transition**. *Physical Review Letters*, **55**:2903–2906, Dec 1985. 14

REFERENCES

[82] J. M. HICKS, K. KEMNITZ, K. B. EISENTHAL, AND T. F. HEINZ. **Studies of liquid surfaces by second harmonic generation**. *Journal of Physical Chemistry*, **90**(4):560–562, February 1986. 14

[83] X.-D. XIAO, V. VOGEL, AND Y. SHEN. **Probing the proton excess at interfaces by second harmonic generation**. *Chemical Physics Letters*, **163**(6):555–559, 1989. 14

[84] C. V. SHANK, R. YEN, AND C. HIRLIMANN. **Femtosecond-Time-Resolved Surface Structural Dynamics of Optically Excited Silicon**. *Physical Review Letters*, **51**:900–902, Sep 1983. 14

[85] G. T. BOYD, Y. R. SHEN, AND T. W. HÄNSCH. **Continuous-wave second-harmonic generation as a surface microprobe**. *Optics Letters*, **11**(2):97–99, Feb 1986. 14

[86] Y. R. SHEN. *Fundamentals of Sum-Frequency Spectroscopy*. Cambridge Molecular Science. Cambridge University Press, 2016. 14, 15, 16, 19, 24

[87] J. HUNT, P. GUYOT-SIONNEST, AND Y. SHEN. **Observation of C-H stretch vibrations of monolayers of molecules optical sum-frequency generation**. *Chemical Physics Letters*, **133**(3):189–192, 1987. 14, 24

[88] J. Y. ZHANG, J. Y. HUANG, Y. R. SHEN, AND C. CHEN. **Optical parametric generation and amplification in barium borate and lithium triborate crystals**. *Journal of the Optical Society of America*, **10**(9):1758–1764, Sep 1993. 15

[89] L. J. RICHTER, T. P. PETRALLI-MALLOW, AND J. C. STEPHENSON. **Vibrationally resolved sum-frequency generation with broad-bandwidth infrared pulses**. *Optics Letters*, **23**(20):1594–1596, Oct 1998. 15

[90] R. SUPERFINE, J. Y. HUANG, AND Y. R. SHEN. **Phase measurement for surface infrared–visible sum-frequency generation**. *Optics Letters*, **15**(22):1276–1278, Nov 1990. 15, 24, 33, 46

[91] V. OSTROVERKHOV, G. A. WAYCHUNAS, AND Y. SHEN. **Vibrational spectra of water at water/α-quartz (0001) interface**. *Chemical Physics Letters*, **386**(1):144–148, 2004. 15, 33

[92] I. V. STIOPKIN, C. WEERAMAN, P. A. PIENIAZEK, ET AL. **Hydrogen bonding at the water surface revealed by isotopic dilution spectroscopy**. *Nature*, **474**(7350):192–195, 2011. 15, 33

[93] S. NIHONYANAGI, S. YAMAGUCHI, AND T. TAHARA. **Direct evidence for orientational flip-flop of water molecules at charged interfaces: A heterodyne-detected vibrational sum frequency generation study**. *The Journal of Chemical Physics*, **130**(20):204704, 2009. 15, 33, 46, 47, 53

[94] P. C. SINGH, S. NIHONYANAGI, S. YAMAGUCHI, AND T. TAHARA. **Ultrafast vibrational dynamics of water at a charged interface revealed by two-dimensional heterodyne-detected vibrational sum frequency generation**. *The Journal of Chemical Physics*, **137**(9):094706, 2012. 15, 33

[95] S. NIHONYANAGI, J. A. MONDAL, S. YAMAGUCHI, AND T. TAHARA. **Structure and Dynamics of Interfacial Water Studied by Heterodyne-Detected Vibrational Sum-Frequency Generation**. *Annual Review of Physical Chemistry*, **64**(1):579–603, 2013. PMID: 23331304. 15, 33, 58

[96] L. B. DREIER, Y. NAGATA, H. LUTZ, ET AL. **Saturation of charge-induced water alignment at model membrane surfaces**. *Science Advances*, **4**(3), 2018. 15, 124

[97] Y. NOJIMA, Y. SUZUKI, AND S. YAMAGUCHI. **Weakly Hydrogen-Bonded Water Inside Charged Lipid Monolayer Observed with Heterodyne-Detected Vibrational Sum Frequency Generation Spectroscopy**. *The Journal of Physical Chemistry C*, **121**(4):2173–2180, February 2017. 15, 46, 53

[98] L. B. DREIER, M. BONN, AND E. H. G. BACKUS. **Hydration and Orientation of Carbonyl Groups in Oppositely Charged Lipid Monolayers on Water**. *Journal of Physical Chemistry B*, **123**(5):1085–1089, 2019. 15, 46, 103

[99] L. B. DREIER, A. WOLDE-KIDAN, D. J. BONTHUIS, ET AL. **Unraveling the Origin of the Apparent Charge of Zwitterionic Lipid Layers**. *The Journal of Physical Chemistry Letters*, **10**(20):6355–6359, 2019. 15, 46

[100] L. FU, J. LIU, AND E. C. Y. YAN. **Chiral Sum Frequency Generation Spectroscopy for Characterizing Protein Secondary Structures at Interfaces**. *Journal od the American Chemical Society*, **133**(21):8094–8097, June 2011. 15

[101] M. BONN, H. J. BAKKER, Y. TONG, AND E. H. G. BACKUS. **No Ice-Like Water at Aqueous Biological Interfaces**. *Biointerphases*, **7**(1):20, 2012. 15

[102] S. HOSSEINPOUR, S. J. ROETERS, M. BONN, ET AL. **Structure and Dynamics of Interfacial Peptides and Proteins from Vibrational Sum-Frequency Generation Spectroscopy**. *Chemical Review*, **120**(7):3420–3465, April 2020. 15

[103] T. GUCKEISEN, S. HOSSEINPOUR, AND W. PEUKERT. **Effect of pH and urea on the proteins secondary structure at the water/air interface and in solution**. *Journal of Colloid and Interface Science*, **590**:38–49, 2021. 15

[104] R. W. BOYD. *Nonlinear Optics, Third Edition*. Academic Press, Inc., USA, 3rd edition, 2008. 16, 19, 24

[105] A. G. LAMBERT, P. B. DAVIES, AND D. J. NEIVANDT. **Implementing the Theory of Sum Frequency Generation Vibrational Spectroscopy: A Tutorial Review**. *Applied Spectroscopy Reviews*, **40**(2):103–145, 2005. 16, 20, 21, 22, 23, 24

[106] S. MUKAMEL. *Principles of Nonlinear Optical Spectroscopy*. Oxford series in optical and imaging sciences. Oxford University Press, 1995. 17, 24

[107] Y. R. SHEN. **Revisiting the basic theory of sum-frequency generation**. *The Journal of Chemical Physics*, **153**(18):180901, 2020. 21

[108] H. HORA. **Y. R. Shen, The Principles of Nonlinear Optics, John Wiley & Sons, New York, 1984, 576 pages**. *Laser and Particle Beams*, **4**(2):318–319, 1986. 23

[109] X. Zhuang, P. B. Miranda, D. Kim, and Y. R. Shen. **Mapping molecular orientation and conformation at interfaces by surface nonlinear optics**. *Physical Review B*, **59**:12632–12640, May 1999. 23

[110] H.-F. Wang, W. Gan, R. Lu, et al. **Quantitative spectral and orientational analysis in surface sum frequency generation vibrational spectroscopy (SFG-VS)**. *International Reviews in Physical Chemistry*, **24**(2):191–256, 2005. 23, 24

[111] W. Gan, B.-h. Wu, Z. Zhang, et al. **Vibrational Spectra and Molecular Orientation with Experimental Configuration Analysis in Surface Sum Frequency Generation (SFG)**. *Journal of Physical Chemistry C*, **111**(25):8716–8725, June 2007. 23

[112] E. H. G. Backus, N. Garcia-Araez, M. Bonn, and H. J. Bakker. **On the Role of Fresnel Factors in Sum-Frequency Generation Spectroscopy of Metal-Water and Metal-Oxide-Water Interfaces**. *Journal of Physical Chemistry C*, **116**(44):23351–23361, November 2012. 23

[113] J. Löbau and K. Wolfrum. **Sum-frequency spectroscopy in total internal reflection geometry: signal enhancement and access to molecular properties**. *Journal of the Optical Society of America*, **14**(10):2505–2512, Oct 1997. 23

[114] D. A. Woods and C. D. Bain. **Total internal reflection spectroscopy for studying soft matter**. *Soft Matter*, **10**:1071–1096, 2014. 23

[115] N. Takeshita, M. Okuno, and T.-a. Ishibashi. **Development of Heterodyne-Detected Total Internal Reflection Vibrational Sum Frequency Generation Spectroscopy and Its Application to CaF 2 /Liquid Interfaces**. *The Journal of Physical Chemistry C*, **121**, 11 2017. 23

[116] C. Hirose, N. Akamatsu, and K. Domen. **Formulas for the Analysis of the Surface SFG Spectrum and Transformation Coefficients of Cartesian SFG Tensor Components**. *Applied Spectroscopy*, **46**(6):1051–1072, Jun 1992. 24

[117] X. Wei, S.-C. Hong, X. Zhuang, et al. **Nonlinear optical studies of liquid crystal alignment on a rubbed polyvinyl alcohol surface**. *Physical Review E*, **62**:5160–5172, Oct 2000. 24

[118] C. Lawrence and J. Skinner. **Ultrafast infrared spectroscopy probes hydrogen-bonding dynamics in liquid water**. *Chemical Physics Letters*, **369**(3-4):472–477, 2003. 32

[119] R. Rey, K. B. Møller, and J. T. Hynes. **Hydrogen Bond Dynamics in Water and Ultrafast Infrared Spectroscopy**. *The Journal of Physical Chemistry A*, **106**(50):11993–11996, 2002. 32

[120] C. Tian, N. Ji, G. A. Waychunas, and Y. R. Shen. **Interfacial Structures of Acidic and Basic Aqueous Solutions**. *Journal of the American Chemical Society*, **130**(39):13033–13039, October 2008. 33

[121] N. Ji, V. Ostroverkhov, C.-Y. Chen, and Y.-R. Shen. **Phase-Sensitive Sum-Frequency Vibrational Spectroscopy and Its Application to Studies of Interfacial Alkyl Chains**. *Journal of the American Chemical Society*, **129**(33):10056–10057, August 2007. 33, 46, 47

[122] L. Lepetit, G. Chériaux, and M. Joffre. **Linear techniques of phase measurement by femtosecond spectral interferometry for applications in spectroscopy**. *Journal of the Optical Society of America*, **12**(12):2467–2474, Dec 1995. 33, 47

[123] V. Ostroverkhov, G. A. Waychunas, and Y. R. Shen. **New Information on Water Interfacial Structure Revealed by Phase-Sensitive Surface Spectroscopy**. *Physical Review Letters*, **94**:046102, Feb 2005. 33, 46, 47

[124] N. Ji, V. Ostroverkhov, C. S. Tian, and Y. R. Shen. **Characterization of Vibrational Resonances of Water-Vapor Interfaces by Phase-Sensitive Sum-Frequency Spectroscopy**. *Physical Review Letters*, **100**:096102, Mar 2008. 33, 46, 47

[125] I. V. Stiopkin, H. D. Jayathilake, A. N. Bordenyuk, and A. V. Benderskii. **Heterodyne-Detected Vibrational Sum Frequency Generation Spectroscopy**. *Journal of the American Chemical Society*, **130**(7):2271–2275, February 2008. 33, 47

[126] S. Yamaguchi and T. Tahara. **Heterodyne-detected electronic sum frequency generation: "Up" versus "down" alignment of interfacial molecules**. *The Journal of Chemical Physics*, **129**(10):101102, 2008. 33, 35, 47, 48, 52

[127] C. Froehly, B. Colombeau, and M. Vampouille. **II Shaping and Analysis of Picosecond Light Pulses**. **20** of *Progress in Optics*, pages 63–153. Elsevier, 1983. 37

[128] **Open Access license CC BY 4.0.** . 39

[129] G. Vali. **Quantitative Evaluation of Experimental Results an the Heterogeneous Freezing Nucleation of Supercooled Liquids**. *Journal of the Atmospheric Sciences*, **28**(3):402–409, 1971. 40, 41, 63, 99, 123

[130] J. Fröhlich-Nowoisky, T. C. J. Hill, B. G. Pummer, et al. **Ice nucleation activity in the widespread soil fungus Mortierella alpina**. *Biogeosciences*, **12**(4):1057–1071, 2015. 40, 132

[131] A. J. Miles and B. A. Wallace. **Circular dichroism spectroscopy of membrane proteins**. *Chemical Society Reviews*, **45**:4859–4872, 2016. 42, 43

[132] **Open Access license CC BY-NC 3.0.** https://creativecommons.org/licenses/by-nc/3.0/. 43

[133] E. C. McCusker, C. Bagnéris, C. E. Naylor, et al. **Structure of a bacterial voltage-gated sodium channel pore reveals mechanisms of opening and closing**. *Nature Communications*, **3**(1):1102, 2012. 43

[134] A. Abdul-Gader, A. J. Miles, and B. A. Wallace. **A reference dataset for the analyses of membrane protein secondary structures and transmembrane residues using circular dichroism spectroscopy**. *Bioinformatics*, **27**(12):1630–1636, 04 2011. 43

REFERENCES

[135] L. Whitmore, B. Woollett, A. J. Miles, et al. **PCDDB: the protein circular dichroism data bank, a repository for circular dichroism spectral and metadata.** *Nucleic Acids Research*, **39**(suppl1):D480–D486, 11 2010. 42, 43

[136] Y. R. Shen. **Surface properties probed by second-harmonic and sum-frequency generation.** *Nature*, **337**(6207):519–525, 1989. 46

[137] K. B. Eisenthal. **Liquid Interfaces Probed by Second-Harmonic and Sum-Frequency Spectroscopy.** *Chemical Reviews*, **96**(4):1343–1360, January 1996. 46, 58

[138] P. B. Miranda and Y. R. Shen. **Liquid Interfaces: A Study by Sum-Frequency Vibrational Spectroscopy.** *Journal of Physical Chemistry B*, **103**(17):3292–3307, April 1999. 46

[139] G. L. Richmond. **Molecular Bonding and Interactions at Aqueous Surfaces as Probed by Vibrational Sum Frequency Spectroscopy.** *Chemical Reviews*, **102**(8):2693–2724, August 2002. 46

[140] J. D. Cyran, M. A. Donovan, D. Vollmer, et al. **Molecular hydrophobicity at a macroscopically hydrophilic surface.** *Proceedings of the National Academy of Sciences of the United States of America*, **116**(5):1520–1525, 2019. 46

[141] Y. R. Shen and V. Ostroverkhov. **Sum-Frequency Vibrational Spectroscopy on Water Interfaces: Polar Orientation of Water Molecules at Interfaces.** *Chemical Reviews*, **106**(4):1140–1154, April 2006. 46

[142] J. Schaefer, E. H. G. Backus, Y. Nagata, and M. Bonn. **Both Inter- and Intramolecular Coupling of O–H Groups Determine the Vibrational Response of the Water/Air Interface.** *The Journal of Physical Chemistry Letters*, **7**(22):4591–4595, 2016. 46

[143] T. W. Golbek, J. Franz, J. Elliott Fowler, et al. **Identifying the selectivity of antimicrobial peptides to cell membranes by sum frequency generation spectroscopy.** *Biointerphases*, **12**(2):02D406, 2017. 46, 103

[144] S. Devineau, K.-i. Inoue, R. Kusaka, et al. **Change of the isoelectric point of hemoglobin at the air/water interface probed by the orientational flip-flop of water molecules.** *Physical Chemistry Chemical Physics*, **19**(16):10292–10300, 2017. 46, 66, 124, 130

[145] S. Strazdaite, K. Meister, and H. J. Bakker. **Orientation of polar molecules near charged protein interfaces.** *Physical Chemistry Chemical Physics*, **18**(10):7414–7418, 2016. 46, 66, 67, 124, 130

[146] T. Guckeisen, S. Hosseinpour, and W. Peukert. **Isoelectric Points of Proteins at the Air/Liquid Interface and in Solution.** *Langmuir*, **35**(14):5004–5012, 2019. 46, 66, 124, 130

[147] M. Thämer, R. K. Campen, and M. Wolf. **Detecting weak signals from interfaces by high accuracy phase-resolved SFG spectroscopy.** *Physical Chemistry Chemical Physics*, **20**:25875–25882, 2018. 48

[148] T. Garling, R. K. Campen, M. Wolf, and M. Thämer. **A General Approach To Combine the Advantages of Collinear and Noncollinear Spectrometer Designs in Phase-Resolved Second-Order Nonlinear Spectroscopy.** *Journal of Physical Chemistry A*, **123**(51):11022–11030, December 2019. 48

[149] B. Xu, Y. Wu, D. Sun, et al. **Stabilized phase detection of heterodyne sum frequency generation for interfacial studies.** *Optics Letters*, **40**(19):4472–4475, Oct 2015. 48

[150] S. Sun, P. J. Bisson, M. Bonn, et al. **Phase-Sensitive Sum-Frequency Generation Measurements Using a Femtosecond Nonlinear Interferometer.** *The Journal of Physical Chemistry C*, **123**(12):7266–7270, 2019. 48

[151] Y. Nagata, T. Hasegawa, E. H. G. Backus, et al. **The surface roughness, but not the water molecular orientation varies with temperature at the water–air interface.** *Physical Chemistry Chemical Physics*, **17**:23559–23564, 2015. 52

[152] S. Yamaguchi. **Development of single-channel heterodyne-detected sum frequency generation spectroscopy and its application to the water/vapor interface.** *The Journal of Chemical Physics*, **143**(3):034202, 2015. 53, 59

[153] S. Hosseinpour, F. Tang, F. Wang, et al. **Chemisorbed and Physisorbed Water at the TiO2/Water Interface.** *The Journal Physical Chemistry Letters*, **8**(10):2195–2199, May 2017. 58

[154] S. Nihonyanagi, T. Ishiyama, T.-k. Lee, et al. **Unified molecular view of the air/water interface based on experimental and theoretical $\chi^{(2)}$ spectra of an isotopically diluted water surface.** *Journal of the American Chemical Society*, **133**(42):16875–16880, 2011. 58

[155] R. E. Pool, J. Versluis, E. H. G. Backus, and M. Bonn. **Comparative Study of Direct and Phase-Specific Vibrational Sum-Frequency Generation Spectroscopy: Advantages and Limitations.** *Journal of Physical Chemistry B*, **115**(51):15362–15369, December 2011. 58

[156] A. T. Kunert, M. L. Pöhlker, C. S. Krevert, et al. **Highly active and stable fungal ice nuclei are widespread among Fusarium species.** *Biogeosciences Discussions*, **2019**:1–19, 2019. 62, 132

[157] G. M. Mueller, P. K. Wolber, and G. J. Warren. **Clustering of ice nucleation protein correlates with ice nucleation activity.** *Cryobiology*, **27**(4):416–422, 1990. 62, 98

[158] D. Schmid, D. Pridmore, G. Capitani, et al. **Molecular organisation of the ice nucleation protein InaV from Pseudomonas syringae.** *FEBS Letters*, **414**(3):590–4, 1997. 62

[159] R. Pandey, K. Usui, R. A. Livingstone, et al. **Ice-nucleating bacteria control the order and dynamics of interfacial water.** *Science Advances*, **2**(4):e1501630, 2016. 62, 68, 76, 80, 101, 121, 126, 130

[160] D. Gurian-Sherman and S. E. Lindow. **Bacterial ice nucleation: significance and molecular basis.** *FASEB Journal*, **7**(14):1338–43, 1993. 62, 63, 124, 130

[161] K. Liu, C. Wang, J. Ma, et al. **Janus effect of antifreeze proteins on ice nucleation.** *Proceedings of the National Academy of Sciences*, **113**(51):14739–14744, 2016. 62, 76

[162] G. Bai, D. Gao, Z. Liu, et al. **Probing the critical nucleus size for ice formation with graphene oxide nanosheets.** *Nature*, **576**(7787):437–441, 2019. 62, 76

[163] E. Attard, H. Yang, A.-M. Delort, et al. **Effects of atmospheric conditions on ice nucleation activity of Pseudomonas.** *Atmospheric Chemistry and Physics*, **12**(22), 2012. 63, 67, 76, 77, 85

[164] H. Kawahara, Y. Tanaka, and H. Obata. **Isolation and Characterization of a Novel Ice-nucleating Bacterium, Pseudomonas sp. KUIN-4, Which Has Stable Activity in Acidic Solution.** *Bioscience, biotechnology, and biochemistry*, **59**(8):1528–1532, 1995. 63, 67

[165] K. Meister, S. Strazdaite, A. L. DeVries, et al. **Observation of ice-like water layers at an aqueous protein surface.** *Proceedings of the National Academy of Sciences of the United States of America*, **111**(50):17732–17736, 2014. 65, 80

[166] K. Meister, S. J. Roeters, A. Paananen, et al. **Observation of pH-Induced Protein Reorientation at the Water Surface.** *The Journal of Physical Chemistry Letters*, **8**(8):1772–1776, 2017. 65, 103

[167] K. Engelhardt, W. Peukert, and B. Braunschweig. **Vibrational sum-frequency generation at protein modified air–water interfaces: Effects of molecular structure and surface charging.** *Current Opinion in Colloid & Interface Science*, **19**(3):207–215, 2014. 66, 67, 124, 130

[168] M. Horká, J. Horký, H. Matoušková, and K. Šlais. **Free flow and capillary isoelectric focusing of bacteria from the tomatoes plant tissues.** *Journal of Chromatography A*, **1216**(6):1019–1024, 2009. 67

[169] C. E. Morris, F. Conen, J. Alex Huffman, et al. **Bioprecipitation: a feedback cycle linking earth history, ecosystem dynamics and land use through biological ice nucleators in the atmosphere.** *Global Change Biology*, **20**(2):341–51, 2014. 67, 119

[170] P. W. Wilson, A. F. Heneghan, and A. D. Haymet. **Ice nucleation in nature: supercooling point (SCP) measurements and the role of heterogeneous nucleation.** *Cryobiology*, **46**(1):88–98, 2003. 76

[171] L. R. Maki and K. J. Willoughby. **Bacteria as Biogenic Sources of Freezing Nuclei.** *Journal of Applied Meteorology*, **17**(7):1049–1053, 1978. 76

[172] C. E. Morris, D. G. Georgakopoulos, and D. C. Sands. **Ice nucleation active bacteria and their potential role in precipitation.** *Journal de Physique IV (Proceedings)*, **121**:87–103, 2004. 76

[173] M. T. Reischel and G. Vali. **Freezing Nucleation in Aqueous Electrolytes.** *Tellus*, **27**(4):414–427, 1975. 77, 86

[174] T. Koop and B. Zobrist. **Parameterizations for ice nucleation in biological and atmospheric systems.** *Physical Chemistry Chemical Physics*, **11**(46):10839–10850, 2009. 77, 88, 93

[175] P. Jungwirth and P. S. Cremer. **Beyond Hofmeister.** *Nature Chemistry*, **6**:261, 2014. 77, 80

[176] X. Chen, T. Yang, S. Kataoka, and P. S. Cremer. **Specific Ion Effects on Interfacial Water Structure near Macromolecules.** *Journal of the American Chemical Society*, **129**(40):12272–12279, 2007. 77, 80

[177] D. J. Tobias and J. C. Hemminger. **Getting Specific About Specific Ion Effects.** *Science*, **319**(5867):1197–1198, 2008. 77

[178] F. Hofmeister. **Zur Lehre von der Wirkung der Salze.** *Archiv für experimentelle Pathologie und Pharmakologie*, **24**(4):247–260, 1888. 77

[179] H. I. Okur, J. Hladílková, K. B. Rembert, et al. **Beyond the Hofmeister Series: Ion-Specific Effects on Proteins and Their Biological Functions.** *The Journal of Physical Chemistry B*, **121**(9):1997–2014, 2017. 77

[180] K. D. Collins and M. W. Washabaugh. **The Hofmeister effect and the behaviour of water at interfaces.** *Quarterly Reviews of Biophysics*, **18**(4):323–422, 1985. 77

[181] E. E. Bruce, P. T. Bui, B. A. Rogers, et al. **Nonadditive Ion Effects Drive Both Collapse and Swelling of Thermoresponsive Polymers in Water.** *Journal of the American Chemical Society*, **141**(16):6609–6616, 2019. 77, 80

[182] A. A. Zavitsas. **Properties of Water Solutions of Electrolytes and Nonelectrolytes.** *The Journal of Physical Chemistry B*, **105**(32):7805–7817, 2001. 78

[183] S. Nihonyanagi, S. Yamaguchi, and T. Tahara. **Counterion Effect on Interfacial Water at Charged Interfaces and Its Relevance to the Hofmeister Series.** *Journal of the American Chemical Society*, **136**(17):6155–6158, 2014. 80, 81

[184] F. Tang, T. Ohto, S. Sun, et al. **Molecular Structure and Modeling of Water–Air and Ice–Air Interfaces Monitored by Sum-Frequency Generation.** *Chemical Reviews*, **120**(8):3633–3667, 2020. 82

[185] K. Meister, J. G. Duman, Y. Xu, et al. **The Role of Sulfates on Antifreeze Protein Activity.** *The Journal of Physical Chemistry B*, **118**(28):7920–7924, 2014. 85

[186] M. Fitzner, G. C. Sosso, S. J. Cox, and A. Michaelides. **Ice is born in low-mobility regions of supercooled liquid water.** *Proceedings of the National Academy of Sciences*, **116**(6):2009–2014, 2019. 85

[187] T. F. Whale, M. A. Holden, T. Wilson, et al. **The enhancement and suppression of immersion mode heterogeneous ice-nucleation by solutes.** *Chemical Science*, **9**(17):4142–4151, 2018. 86

REFERENCES

[188] D. R. LIDE. *CRC handbook of chemistry and physics*, **85**. CRC Pres, 2004. 87, 88

[189] O. BONNER. **The osmotic and activity coefficients of some guanidinium salts at 298.15 K**. *The Journal of Chemical Thermodynamics*, **8**(12):1167–1172, 1976. 88

[190] G. KLOPMAN. **Chemical reactivity and the concept of charge- and frontier-controlled reactions**. *Journal of the American Chemical Society*, **90**(2):223–234, January 1968. 88

[191] H. E. TOMALTY, L. A. GRAHAM, R. EVES, ET AL. **Laboratory-Scale Isolation of Insect Antifreeze Protein for Cryobiology**. *Biomolecules*, **9**(5):180, 2019. 88, 99, 107, 121

[192] W. L. JORGENSEN, D. S. MAXWELL, AND J. TIRADO-RIVES. **Development and Testing of the OPLS All-Atom Force Field on Conformational Energetics and Properties of Organic Liquids**. *Journal of the American Chemical Society*, **118**, 1996. 89, 92

[193] A. LUZAR AND D. CHANDLER. **Hydrogen-bond kinetics in liquid water**. *Nature*, **379**(6560):55–57, 1996. 90

[194] A. STRIOLO. **The mechanism of water diffusion in narrow carbon nanotubes**. *Nano Letters*, **6**(4):633–639, 2006. 90

[195] D. VAN DER SPOEL, P. J. VAN MAAREN, P. LARSSON, AND N. TÎMNEANU. **Thermodynamics of hydrogen bonding in hydrophilic and hydrophobic media**. *Journal of Physical Chemistry B*, **110**(9):4393–4398, 2006. 90

[196] F. W. STARR, J. K. NIELSEN, AND H. E. STANLEY. **Hydrogen-bond dynamics for the extended simple point-charge model of water**. *Physical Review E*, **62**(1):579, 2000. 90

[197] V. BALOS, S. IMOTO, R. R. NETZ, ET AL. **Macroscopic conductivity of aqueous electrolyte solutions scales with ultrafast microscopic ion motions**. *Nature Communications*, **11**(1):1611, 2020. 90

[198] M. MATSUMOTO, S. SAITO, AND I. OHMINE. **Molecular dynamics simulation of the ice nucleation and growth process leading to water freezing**. *Nature*, **416**(6879):409–413, 2002. 90

[199] B. DOHERTY, X. ZHONG, S. GATHIAKA, ET AL. **Revisiting OPLS force field parameters for ionic liquid simulations**. *Journal of Chemical Theory and Computation*, **13**(12):6131–6145, 2017. 92

[200] G. TESEI, V. ASPELIN, AND M. LUND. **Specific Cation Effects on SCN−in Bulk Solution and at the Air−Water Interface**. *The Journal of Physical Chemistry B*, **122**(19):5094–5105, 2018. 92

[201] W. WANG AND R. WOLF. **J.; Caldwell, JW; Kollman, PA; Case**. *DA Journal of Computational Chemistry*, **25**:1157–1174, 2004. 92

[202] A. HUDAIT, D. R. MOBERG, Y. QIU, ET AL. **Preordering of water is not needed for ice recognition by hyperactive antifreeze proteins**. *Proceedings of the National Academy of Sciences of the United States of America*, **115**(33):8266–8271, 2018. 99, 132

[203] C. ADAR, V. SIROTINSKAYA, M. BAR DOLEV, ET AL. **Falling water ice affinity purification of ice-binding proteins**. *Scientific Reports*, **8**(1):11046, 2018. 99, 107, 121

[204] C. J. MARSHALL, K. BASU, AND P. L. DAVIES. **Ice-shell purification of ice-binding proteins**. *Cryobiology*, **72**(3):258–63, 2016. 99, 107

[205] L. M. KOZLOFF, M. A. TURNER, AND F. ARELLANO. **Formation of bacterial membrane ice-nucleating lipoglycoprotein complexes**. *Journal of Bacteriology*, **173**(20):6528–36, 1991. 100

[206] R. SCHWIDETZKY, A. T. KUNERT, M. BONN, ET AL. **Inhibition of Bacterial Ice Nucleators Is Not an Intrinsic Property of Antifreeze Proteins**. *Journal of Physical Chemistry B*, **124**(24):4889–4895, 2020. 100

[207] B. G. PUMMER, C. BUDKE, S. AUGUSTIN-BAUDITZ, ET AL. **Ice nucleation by water-soluble macromolecules**. *Atmospheric Chemistry and Physics*, **15**(8):4077–4091, 2015. 100, 106

[208] M. L. LING, H. WEX, S. GRAWE, ET AL. **Effects of Ice Nucleation Protein Repeat Number and Oligomerization Level on Ice Nucleation Activity**. *Journal of Geophysical Research-Atmospheres*, **123**(3):1802–1810, 2018. 100, 131

[209] C. BONECHI, G. TAMASI, A. PARDINI, ET AL. **Ordering effect of protein surfaces on water dynamics: NMR relaxation study**. *Biophysical Chemistry*, **249**:106149, 2019. 100

[210] M. J. BURKE AND S. E. LINDOW. **Surface-Properties and Size of the Ice Nucleation Site in Ice Nucleation Active Bacteria - Theoretical Considerations**. *Cryobiology*, **27**(1):80–84, 1990. 100

[211] D. R. MOBERG, S. C. STRAIGHT, AND F. PAESANI. **Temperature Dependence of the Air/Water Interface Revealed by Polarization Sensitive Sum-Frequency Generation Spectroscopy**. *The Journal of Physical Chemistry B*, **122**(15):4356–4365, 2018. 101

[212] S. J. ROETERS, C. N. VAN DIJK, A. TORRES-KNOOP, ET AL. **Determining in situ protein conformation and orientation from the amide-I sum-frequency generation spectrum: theory and experiment**. *Journal of Physical Chemistry A*, **117**(29):6311–22, 2013. 103

[213] L. FU, Z. WANG, B. T. PSCIUK, ET AL. **Characterization of Parallel beta-Sheets at Interfaces by Chiral Sum Frequency Generation Spectroscopy**. *The Journal Physical Chemistry Letters*, **6**(8):1310–5, 2015. 103

[214] X. CHEN, J. WANG, J. J. SNIADECKI, ET AL. **Probing alpha-helical and beta-sheet structures of peptides at solid/liquid interfaces with SFG**. *Langmuir*, **21**(7):2662–4, 2005. 103

[215] A. BLUME, W. HUBNER, AND G. MESSNER. **Fourier transform infrared spectroscopy of 13C = O-labeled phospholipids hydrogen bonding to carbonyl groups**. *Biochemistry*, **27**(21):8239–49, 1988. 103

[216] H. H. MANTSCH AND R. N. MCELHANEY. **Phospholipid Phase-Transitions in Model and Biological-Membranes as Studied by Infrared-Spectroscopy**. *Chemistry and Physics of Lipids*, **57**(2-3):213–226, 1991. 103

[217] K. Basu, L. A. Graham, R. L. Campbell, and P. L. Davies. **Flies expand the repertoire of protein structures that bind ice**. *Proceedings of the National Academy of Sciences of the United States of America*, **112**(3):737–42, 2015. 104, 105

[218] N. Li, B. S. Kendrick, M. C. Manning, et al. **Secondary structure of antifreeze proteins from overwintering larvae of the beetle Dendroides canadensis**. *Archives of Biochemistry and Biophysics*, **360**(1):25–32, 1998. 104

[219] C. P. Garnham, J. A. Gilbert, C. P. Hartman, et al. **A Ca2+-dependent bacterial antifreeze protein domain has a novel beta-helical ice-binding fold**. *Biochemical Journal*, **411**(1):171–80, 2008. 105

[220] Y. Hasegawa, Y. Ishihara, and T. Tokuyama. **Characteristics of ice-nucleation activity in Fusarium avenaceum IFO 7158**. *Bioscience, Biotechnology, and Biochemistry*, **58**(12):2273–2274, 1994. 118

[221] P. L. Davies. **Ice-binding proteins: a remarkable diversity of structures for stopping and starting ice growth**. *Trends in Biochemical Sciences*, **39**(11):548–555, 2014. 118

[222] G. J. Warren. **Bacterial Ice Nucleation: Molecular Biology and Applications**. *Biotechnology and Genetic Engineering Reviews*, **5**(1):107–136, 1987. 119

[223] A. Margaritis and A. S. Bassi. **Principles and Biotechnological Applications of Bacterial Ice Nucleation**. *Critical Reviews in Biotechnology*, **11**(3):277–295, 1991. 119

[224] T. Zwieg, V. Cucarella, and M. Kauffeld. **Novel biomimetically based ice-nucleating coatings**. *International Journal of Materials Research*, **98**(7):597–602, 2007. 119

[225] D. Murakami and K. Yasuoka. **Molecular dynamics simulation of quasi-two-dimensional water clusters on ice nucleation protein**. *The Journal of Chemical Physics*, **137**(5):054303, 2012. 119

[226] Z. Yang, Y. Zhou, K. Liu, et al. **Computational study on the function of water within a beta-helix antifreeze protein dimer and in the process of ice-protein binding**. *Biophysical journal*, **85**(14507722):2599–2605, October 2003. 119, 120

[227] R. L. Green and G. J. Warren. **Physical and functional repetition in a bacterial ice nucleation gene**. *Nature*, **317**(6038):645–648, 1985. 119

[228] R. L. Green, L. V. Corotto, and G. J. Warren. **Deletion mutagenesis of the ice nucleation gene from Pseudomonas syringae S203**. *Molecular and General Genetics MGG*, **215**(1):165–172, 1988. 119

[229] S. J. Roeters, T. W. Golbek, M. Bregnhøj, et al. **The Ice Nucleating Protein InaZ is Activated by Low Temperature**. *bioRxiv*, 2020. 121, 126

[230] S. Pouleur, C. Richard, J.-G. Martin, and H. Antoun. **Ice Nucleation Activity in *Fusarium acuminatum* and *Fusarium avenaceum***. *Applied and Environmental Microbiology*, **58**(9):2960–2964, 1992. 132

[231] A. T. Kunert, M. L. Pöhlker, K. Tang, et al. **Macromolecular fungal ice nuclei in *Fusarium*: effects of physical and chemical processing**. *Biogeosciences*, **16**(23):4647–4659, 2019. 132, 134

[232] M. Cascajo-Castresana, R. O. David, M. A. Iriarte-Alonso, et al. **Protein aggregates nucleate ice: the example of apoferritin**. *Atmospheric Chemistry and Physics*, **20**(6):3291–3315, 2020. 133

Software

- The SFG and CD spectra shown in the Chapters 4, 5, 6, 7 and 8 were processed in IgorPro 6. The SFG spectra shown in 3 were processed in MATLAB R2020a.

- TINA droplet freezing assay data were processed in IgorPro 6 and plotted in OriginPro2019b.

- The Figures 1.4, 1.5, 2.2, 2.3 B, 2.8, 2.10 A, 7.1, and 7.4, as well as the TOC figure of Chapter 7 and the back cover figure of the printed version were created with *BioRender.com.*

Acknowledgements

This section is not included in this version.